CHAPTER 10
CORE TRANSPORT STUDIES IN JET

P. MANTICA,*[a] G. CORRIGAN,[b] X. GARBET,[c] F. IMBEAUX,[c] J. LONNROTH,[d] V. PARAIL,[b]
T. TALA,[e] A. TARONI,[f] M. VALISA,[g] and H. WEISEN[h]

[a]*Istituto di Fisica del Plasma, Euratom/ENEA-CNR Association, Via Cozzi 53, 20125 Milano, Italy*
[b]*Culham Science Centre, EURATOM/UKAEA Fusion Association, Abingdon OX14 3DB, United Kingdom*
[c]*Association EURATOM-CEA, CEA Cadarache, 13108 St Paul-Lez-Durance, France*
[d]*Association EURATOM-Tekes, Helsinki University of Technology, P.O. Box 2200, 02015 HUT, Finland*
[e]*Association EURATOM-TEKES, VTT, P.O. Box 1000, FIN-02044 VTT, Finland*
[f]*Former Member of the JET Joint Undertaking*
[g]*Consorzio RFX-Associazione Euratom-Enea sulla Fusione, I-35127 Padova, Italy*
[h]*EPFL, CRPP, Association EURATOM—Confederation Suisse, 1015 Lausanne, Switzerland*

This paper presents an overview of the state of the art of core transport studies in JET. It covers in various sections the topics of heat transport, particle and impurity transport, momentum transport, internal transport barrier physics and integrated core and edge modeling. For each topic, a brief summary of older results obtained under the JET Joint Undertaking and a review of recent results obtained under the European Fusion Development Agreement are presented and discussed in view of the possibility of extrapolating to ITER plasmas. A final outlook of future developments of core transport studies in JET concludes the paper.

KEYWORDS: *magnetic fusion, core tokamak transport, turbulence-driven transport*

Note: Some figures in this paper are in color only in the electronic version.

Contents—Chapter 10

*E-mail: mantica@ifp.cnr.it

I. INTRODUCTION

Core transport studies have always been an important topic of investigation in JET experimental work programs, as well as in many other tokamaks. The basic drive of such studies has been and still is to dig out sufficiently detailed experimental information to elucidate the basic transport mechanisms at work and validate existing theoretical transport models in order to achieve confidence in predictions of ITER temperature, density, impurity, and rotation profiles, rather than relying only on empirical global scaling laws. This goal, although not yet met, is certainly much nearer now due to increasing interaction between theory and experiment and more and more specific transport experiments performed in a coordinated way in a number of tokamaks, with an important contribution of JET related to the good quality of its diagnostics and to its size, which makes it the machine with parameters nearest those of ITER among the existing tokamaks.

Several areas of transport have been investigated in JET, namely, electron and ion heat transport, particle and impurity transport, and momentum transport. In each area, some basic questions regarding extrapolation to ITER have somehow constituted a focus for research. For example, will ITER temperature profiles be strongly limited by stiffness maintaining them close to marginality, and what will be the temperature critical gradient length? Consequently, will the pedestal height necessary to achieve the required core parameters be incompatible with limitations in wall loads? Will ITER density profiles be peaked? Will there be heavy impurity accumulation; will He ash accumulation be a problem? What level of toroidal rotation is to be expected in ITER? After years of work, a basic understanding of plasma core transport as driven by electrostatic turbulence, i.e., mainly by ion temperature gradient and trapped electron modes, has emerged and the answers to these questions start to be hinted at, although not yet consolidated.

This chapter reviews the progress achieved in JET in understanding core transport in the various channels, focusing on conventional L- and H-mode scenarios: Sec. II deals with heat transport (written by P. Mantica), Sec. III with particle and impurity transport (written by H. Weisen and M. Valisa), and Sec. IV with momentum transport (written by T. Tala). Then, the progress made in understanding the formation and sustainment of internal transport barriers (ITBs), which makes full use of the understanding achieved in the three above areas, is reviewed in Sec. V (written by T. Tala and X. Garbet), to provide a basis for possible advanced tokamak operation in ITER. Finally, the need for a comprehensive modeling of tokamak plasmas that accounts in a consistent way for the link between core and edge behavior is discussed in Sec. VI, and recent work done at JET in this area is reviewed (written by V. Parail, A. Taroni, G. Corrigan, F. Imbeaux, J. Lonnroth, and T. Tala.). In Sec. VII a final outlook on future developments of core transport studies in JET concludes the chapter.

II. CORE HEAT TRANSPORT STUDIES IN JET

II.A. Introduction

Since early operation, core heat transport studies have been present in the experimental work programs of JET, either as parasitic studies gathering information from the database of JET discharges or through dedicated experiments, such as systematic scans of plasma parameters or power deposition profiles and, more recently, power modulation experiments.

The basic issues that have been tackled by such work can be summarized as follows:

1. to investigate experimentally the parametric dependences of the core heat diffusivity on the main dimensional or dimensionless parameters

2. to propose and test heat transport models, either empirical or from basic theory, capable of explaining all available experimental observations

3. to investigate how temperature profiles react to changes in power deposition profiles, i.e., whether transport is local and diffusive

4. to check consistency of findings on local core heat transport with global confinement scaling laws.

The purpose of this section is to present an overview of how the answers to these questions have been evolving at JET with time, following the refinement of experimental techniques and diagnostic capabilities and the evolution of the theoretical views on heat transport.

Major steps forward on the diagnostic side have been the availability of ion temperature profile measurements and fast time resolution electron temperature profile measurements. On the theory side, the notion of the existence of a threshold in the inverse temperature gradient length for the onset of electrostatic turbulence has finally allowed us to understand within a single frame several existing observations and has driven ideas for further experimental work. Last, but not least, a significant change in the experimental methods to investigate core heat transport has taken place. In the past, most dedicated heat transport experiments in JET were done in steady-state conditions. Few attempts were made to gain some additional insight using the available perturbative techniques at the time, i.e., sawteeth-generated heat pulses and cold pulses from laser ablation of metallic impurities in the edge. Substantial progress in the understanding of core heat transport was somehow hindered by the absence on JET of a localized direct electron heating source such as electron cyclotron heating, which was instead available on other major devices such as ASDEX Upgrade, DIII-D, JT-60U. Power modulation using neutral beam injection (NBI) or ion cyclotron resonance heating (ICRH) in minority heating turned out to be unsatisfactory for transport studies due to very broad power deposition profiles and the mediation of fast ions with long slowing-down times. Starting in 2001, however, a new scheme for ICRH absorption was optimized in JET D plasmas with a ^{3}He component, based on mode conversion of the launched waves into ion Bernstein waves at the ion-ion hybrid layer, which generates short-wavelength electrostatic waves damped directly on electrons in a localized region (see Chapter 9 of this issue). This scheme has proved able to achieve power modulation results of quality similar to that of ECH modulation, although much more cumbersome to use. It was then possible to verify on JET some of the latest findings concerning electron heat transport obtained in ASDEX Upgrade and to carry out a comparative study between the two devices, which has added valuable information for electron heat transport understanding. A recent upgrade of the ion temperature diagnostics will soon enable us also to tackle with similar methods the ion channel, using modulation of ICRH with a ^{3}He minority scheme, which has rather a narrow ion deposition profile and short fast ion slowing-down time. Therefore, a major component of recent heat transport–dedicated experiments on JET has been (and will remain for the next years) focused on perturbative techniques to get the most complete physics picture of heat transport in both electron and ion channels. This provides a challenging set of experimental results for the validation of various first-principle theory models in view of extrapolation to transport prediction in future machines.

II.B. Core Heat Transport Studies in the JET Joint Undertaking Phase

Earliest heat transport analyses at JET as reported in Refs. 1 and 2 used a one-fluid approximation due to lack of ion profile measurements to ensure separation of ion and electron channels. Starting from the general representation for the total heat flux $\mathbf{q}$

$$\mathbf{q} = -n\chi\boldsymbol{\nabla}T + \mathbf{q_{flow}} \ , \qquad (1)$$

where n is the density, T is the temperature, and χ is the heat diffusivity, they aimed at distinguishing on the basis of JET data between a "heat pinch or excess temperature gradient model" (in which $\mathbf{q_{flow}}$ could be interpreted either as a thermal flow or as a critical gradient term $\mathbf{q_{flow}} = +n\chi\boldsymbol{\nabla}T_c$) and a nonlinear χ model in which $\mathbf{q_{flow}} = 0$ and $\chi \sim \boldsymbol{\nabla}T^\beta$. It was pointed out that both models would be consistent with the finding from sawtooth heat pulse propagation that the perturbative χ (χ^{HP}) is larger than power balance χ (χ^{PB}). It was also remarked that although neither model implies rigorously a stiffness of temperature profiles, still, due to the fact that temperature is a double integral of the heating profile, temperature reacts weakly to changes in power deposition. The two models were found to describe equivalently well the local heat transport data. However, by deriving global scaling laws from the models, it was found that the heat pinch model yielding an offset linear law for the total stored energy W versus input power P_{in} described better the overall JET data set. In Ref. 2 the dependence of heat flux on local parameters was investigated and a clear dependence on plasma current was identified:

$$\mathbf{q} = -C/In\boldsymbol{\nabla}T + \mathbf{q_{flow}} \qquad (2)$$

in which C is a constant and I the plasma current enclosed by the magnetic surface.

A heuristic model based on the assumption that turbulence in the magnetic topology was the cause for anomalous transport was proposed in Ref. 3 in support of the concept of a critical gradient in the heat flux. Chains of islands would form around rational magnetic surfaces and chaos (inducing transport enhancement) would occur when islands overlapped radially. This would take place when a critical value of the electron temperature gradient

was exceeded. Therefore, the electron temperature gradient would determine both the electron and ion transport. Specific expressions for the threshold and for the electron and ion diffusivities were derived heuristically and tested rather successfully against data from various tokamaks and plasma regimes (Ref. 3 and references therein). An offset linear scaling for the total electron energy was also derived, whose numerical coefficients were obtained by fit to JET data.

Further detailed experiments to demonstrate the local character of transport made use of a systematic comparison of on-axis and off-axis ICRH heating.[4,5] As shown in Figs. 1 and 2 (Ref. 4), it was found that the electron temperature profile responds to the heating profile and there was no need to invoke nonlocal features to explain the profile evolution. By inducing a large core thermal sink with pellet injection, it was also possible to exclude the existence of a substantial thermal pinch (Fig. 2), further confirming that Eq. (1) should always be interpreted in terms of a critical gradient concept. In those studies, however, a nonlinear model for the heat flux was preferred, i.e., a quadratic or cubic dependence of the heat flux on $q^{1.75}n_e\nabla T_e$, where q is the safety factor.[4] The possibility of varying the temperature gradient by varying the heat flux led also to the conclusion that in JET, temperature profiles are not stiff. This conclusion will be discussed further in the next sections in light of present understanding.

Fig. 2. (a) Radial electron temperature profile from ECE measurements at different times for on-axis (solid line) and off-axis (dotted line) heating cases with pellet injection. (b) Total volume integrated heating power (ICRH + ohmic) for both cases (from Ref. 4). Discharge parameters are $B_T = 2.8$ T, $I_p = 3.3$ MA, and $\langle n_e \rangle \sim 4 \times 10^{19}$ m^{-3}.

The dependence of core heat transport on isotope mass was also investigated in JET H-mode plasmas with H, D, D-T, and T isotopes.[6] It was found that core heat transport increases with mass in approximate agreement with theoretical models of the gyro-Bohm type ($\chi/B \sim \rho^{*3}$, where ρ^* is the normalized ion Larmor radius).

In addition to steady-state studies, perturbative studies using sawteeth heat pulses indicated that the heat pulse propagation was consistent with diffusive transport but with a measured perturbative diffusivity χ^{HP} 2 to 10 times larger than the power balance one, χ^{PB} (Refs. 7 and 8). This evidence is in accordance both with a critical gradient idea giving an offset linear dependence of the heat flux on the gradient and with a nonlinear dependence of heat flux on the gradient, so it did not help to discriminate between the two models. Cold pulses from edge instead showed an immediate reaction of plasma core to edge perturbations,[9] which brought into discussion the idea of nonlocal transport,[10] apparently in contrast with the observations from the ICRH profile shaping experiments described above. The fast reaction of the core to edge variations was observed also in L-H transitions.[11,12]

In the latest phase of the JET Joint Undertaking, an empirically based model for core heat transport was proposed and validated against a wide range of JET discharges. This model features a heat diffusivity that is the sum of a Bohm and a gyro-Bohm term[13]:
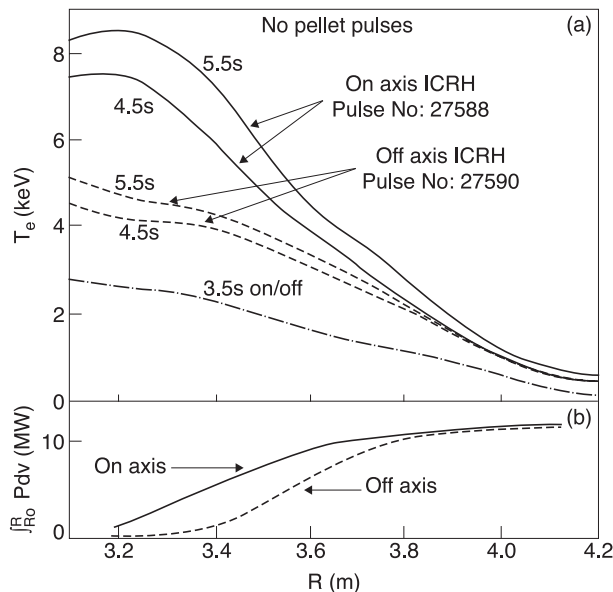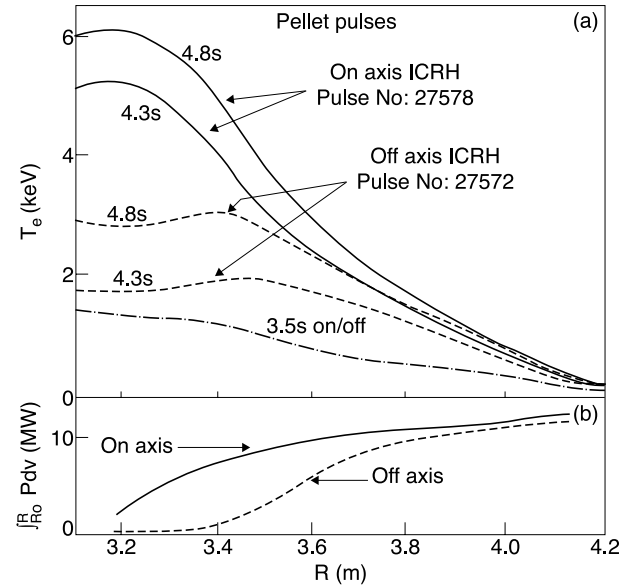

Fig. 1. (a) Radial electron temperature profile from ECE measurements at different times for on-axis (solid line) and off-axis (dotted line) heating cases with gas fueling. (b) Total volume integrated heating power (ICRH + ohmic) for both cases (from Ref. 4). Discharge parameters are $B_T = 2.8$ T, $I_p = 3.3$ MA, and $\langle n_e \rangle \sim 3 \times 10^{19}$ m^{-3}.

$$\chi_{e,i} = \chi_{Be,i} + \chi_{gBe,i} \ . \tag{3}$$

Here, χ_B is a Bohm diffusivity that becomes dominant in the outer part of the plasma:

$$\chi_{Be} = \alpha_B \frac{T_e}{eB_T} L_{pe}^{*-1} q^2 \ ,$$

$$L_{Pe}^* = \frac{p_e}{a|\nabla p_e|} \ ,$$

and

$$\chi_{Bi} = 2\chi_{Be} \ , \tag{4}$$

with B_T being the magnetic field, p_e the electron pressure, and a the minor radius.

χ_{gB} is the gyro-Bohm diffusivity, equal for ions and electrons, which contributes to transport mainly in the plasma core:

$$\chi_{gB} = \alpha_{gB} \frac{T_e}{eB_T} L_{Te}^{*-1} \rho^*$$

and

$$L_{Te}^* = \frac{T_e}{a|\nabla T_e|} \ . \tag{5}$$

To account for fast cold pulse propagation from the edge while still maintaining regular diffusive sawteeth propagation from the core, the model has been complemented by the addition of a nonlocal term into the Bohm part, which sets a dependence of χ on the value of the electron temperature gradient length in the edge region ($0.8 < \rho < 1$):

$$\chi_{e,i} = \chi_{Be,i}(T_{e(\rho=0.8)} - T_{e(\rho=1)})/T_{e(\rho=1)} + \chi_{gBe,i} \ . \tag{6}$$

In the case of H-mode, the edge temperature is taken at the top of the pedestal rather than at the separatrix.

This model was shown to be capable of satisfactorily reproducing temperature profiles from a large number of JET discharges in both L- and H-mode and also sawteeth heat pulses and fast edge cold pulses and L-H transitions with a unique choice for the values of the coefficients:

$$\alpha_{gB} = 3.5 \times 10^{-2} \quad \text{and} \quad \alpha_B = 8 \times 10^{-5} \ .$$

The q dependence in the Bohm term, which dominates volume integrals, guarantees the reproduction of the observed experimental scaling of global confinement with plasma current. It is important to note that this model does not feature a threshold in the value of the temperature gradient length, so it belongs to the class of the nonlinear rather than offset linear models for the heat flux.

The apparent impasse due to the impossibility of discriminating between a nonlinear or offset linear (threshold) model on the basis of steady-state data or even sawtooth heat pulses and edge cold pulses was overcome during recent years, mainly due to a progress in the theoretical understanding of transport and also to the availability on JET of a tool to perform electron temperature modulation studies. Sections II.C and II.D give brief descriptions of these two theoretical and experimental tools, respectively, which have allowed us to make a step forward in the understanding of JET core transport.

II.C. The Concept of Critical Temperature Gradient Length in the Electrostatic Turbulence Framework

Progress in theoretical understanding of plasma turbulence has led to the hypothesis that, at least in low-β plasmas, most of the heat transport in the core is carried by electrostatic microinstabilities, namely, the ion temperature gradient (ITG) mode, the trapped electron mode (TEM), and the electron temperature gradient (ETG) mode. This assumption should hold if the plasma $\beta = 2\mu_0 p/B^2$ (where p is the total pressure and B the magnetic field) is lower than the instability threshold of kinetic ballooning modes. Given that the level of transport carried by ETGs even in the presence of streamers (i.e., radially elongated structures) is much smaller than that driven by fully developed ITG/TEMs (Ref. 14), in Sec. II dealing with plasmas that are above ITG/TEM thresholds along most of the radius we avoid proper modeling of the ETG component of electron transport, regarding it rather as a residual transport level that plays a role only near the magnetic axis, where the TEMs are stabilized.

ITG/TEM modes are unstable in the limit of large wavelengths such that $k_\perp \rho_i < 1$, where $k_\perp$ is the perpendicular wave number and ρ_i is the ion Larmor radius [$\rho_i = (m_i T_i)^{1/2}/eB$, where m_i is the ion mass and T_i is the ion temperature]. In the nonlinear regime, they produce particle, momentum, and heat transport. An important feature of these micromodes is the existence of an instability threshold, given by a critical value of the inverse temperature gradient length $R/L_T = R|\nabla T|/T$ (where R is the major radius) of ions for ITG and of electrons for TEM. Such thresholds depend on the density gradient length and on other plasma parameters such as T_e/T_i and the magnetic shear s, as discussed in Ref. 15. Figure 3 (Ref. 15) shows an example of a stability diagram in the special case when the electron and ion temperatures are equal, $T_e = T_i$. Depending on the values of gradient lengths, zero, one, or two modes may be unstable. A separate treatment of ion and electron modes is usually an oversimplification. Nevertheless, there exist experimental situations in which one branch is dominant, for instance, when one species is hotter than the other, or depending on the density gradient (i.e., ITGs tend to dominate for flat density profiles and TEMs tend to dominate for peaked density profiles).
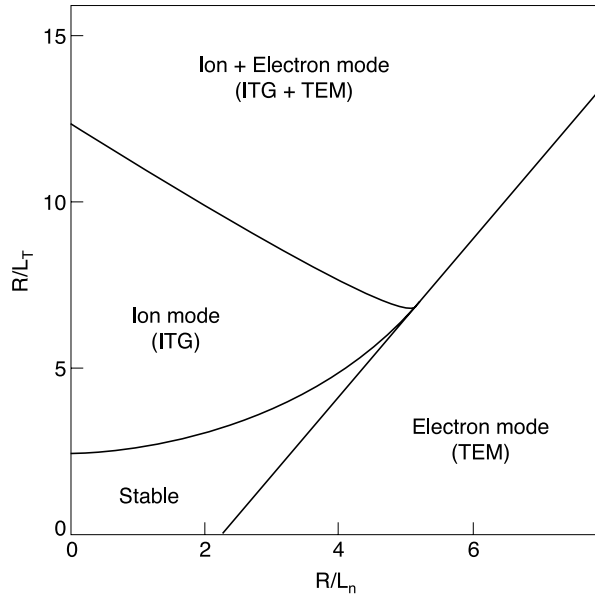
Fig. 3. Stability diagram of ITG/TEM modes. Electron and ion temperatures are equal (from Ref. 15).

Fig. 4. Schematic diagram of the dependence of the heat flux on the inverse temperature gradient length in a critical gradient–based model.

A wide range of theoretical models based on electrostatic turbulence is available, from one-dimensional (1-D) quasi-linear transport models to three-dimensional nonlinear fluid and kinetic turbulence codes. One of the aims of the ongoing work related to core heat transport understanding is to verify to what extent these models can explain the available experimental evidence (for example, see the review in Ref. 16). A brief account of work done at JET in this direction is presented in Sec. II.H.

In this section we rather describe a simple semiempirical transport model developed for electron heat transport,[17,18] based on the idea of a threshold in the inverse temperature gradient length and used very successfully for the analysis of electron heat transport experiments. The model does not pretend to take into account the complete transport physics, but it is a useful tool to investigate the validity of the threshold hypothesis and to compare results from different plasmas and machines.

In this critical gradient model (CGM), the electron heat diffusivity is written as

$$
\chi_e = \chi_s q^{3/2} \frac{T_e}{eB} \frac{\rho_s}{R} \left[\frac{R}{L_{T_e}} - \frac{R}{L_{T_{e,crit}}} \right] H \left[\frac{R}{L_{T_e}} - \frac{R}{L_{T_{e,crit}}} \right]
$$
$$
+ \chi_0 \frac{T_e}{eB} \frac{\rho_s}{R} \ , \tag{7}
$$

where $\rho_s = (m_i T_e)^{1/2}/eB$. This model is graphically illustrated in Fig. 4. We note that Eq. (7) implies a linear dependence of χ on R/L_T, and therefore a quadratic dependence of heat flux, whereas recent theoretical predictions (e.g., Ref. 19 for ITG turbulence and Ref. 20 for

TEM turbulence) have found a linear dependence of the heat flux on R/L_T. Because in the experimental range of heat fluxes that characterizes the JET experiments presented in this paper the two dependences are indistinguishable, we have decided to continue to adopt Eq. (7) in spite of its being in disagreement with the theoretical linear dependence of the heat flux, in order to be consistent with previous experimental work and thus be able to compare results.

χ_e features an increase from a basic level, not necessarily neoclassical, to a higher turbulent level, when a critical value $R/L_{T_{e,crit}}$ is exceeded. H is the Heaviside step function, which provides the threshold effect above $R/L_{T_{e,crit}}$. The residual transport term is quantified by the dimensionless parameter χ_0, and χ_s quantifies the turbulent term, which, being proportional to the slope of the heat flux curve above threshold, yields the level of stiffness of temperature profiles. For large χ_s values, an increase of the heat flux drives a large increase in χ_e and therefore does not result in a change of R/L_{T_e}, thereby leading to stiff temperature profiles. The coefficients χ_s and χ_0 and the threshold are adjusted to fit the data best. They are assumed to be uniform in space, which is a simplification due to the need to avoid too many free parameters in fitting the available data. However, the TEM threshold is expected to strongly increase in the very center but not to be strongly varying with radius outside the very core, so the assumption is not physically unjustified. A similar model can be worked out for ions, whose stiffness level is expected to be larger than that of electrons, although experimental estimates are not yet available. We would like to stress that the underlying

hypothesis behind Eq. (7) is that electron heat transport is mainly driven by TEMs, with other contributions such as neoclassical and ETG- and ITG-driven electron transport being grouped into the residual term. Therefore, the model is expected to work well in situations of dominant electron heating and $T_e \gg T_i$, while it may turn out to be too simplistic in situations with mixed ion and electron heating and $T_e \sim T_i$, where strong coupling in the instabilities between electron and ion dynamics occurs. Such situations are, of course, most often occurring in JET plasmas. Nevertheless, the use of the model in Eq. (7) turns out to be useful also in JET, as will be discussed in the next sections, to provide in situations of dominant electron heating a quantitative comparison of stiffness levels and thresholds with those from other machines and to identify in situations of mixed heating more complex trends with increasing ion heating that point to the need to use more complete first-principle-based theoretical models.

The normalization factor $(T_e \rho_s)/(eBR)$ in both terms reflects the gyro-Bohm character of transport (supported both by theory and by scaling studies[21]) and introduces a temperature dependence $T_e^{3/2}$ in χ_e. We remark that the normalized coefficient χ_s describes the intrinsic stiffness of the plasma, whereas the effective stiffness is given by all factors multiplying the difference between R/L_{T_e} and threshold in Eq. (7) and therefore scales with temperature. The dependence on q, the safety factor, is introduced to recover the experimentally observed dependence of confinement on plasma current and radial increase of transport from core to edge. Theoretically, it is supported by nonlinear gyrokinetic simulations of TEM as due to an increase in size of turbulent eddies with increasing q (Ref. 22). Originally, an identical q dependence was proposed for both terms in Ref. 18, but in later work the q dependence was dropped from the residual term since it did not reproduce the data correctly. This is still consistent with a scaling with plasma current since confinement is determined by the turbulent part. Apart from explicit dependences on ρ_s and safety factor and from the inherent scaling with power of Eq. (7), other parameters that are seen to affect core confinement (such as collisionality or elongation) would be hidden in the parametric dependences of threshold and χ_e, whereas parameters such as triangularity or fueling that are seen to affect global confinement through their impact on pedestal would, of course, not be involved in Eq. (7). For a complete review on confinement scaling studies on JET, we refer to Chapter 3 of this issue.[21]

II.D. The Use of Temperature Modulation Experiments in Recent JET Heat Transport Work

It has been widely demonstrated that the use of temperature perturbations in addition to steady-state data allows a more powerful investigation of heat transport mechanisms. For a recent review on perturbative trans-

port we refer to Ref. 23. Because of the lack, until recently, of an ion temperature diagnostic with sufficient time resolution, perturbative heat studies at JET have focused on the electron channel. Therefore, Sec. II.E refers to the electron channel only. The work on ion transport based just on steady-state data is briefly reviewed in Sec. II.J.

For the purpose of this section we briefly review that heat waves travel in the plasma according to a perturbed heat diffusivity χ_e^{HP}, which is given by the slope of the heat flux versus temperature gradient curve and therefore differs from that of the power balance (χ_e^{PB}) when the heat flux is a nonlinear or offset linear function of the gradient:

$$\chi_e^{HP} = -\frac{\partial q_e}{n_e \partial \nabla T_e} = \chi_e + \frac{\partial \chi_e}{\partial \nabla T_e} \nabla T_e \neq \chi_e^{PB}$$

$$= -\frac{q_e}{n_e \nabla T_e} \quad . \tag{8}$$

In modulation experiments, the temperature time traces can be Fourier analyzed to derive spatial profiles of the amplitude (A) and phase (φ) of the perturbation at various harmonics of the modulation frequency. χ_e^{HP} is related in a simple way to the spatial derivatives of the phase (i.e., to the propagation speed) and of the amplitude (i.e., to the heat wave damping) and can be worked out from the experimental data either with simplified formulas or with full transport simulations.[23]

In the critical gradient model of Eq. (7), χ_e^{HP} is given by

$$\chi_e^{HP} = \chi_s q^{3/2} \frac{T_e}{eB} \frac{\rho_s}{R} \left[2\frac{R}{L_{T_e}} - \frac{R}{L_{T_e,crit}} \right]$$

$$\times H \left[\frac{R}{L_{T_e}} - \frac{R}{L_{T_e,crit}} \right] + \chi_0 \frac{T_e}{eB} \frac{\rho_s}{R} \quad . \tag{9}$$

It can be seen that when crossing the threshold, χ_e^{HP} exhibits a strong discontinuity, as shown in Fig. 5, which is the reason that perturbations are more suitable than a steady state to detect the existence of a critical gradient mechanism.

The experimental setup to perform T_e modulation experiments in JET is based on the use of ICRH modulation in mode conversion scheme. This takes place in D plasmas with a ^{3}He concentration $\sim$20%, so the launched waves convert into ion Bernstein waves at the ion-ion hybrid layer, which generates short-wavelength electrostatic waves damped directly on electrons in a localized region. The frequency used was 33 to 37 MHz. For more details we refer to Refs. 24 and 25. The toroidal field B_T in such a configuration needs to be in the range 3.2 T $<$ $B_T <$ 3.6 T. The location of deposition depends both on B_T and on the ^{3}He concentration, which is kept under
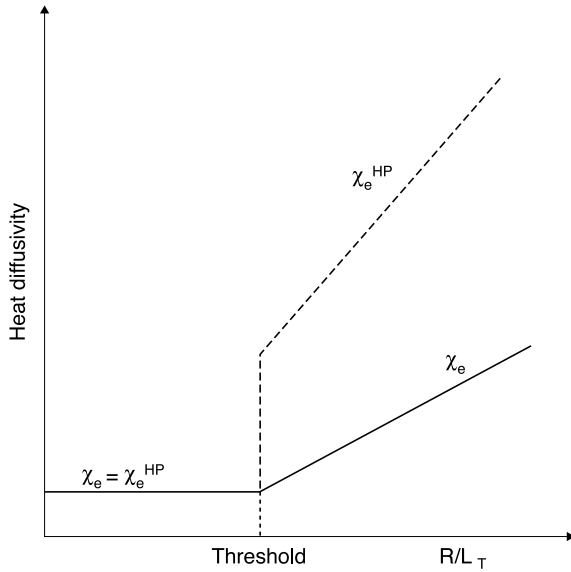
Fig. 5. Schematic diagram of the behavior of heat diffusivity with inverse temperature gradient length in a critical gradient–based model.

real-time control to avoid shifts in the deposition during a discharge. The T_e dynamic response to power modulation is measured with the 96-channel electron cyclotron emission (ECE) heterodyne radiometer. The ICRH power is modulated at a frequency of 15 to 20 Hz with a duty cycle $\sim$0.6 and an amplitude $\Delta P = 50\%$. Because of the absence of a reliable theoretical prediction of the mode conversion power deposition profile, the latter is extracted together with the heat diffusivity from a best fit of amplitude and phase profiles at three harmonics using the transport code ASTRA (Ref. 26) and the χ_e model in Eq. (7). Various results have been presented in Refs. 23 and 27 through 30 and are summarized in the next section.

II.E. Results on JET Core Electron Heat Transport from T_e Modulation Experiments

A typical example in a JET L-mode plasma of experimental profiles of steady-state T_e and amplitudes and phases at first and third harmonics of the modulation is shown (dots) in Fig. 6 (Ref. 28). Also shown are the power deposition and χ_e profiles derived by best fit of both steady-state T_e and modulation data performing simulations by means of the ASTRA code (the lines in Fig. 6 indicate the best-fit simulation). In this discharge ICRH was applied off-axis at $\rho_{dep} \sim 0.3$ and an asymmetry of propagation inside and outside ρ_{dep} can be observed. The slopes of A and φ in the inner part of the plasma are much steeper than in the outer part, indicating a rather abrupt change of χ_e^{HP}, which is consistent with the T_e inverse gradient length passing from below threshold inside ρ_{dep} (slow propagation, high damping) to above threshold outside ρ_{dep} (fast pro-

gation, small damping). Best fit of the data yields an estimate of the threshold $R/L_{T_{crit}} \sim 5$, which is consistent with estimates of the TEM threshold obtained for this shot from the linear gyrokinetic code KINEZERO (Refs. 31 and 32). The stiffness level is rather high, $\chi_s \sim 0.9$, which implies that the T_e profile is bound to threshold in the whole region outside $\rho = 0.3$. We also remark that the level of residual transport below TEM threshold expressed by $\chi_0 \sim$ 0.7 is significantly above the electron neoclassical level and could correspond to electron transport driven by ITG or ETG turbulence.

To verify the presence of a critical gradient–regulated transport, several discharges with T_e modulation have been performed while varying the profile of electron heat flux by changing ICRH location and NBI power level. The resulting variations in electron power density, heat flux, and T_e profiles are illustrated in Figs. 7a and 7b (Ref. 27). Figure 8 (Ref. 27) illustrates the changes in T_e profiles in log scale (for completeness ions also are shown) and the changes in R/L_{T_e}. One can see that the T_e (and T_i) profiles can change shape as far as R/L_T stays below a critical value, above which it is not possible to increase R/L_T any further. Therefore, the variation of core temperature profiles, which at first sight can be taken as evidence for lack of stiffness, is in reality merely due to the fact that profiles can well be modified when they are below threshold due to lack of central power, but cannot be brought significantly above the threshold level of R/L_T, consistent with a stiff model such as in Eq. (7). Therefore, the evidence of T_e profile change as in Fig. 7a is not a demonstration of lack of stiffness but is fully consistent with the picture of stiff transport above a critical gradient.

The threshold found from analysis of modulation data in these experiments is $R/L_{T_{e,crit}} \sim 5$, which is also plotted in Fig. 8b. One can see that depending on the shape and magnitude of power deposition, there are examples of discharges below or above threshold along the whole radius, or also crossing threshold around mid-radius (like the one in Fig. 6). We note that the data in Figs. 7 and 8 are fully consistent with the critical gradient hypothesis. For example, around $\rho = 0.35$, shot 55809 goes from above to below threshold, due to lack of central heat flux linked with off-axis deposition, while 55802 remains well above threshold due to central deposition. Outside $\rho = 0.35$ the T_e gradient has similar values for the two shots, whereas inside they depart, with 55809 decreasing below threshold and 55802 remaining above it. This behavior is clearly seen in Figs. 7 and 8, although the uncertainties in the T_e gradient are significant, and fully supports the CGM model. However, the crucial confirmation of the validity of the CGM picture comes from the behavior of the heat waves, which are observed to behave fully consistently with the steady-state information about the plasma being above or below threshold at a given location. In other words, for the same shots as in Fig. 8, amplitude and phase profiles shown in Fig. 9 (Ref. 27) indicate fast propagation and small attenuation
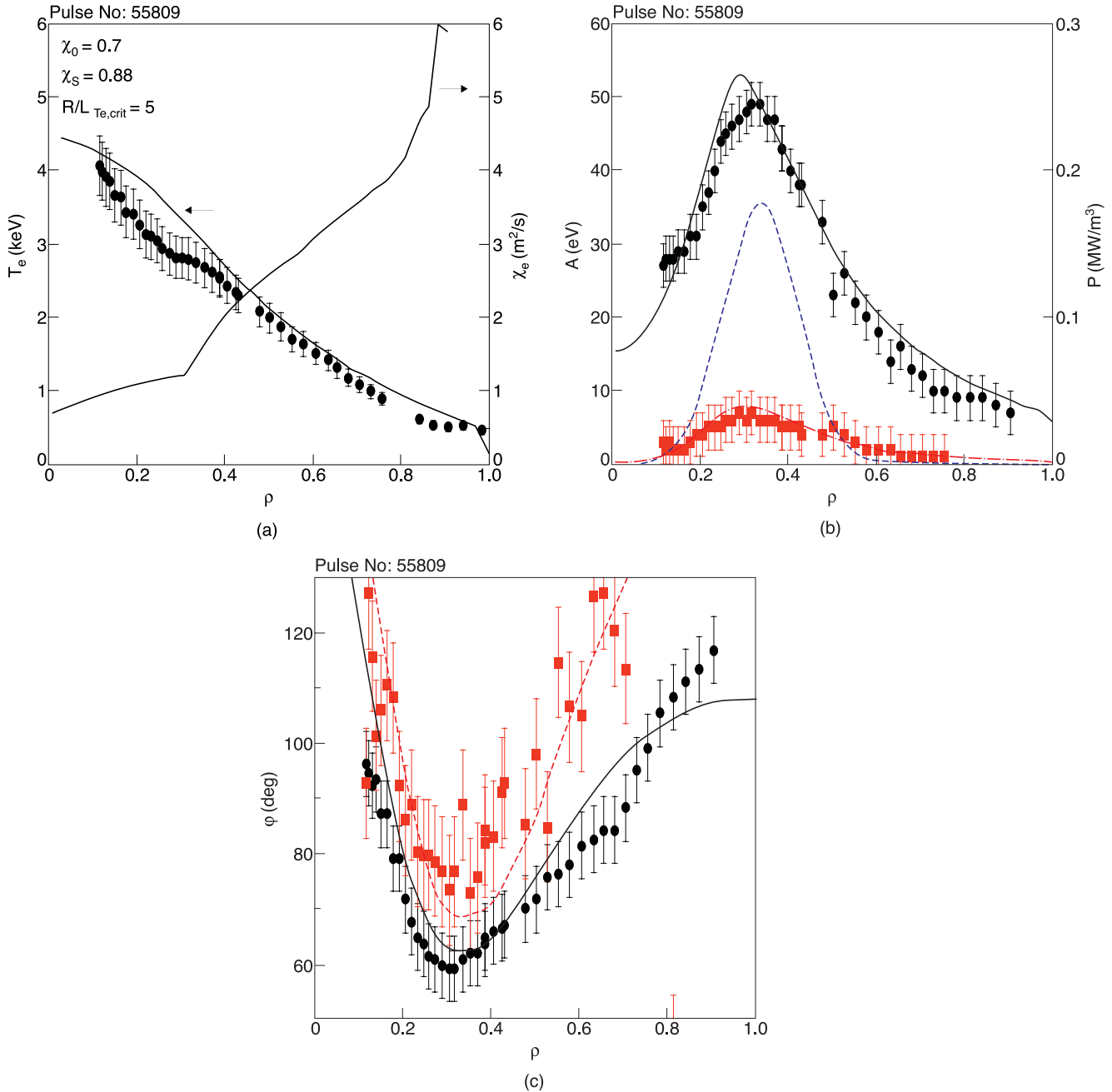
Fig. 6. Experimental (dots) and simulated (lines) profiles of (a) T_e (together with χ_e profile), (b) A at first (black circles) and third (red squares) harmonics (together with rf P_e profile, dashed line), and (c) φ at first (black circles) and third (red squares) harmonics for L-mode discharge 55809 ($B_T = 3.25$ T, $I_p = 1.6$ MA, and $n_{e0} = 2.7 \times 10^{19}$ m^{-3}). The simulation uses the model in Eq. (7) with parameters $R/L_{T_{e,crit}} = 5$, $\chi_s = 0.88$, and $\chi_0 = 0.7$. Note that the effect of an MHD island at $0.25 < \rho < 0.3$ (which locally flattens the T_e profile and is also visible on the A and φ profiles) is outside the scope of the simulation. Figure adapted from Ref. 28. (Color online)

(flat slopes of A and φ) in regions above threshold and slow propagation and strong damping (sharp slopes of A and φ) in regions below threshold.

Having assessed in L-mode plasmas the existence of a threshold above which the onset of rather stiff transport is observed, a comparison was made with H-mode plasmas with similar parameters apart from injected power ($P_{NBI} > 10$ MW is necessary to get into type III H-mode in these high-B_T discharges). This is illustrated in Fig. 10 and described in Ref. 28. R/L_{T_e} is basically the same in
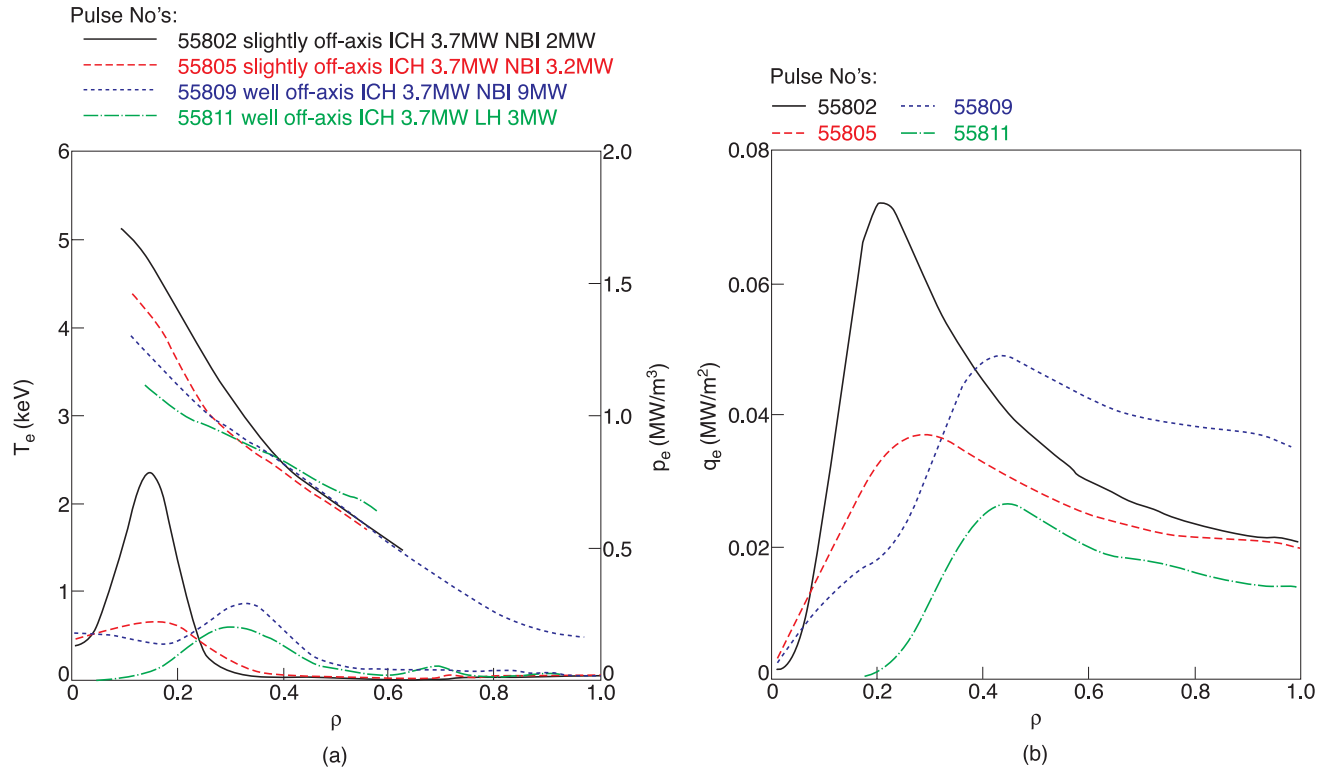
Fig. 7. (a) Power deposition and T_e profiles for four discharges from the heat flux scan experiments, all with similar main plasma parameters ($3.25\,\text{T} < B_T < 3.45\,\text{T}$, $1.6\,\text{MA} < I_p < 1.8\,\text{MA}$, and $2.7 \times 10^{19}\,\text{m}^{-3} < n_{e0} < 3 \times 10^{19}\,\text{m}^{-3}$), and (b) electron heat flux profiles for the same four discharges. From Ref. 27.

L-mode and H-mode and the T_e profiles in log scale are almost parallel, higher T_e in the core being achieved in H-mode mainly because of the higher pedestal. The heat waves behave similarly but with slightly higher slopes in the stiff region ($0.3 < \rho < 0.8$) in the H-mode case, in spite of its higher temperature. The intrinsic stiffness level χ_s is found to be ~ 0.9 in H-mode and ~ 1.3 in L-mode, and $R/L_{T_{e,crit}} \sim 5$ in H-mode and ~ 4 in L-mode.

Figure 11 (Ref. 28) shows the correlation between edge and core T_e values found in a set of similar shots ($3.25\,\text{T} < B_T < 3.45\,\text{T}$, $1.6\,\text{MA} < I_p < 1.8\,\text{MA}$, and $2.8 \times 10^{19}\,\text{m}^{-3} < n_{e0} < 3.5 \times 10^{19}\,\text{m}^{-3}$) with different NBI heating ($0 < P_{NBI} < 16.5\,\text{MW}$) and with increasing pedestal. Such correlation is another signature of a stiff behavior.[33] Ions exhibit a very similar behavior, as will be discussed in Sec. II.J. Note the perfectly linear correlation between T at pedestal and T at $\rho = 0.3$, indicating the presence of stiffness in this region, while the on-axis T_e bends down with respect to the line, indicating the maximum value attainable assuming a uniform threshold. This is due to the fact that the very core region goes below threshold, particularly in H-mode, which presents a wider core region below threshold due to higher boundary T_e, as explained in Ref. 18.

Finally, one can try to combine various similar JET L-mode and H-mode shots with modulation and with different heat flux profiles into a plot of heat flux versus gradient length of the type sketched in Fig. 4. The result is shown in Fig. 12 (Ref. 30), in which two radial positions, $\rho = 0.2$ and $\rho = 0.4$, have been used to get two steady-state values per shot in order to enrich the plot with points both above and below threshold, assuming threshold would not significantly vary in this rather small spatial range, consistent with the simplification we adopt for the modulation analysis of a uniform threshold profile. Given that all shots have modulation and have been fitted with the CGM model, we can also superimpose on the steady-state points the line coming from the CGM model with the typical parameters we have found. In Fig. 12 a normalization of the heat flux consistent with the parameterization adopted for χ_e in Eq. (7) has been used to account for different values of B_T, n_e, T_e, and q in order to build one curve for the whole set of data. This possibility is based on the fact that modulation analysis for each of them yields very similar values for the threshold. On the other hand, two different ranges of values for the stiffness factor have been found; namely, shots having only electron heating show lower χ_s (0.2 to 0.3) whereas shots with some amount of NBI ion heating show higher χ_s (~ 0.9 to 1.3). This result is discussed in detail in the next sections. These two groups have been plotted in Fig. 12 with different symbols since they

(a)

(b)
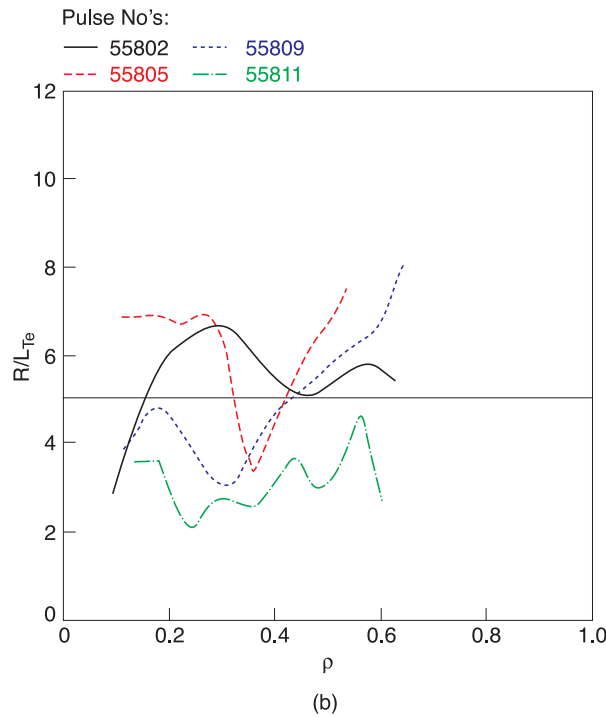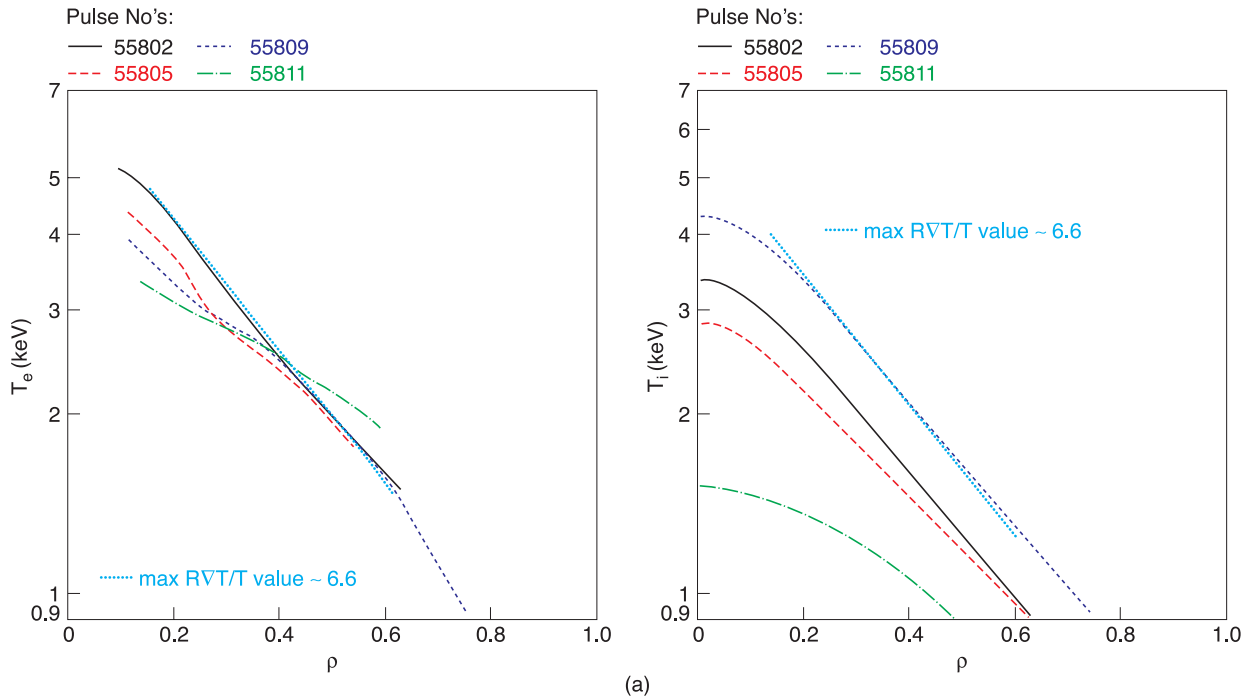
Fig. 8. (a) T_e and T_i profiles in log scale for the four discharges shown in Fig. 7 and (b) profiles of R/L_{T_e} for the same discharges. The threshold value found from modulation experiments is also plotted (straight black line). From Ref. 27.

belong to two different curves. One can see that the steady-state heat flux values are broadly consistent with the critical gradient picture; however, the uncertainties are such that they alone would not constitute a demonstration of the threshold existence, nor of the

increase in stiffness levels in the presence of ion heating. Unless finer ad hoc scans of heat flux values are made, as were performed in ASDEX Upgrade,[23,34–36] modulation experiments are the only possibility in JET to provide evidence for the existence of the threshold
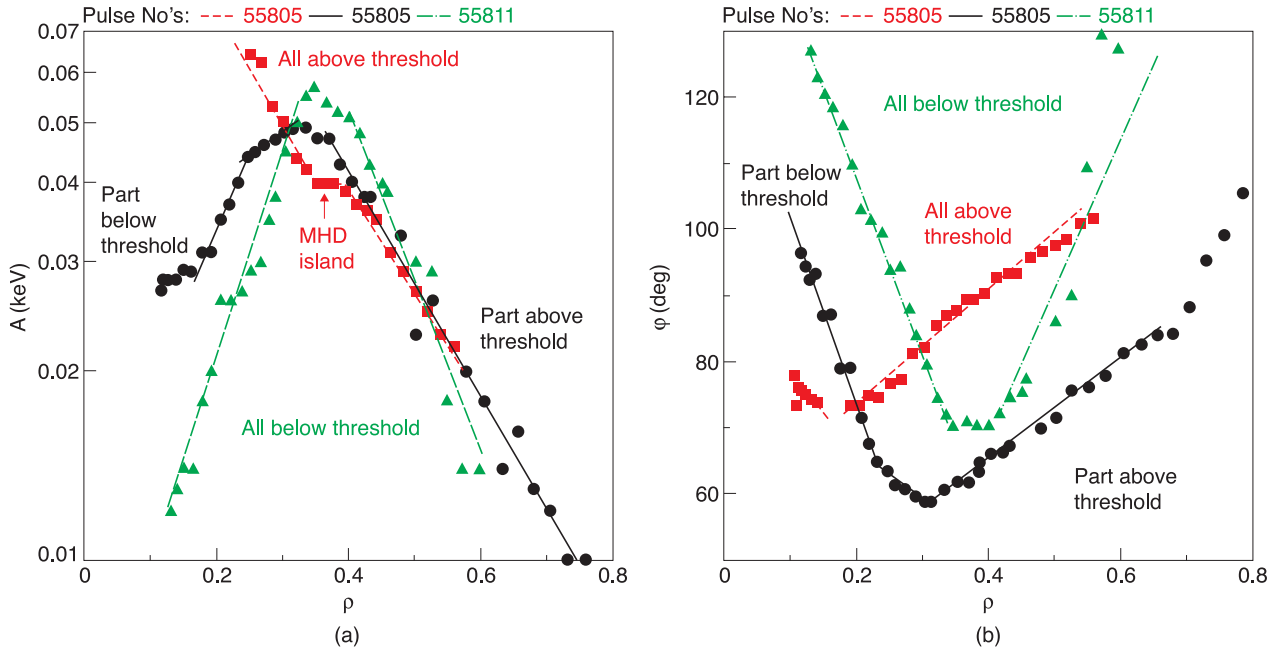
Fig. 9. Heat wave (a) amplitude and (b) phase profiles at first harmonic (15 Hz) for discharges from the heat flux scan experiment of Fig. 7. From Ref. 27.

and a measure of the degree of stiffness in different discharges.

II.F. Multimachine Comparison of Thresholds and Stiffness Levels

A set of JET discharges with T_e modulation have been analyzed with the CGM model [Eq. (7)] to deduce the values of $R/L_{T_{e,crit}}$, χ_s, and χ_0. These include L-mode and H-mode shots with different proportions of electron and ion heating. The values of χ_s versus $R/L_{T_{e,crit}}$ are plotted in Fig. 13 (updated from Ref. 23), which also shows values from ASDEX Upgrade, Tore Supra, and FTU, obtained using similar procedures and the same model within an international collaborative framework on the study of electron stiffness. The details of this intermachine comparison of stiffness are reported in Refs. 18, 23, and 36. In Fig. 13 the triangles mark discharges with significant amounts of ion heating via NBI.

The range of R/L_{T_e} thresholds is found to be the same in all machines; i.e., $R/L_{T_{e,crit}}$ lies between 3 and 8, which are typical values expected for TEMs. Figure 14 (from Ref. 36) shows a comparison between the experimental threshold values and the values predicted by a theoretical formula for TEM threshold derived in Ref. 37 from linear runs of the gyrokinetic code GS2 (Ref. 38). Figure 14 indicates fair agreement, taking into account the large uncertainties associated with both the experimental threshold and the parameters that enter the thresh-

old formula, in particular the magnetic shear. χ_s shows a larger variability (Fig. 13), being in the range $\chi_s \sim 0.2$ to 1.3. Comparing χ_s in plasmas with pure electron heating, the values are found to be rather similar among all devices. This in itself is a confirmation that the assumed gyro-Bohm normalization of the stiffness factor is supported by the experimental data and implies that hotter machines will work closer to threshold. This is indeed observed to be the case when comparing JET with other machines, and it is expected in ITER. An excursion of χ_s to higher values is observed in JET in plasmas with additional ion heating. This suggests that electron and ion channels are coupled and that large amounts of ion heating can induce a higher level of electron stiffness. Still, χ_s remains in the order of 1; i.e., the level of electron stiffness is never extremely high, and therefore models with very high electron stiffness ($\chi_s \sim 10$) such as the original version of GLF23 (Ref. 39) or IFS-PPPL (Ref. 40) should be discarded. The experimental values are in the right ballpark of stiffness levels for models such as the Weiland model[41] or GLF23 renormalized. χ_0 is found to be the quantity with larger uncertainty in its determination; therefore, no speculation on its parametric dependences can be attempted. We just note that the values obtained for χ_0 are usually rather high compared to those for neoclassical transport, suggesting that a residual turbulent transport level is still present after stabilization of the ITG/TEM branch. This is also true for residual transport in ITBs, as is further discussed in Sec. V.
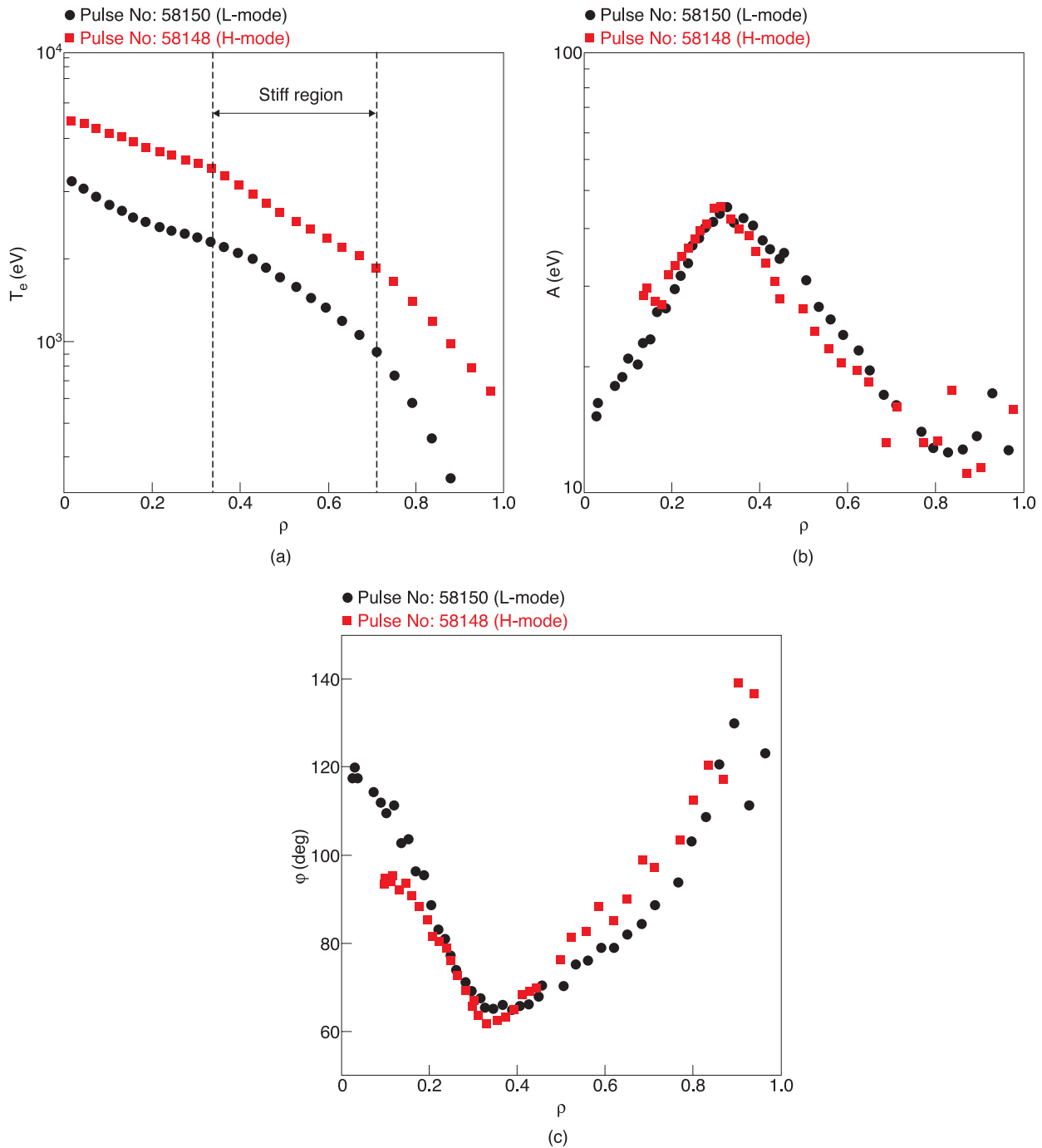
Fig. 10. Experimental profiles of (a) T_e, (b) A, and (c) φ for L-mode ($P_{NBI} = 4$ MW) and H-mode ($P_{NBI} = 14$ MW) shots. Amplitudes are normalized to the H-mode shot to allow direct comparison. $B_T = 3.25$ T, $I_p = 1.8$ MA, and $n_{e0} = 3.5$ (L-mode) and 3.2 (H-mode) $\times 10^{19}$ m^{-3}. From Ref. 28.

II.G. Temperature Profile Stiffness in JET and Implications for Global Confinement

A detailed comparison between the findings on profile stiffness from these experiments and the International Tokamak Physics Activity (ITPA) two-term scaling law for energy confinement[42] has been carried out and is described in Ref. 18. The issue here was to verify the compatibility of scaling laws with a model for the core heat diffusivity of the form of Eq. (7) with values of $\chi_s \sim 1$.
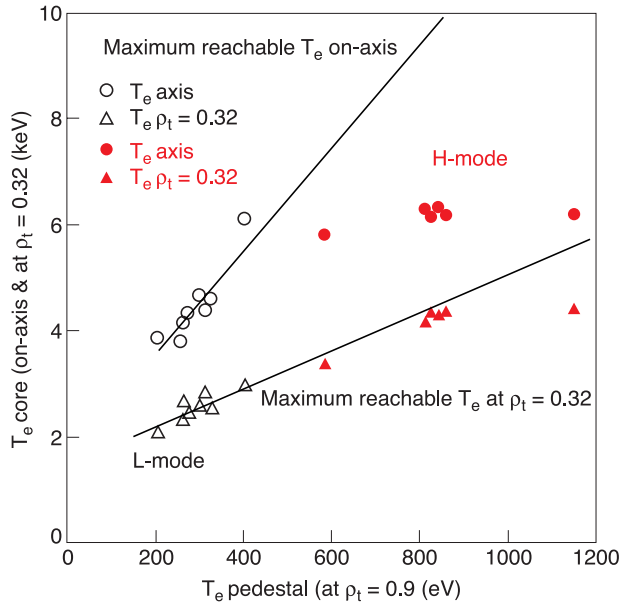
Fig. 11. Core [on-axis (circles) and at $\rho = 0.32$ (triangles)] T_e versus pedestal values. L-mode and H-mode are, respectively, open and closed symbols (3.25 T $< B_T <$ 3.45 T, 1.6 MA $< I_p <$ 1.8 MA, 2.8×10^{19} m$^{-3} <$ $n_{e0} < 3.5 \times 10^{19}$ m^{-3}, and $0 < P_{NBI} < 16.5$ MW). The lines indicate the maximum temperature achievable under the hypothesis of a threshold uniform along the radius. From Ref. 28.

Fig. 12. Normalized heat flux at $\rho = 0.2$ (larger symbols) and $\rho = 0.4$ (smaller symbols) versus R/L_{T_e} for a set of similar JET modulated shots (3.25 T $< B_T <$ 3.45 T, 1.6 MA $< I_p <$ 1.8 MA, 2.8×10^{19} m$^{-3} < n_{e0} <$ 3.2×10^{19} m^{-3}, and $0 < P_{NBI} < 14.3$ MW) characterized by the same threshold and different stiffness levels (red squares, pure electron heating; black circles, mixed ion and electron heating). The lines represent the CGM model with the choice of parameters coming from modulation best fit. Adapted from Ref. 30. (Color online)

One major warning that came from this analysis was that in general for a model as in Eq. (7), it is not correct to split the confinement into two independent terms, one for bulk and one for pedestal. In fact, this is rigorous only for a heat diffusivity that depends only on temperature gradient, not on temperature itself, unlike Eq. (7). It turns out that both for very stiff plasmas and for subcritical nonstiff plasmas, the ITPA bulk term would have a strong dependence on edge temperature, which would strongly couple it with the pedestal term. The fact that in the ITPA scaling laws the two terms are found to have very different parametric dependences implies that very stiff profiles are incompatible with ITPA results. It turns out that, in fact, the only condition in which such decoupling of bulk and pedestal terms takes place within the framework of Eq. (7) is when the level of stiffness is medium. Then, comparison of ITPA law with what would be expected from Eq. (7) yields that χ_s must be of order 1, which is exactly what is found from modulation experiments, taking into account the many sources of approximation in the analysis. Therefore, the results on stiffness described above on the basis of perturbative data are fully compatible with the ITPA two-term scaling.
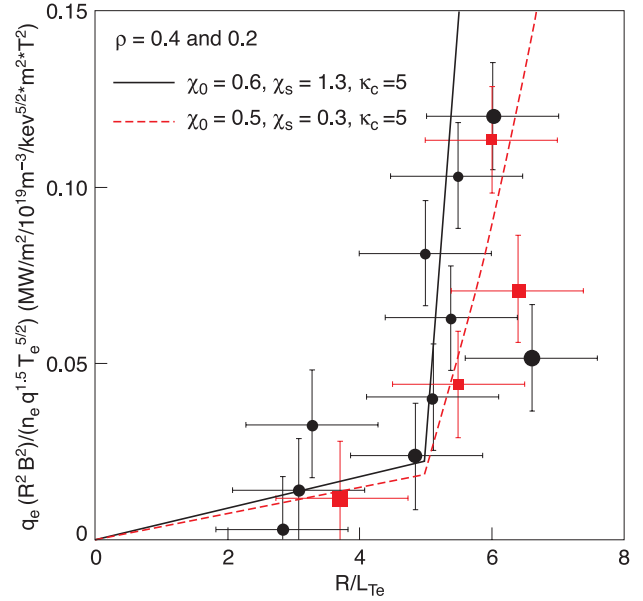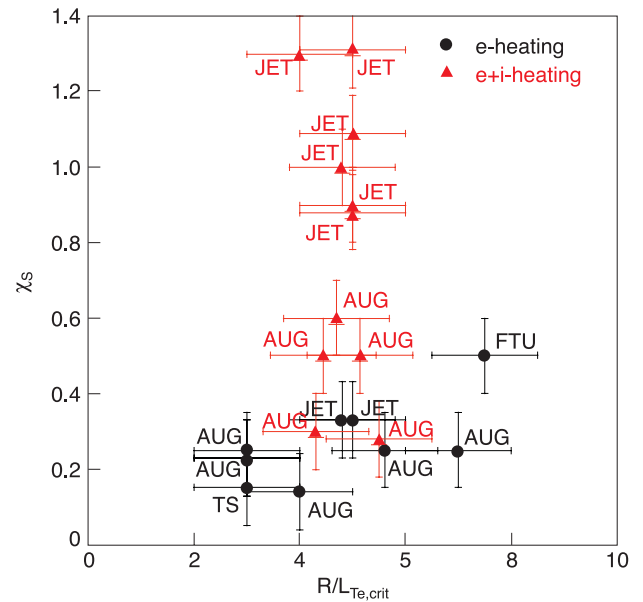

Fig. 13. Experimental values of χ_s versus $R/L_{T_{e,crit}}$ for shots with pure electron heating and with NBI (electron plus ion heating) in AUG, FTU, JET, and TS. Adapted from Ref. 23.
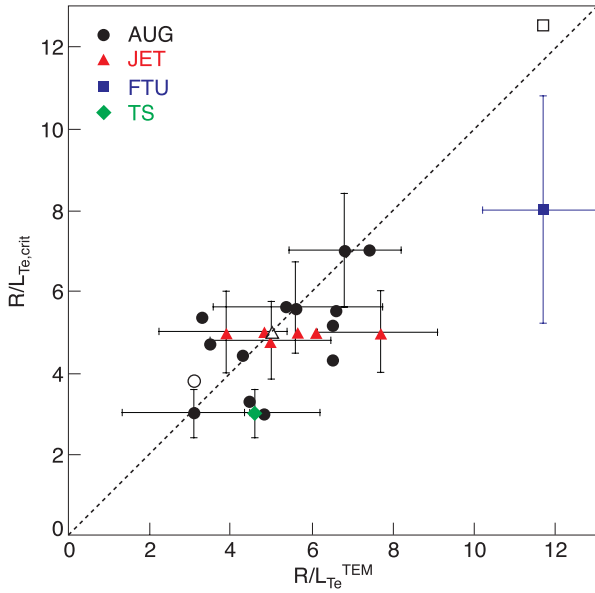
Fig. 14. Experimental threshold values in AUG, FTU, JET, and TS versus TEM threshold by predictive formula derived from GS2 (Ref. 37). Open symbols indicate the threshold from dedicated linear gyrokinetic calculations for specific discharges. From Ref. 36.

II.H. Comparison of Experimental Results with First-Principle Models

Two representative discharges from the data set described previously, i.e., shot 53822 with mainly electron heating (pure ICRH mode conversion) and shot 55809 with an additional 9 MW of NBI heating, have been selected for detailed comparison with predictions from different models.[29] For these two shots a significant difference in χ_s, measured by fitting the data with the CGM model, has been found; namely, $\chi_s = 0.3$ for 53822 and $\chi_s = 0.9$ for 55809 [they correspond respectively to one of the black JET circles and one of the red JET triangles in Fig. 13 (color online)]. The value of R/L_{T_i} increases from 3.8 in 53882 to 5.4 in 55809. In discharge 55809 the ITG instability is dominant, whereas in discharge 53822 the TEM instability starts to dominate the low-$k_\theta \rho_i$ part of the instability spectrum. ETG modes are linearly stable in these plasmas. We note here that adding NBI heating also provides additional electron heating and therefore an increase of profile stiffness due to the factor $T_e^{3/2}$ in Eq. (7). Our definition of stiffness, however, separates this effect from the intrinsic stiffness level expressed in the χ_s coefficient.

The predictive modeling was performed solving all transport equations for T_e, T_i, n_e, and J. The models under test were the Weiland model[41] (either collisionless or with collisions and electromagnetic effects included) and the Bohm–gyro-Bohm model,[13] implemented in the transport code JETTO (Ref. 43), and the GLF23 model,[39]

version 1.61, implemented in the transport code ASTRA. We note that of these models, only GLF23 and Weiland are first-principle-based models, while the Bohm–gyro-Bohm model is empirical. Moreover, in the light of recent progress in the theory of turbulent transport, it has become clear that the mixed Bohm–gyro-Bohm model shows several physics inconsistencies with recent theoretical understanding. Therefore, now in JET priority is being given to the use of first-principle-based models such as Weiland or GLF23. The use of the mixed Bohm–gyro-Bohm model as an empirical model is now limited to those situations in which first-principle models still do not provide an adequate reproduction of data, such as in the presence of ITBs or when a numerically robust model is essential, such as for real-time-control studies or edge–core–integrated modeling. These are, nevertheless, valid reasons, in addition to the extensive use of the model in past JET work, to include the model in the present review of JET transport work and in the test of validity described in this section.

In the following the results of the best-fitted simulation with the empirical CGM model will be used as a reference for comparison with the results obtained by these models. Figure 15 (Ref. 29) shows for the pure electron–heated discharge 53822 the predicted steady-state T_e, T_i, and n_e profiles with the three models: Weiland collisional, Bohm–gyro-Bohm, and GLF23. The same is shown in Fig. 16 (Ref. 29) for shot 55809 with additional NBI heating. The Weiland collisionless model has been discarded because it tends to overpredict the density peaking (compare also Ref. 44). From Fig. 15 it is evident that GLF and to a lesser extent Weiland overestimate T_i in the case of 53822. However, this does not prevent further analysis of modulation data since it has been checked by forcing the absolute T_i value (but keeping R/L_{T_i} constant) that this does not affect the amount of electron stiffness. The use of GLF with predictive density has turned out to be very cumbersome. The model is very unstable and prone to crashes for both shots, but especially for 53822. For 55809 it yields to the formation of an ITB in the density profile, which is not seen in experiment. Therefore, the simulations with GLF23 shown here have been made by fixing the density profile close to experiment. This should not hinder the predictions of the model for heat transport since it is expected that for the R/L_n values of these shots ($R/L_n \sim 2.2$ and $R/L_n \sim 1$, respectively, for 53822 and 55809), the density gradient should not contribute significantly to heat transport.

The performance of the various models in reproducing the modulation amplitude and phase profiles is illustrated in Figs. 17 and 18 (Ref. 29). The best performing model appears to be the collisional Weiland model, which reproduces reasonably the modulation data, although the third harmonic is highly noisy. In particular, the simulation of shot 53822 is very good, but for shot 55809 the model, although reproducing the experimental trend of increasing stiffness with R/L_{T_i}, still underestimates

Fig. 15. Steady-state experimental profiles of T_e, T_i, and n_e for shot 53822 (dots) and simulations using various models: empirical CGM (solid line), Weiland with collisions (short-dashed line), Bohm–gyro-Bohm (dotted line), and GLF23 (long-dashed line). $B_T = 3.5$ T, $I_p = 1.8$ MA, and $n_{e0} = 3.5 \times 10^{19}$ m^{-3}. From Ref. 29.

the level of stiffness compared to experiment. The Bohm–gyro-Bohm model performs less well in reproducing the slopes, and GLF23 performs very badly for shot 53822, whereas it is comparable to the Weiland model for shot 55809.

With regard to the observed increase of electron stiffness with ion heating, we note that this is qualitatively reproduced by the Weiland model, although the simulated trend is quantitatively less strong than in the exper-

iment. This has been further cross-checked by varying the NBI power arbitrarily within a simulation of the same discharge.[29] This issue is being further explored using nonlinear electrostatic fluid turbulence simulations.

In summary, although in principle for electron transport studies the situation of pure electron heating (when electron transport is driven only by the TEM instability) is easier to handle than the one with mixed type of heating (when electron transport is driven both by TEM and
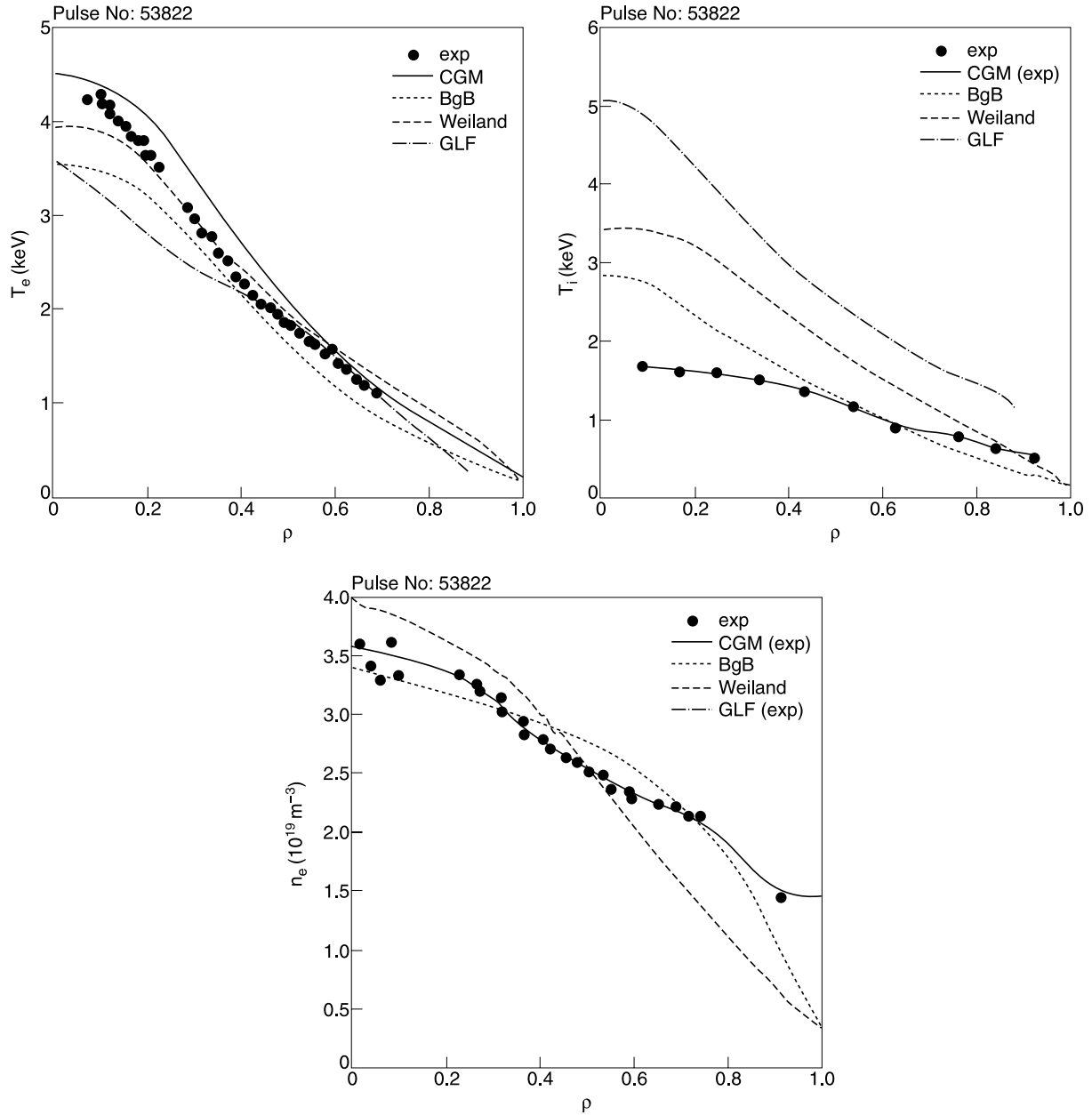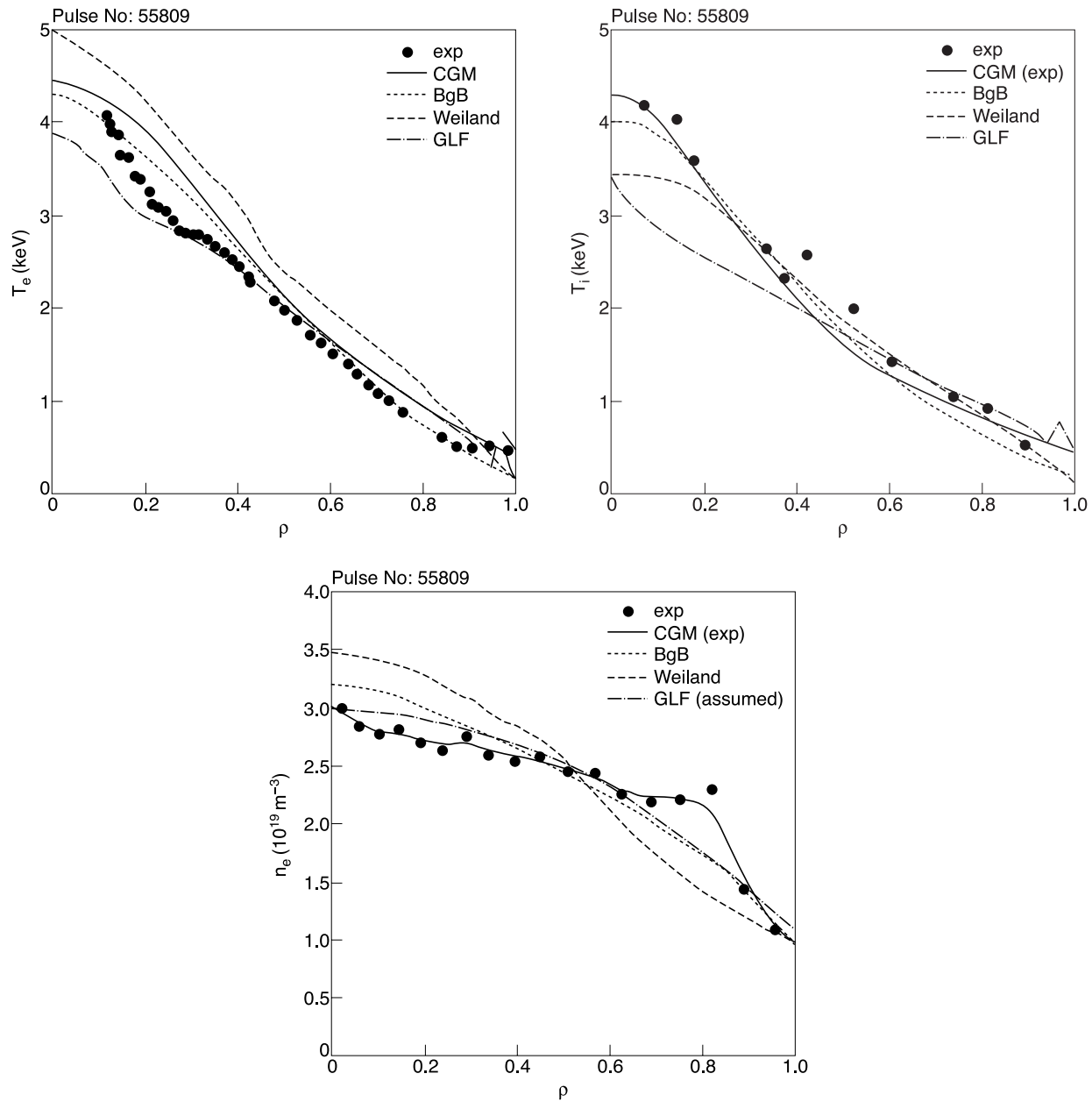
Fig. 16. Steady-state experimental profiles of T_e, T_i, and n_e for shot 55809 (dots) and simulations using various models: empirical CGM (solid line), Weiland with collisions (short-dashed line), Bohm–gyro-Bohm (dotted line), and GLF23 (long-dashed line). $B_T = 3.25$ T, $I_p = 1.6$ MA, and $n_{e0} = 2.7 \times 10^{19}$ m^{-3}. From Ref. 29.

ITG, with a strong coupling in the instabilities between the ion and the electron dynamics), both first-principle models, Weiland and GLF23, do not perform well in the first case (particularly GLF23), whereas they have similar, satisfactory performance in the second case. This difficulty may be ascribed to the fact that the ion dynamics is much easier to capture in a fluid description than that of trapped electrons. In any case, further work in the direction of improving existing models and validating them is still needed before a fully validated model to be

safely used for ITER predictions is achieved. A similar conclusion was reached also in past work simulating cold-pulse propagation in JET (Ref. 45) and in recent work on model performance in reproducing pure steady-state JET profile data in (Refs. 46 and 47). Nonlinear turbulence simulations are indeed a valid tool to facilitate the understanding of specific physics mechanisms, but their use on JET data has been rather limited so far, especially for gyrokinetic codes, due to their extreme computational needs. It is clear, however, that for the moment
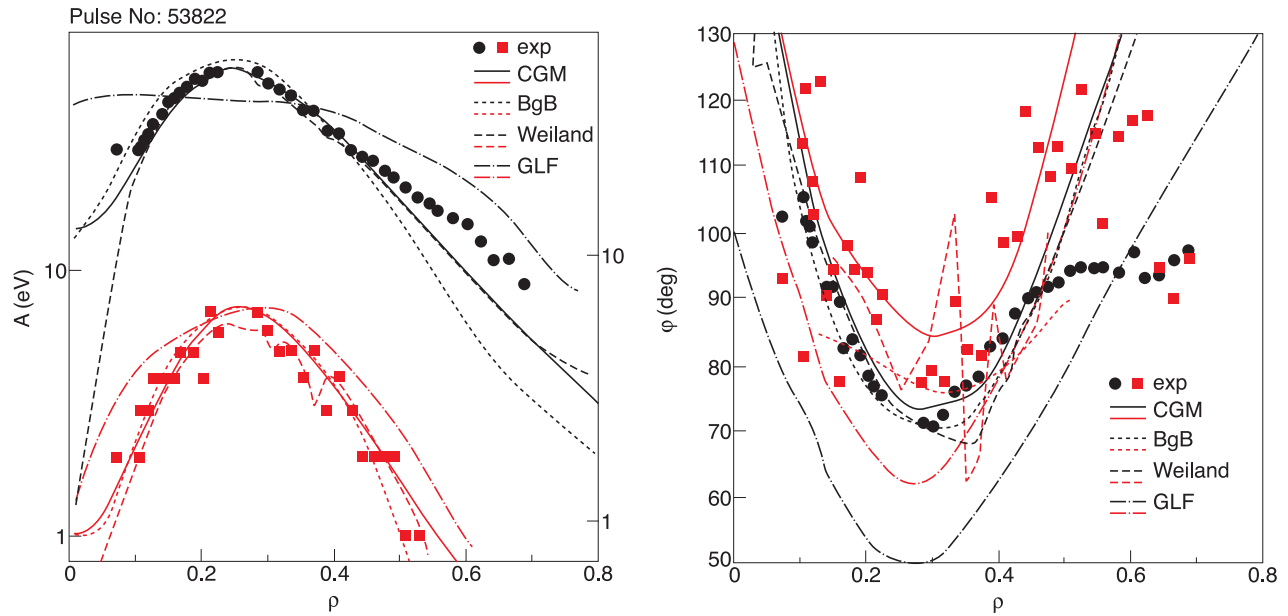
Fig. 17. Experimental profiles (dots) of amplitude and phase at first (black circles) and third (red squares) harmonics for shot 53822 and simulations using various models: empirical CGM (solid line), Weiland with collisions (short-dashed line), Bohm–gyro-Bohm (dotted line), and GLF23 (long-dashed line). From Ref. 29. (Color online)
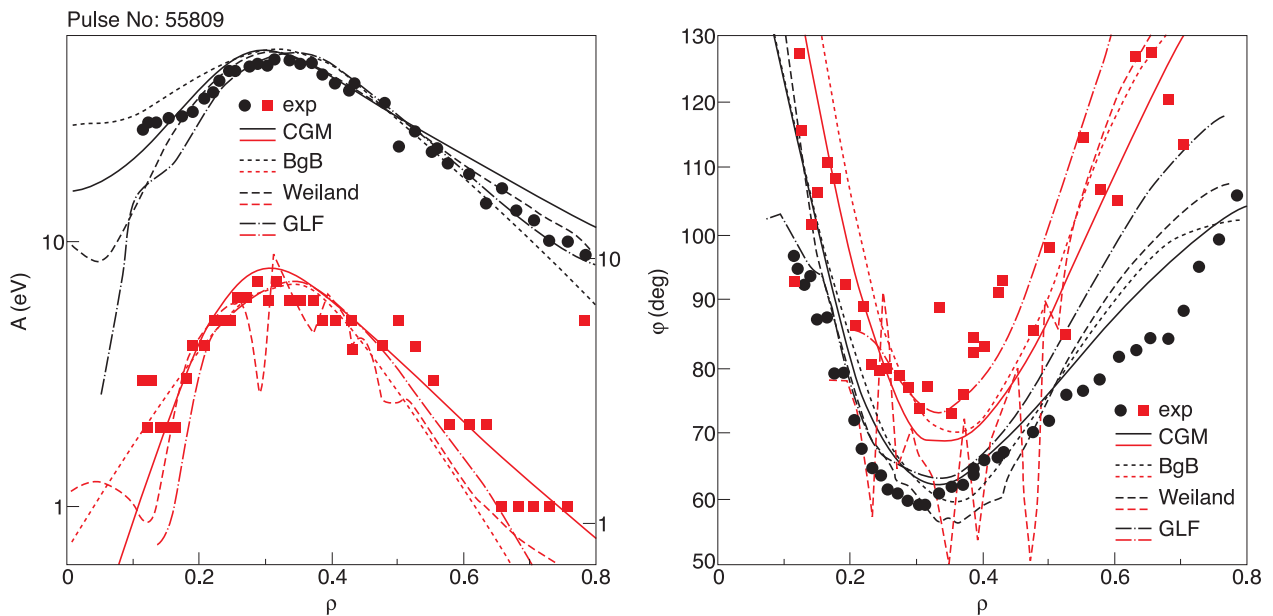
Fig. 18. Experimental profiles (dots) of amplitude and phase at first (black circles) and third (red squares) harmonics for shot 55809 and simulations using various models: empirical CGM (solid line), Weiland with collisions (short-dashed line), Bohm–gyro-Bohm (dotted line), and GLF23 (long-dashed line). From Ref. 29. (Color online)

they do not represent a reliable tool for full predictive modeling and extrapolation to ITER predictions, as discussed also in Ref. 47, although they are a promising prospect for the future. Finally, we observe that even restricting the scope of predictive modeling to prediction of the R/L_T thresholds alone (which may still be rather useful given the high level of stiffness expected on ITER on the basis of JET data), there are nevertheless various models available with different parametric dependences foreseen for thresholds, and none of them has been

systematically validated against experimental data so far, which calls for intense activity of theory-experiment comparison in the near future.

II.I. The Issue on Nonlocality from JET Cold-Pulse Propagation and the Concept of Turbulence Spreading

As a final point, we would like to come back to the observation of fast cold-pulse propagation always observed in JET, as mentioned in Sec. II.B. Within the framework of a local diffusive transport, these observations would be easily consistent with the picture of a stiff transport above a critical gradient, such as the one proposed in the previous sections on the basis of modulation results. The issue then becomes a quantitative one, i.e., whether the stiffness level deduced from T_e modulation is high enough to account for the propagation of a T_e cold pulse from edge to core in 1 to 4 ms, as observed experimentally [e.g., in Fig. 19a (Ref. 27), an upper limit of 4 ms for the delay between $\rho = 0.87$ and $\rho = 0.11$ can be set taking into account noise]. To clarify this subtle point, a dedicated experiment has been devised in a JET L-mode plasma in which T_e modulation and T_e cold pulse were performed in the same discharge and with off-axis ICRH in mode conversion so that the plasma would go below threshold around $\rho = 0.35$ (Ref. 27). The comparison between the two perturbations yielded the surprising results that although T_e modulation undergoes a slowing down when propagating in the region below threshold, as

expected, the T_e cold pulse does not and keeps propagating fast also in the region below threshold. Figure 19a shows the experimental data and Fig. 19b shows a simulation using the CGM model with the parameters extracted from the modulation just before the cold pulse. It is clear that the stiffness parameters measured by modulation in this case would predict a delay for the cold pulse of about 22 ms between the same radii, which is much longer than in the experiment. This indicates that the local critical gradient paradigm described above, although providing a very good framework to explain most transport observations of core heat transport in JET, may need to be further complicated to account for these observations that call for a nonlocal transport mechanism.

One possible idea put forward to explain the asymmetry of behavior between cold pulse and modulation is that of turbulence spreading.[48,49] In this model the local intensity of the turbulent fluctuations is used to determine the fluxes of the transported quantities. The turbulence itself is a transported quantity and can spread into linearly stable regions of the plasma, raising the transport there to high levels. The application of such a model to JET shot 55809 is described in Ref. 50. It was found that indeed the cold pulse delay can be reduced while preserving a good fit of T_e modulation, however, from about 23 ms predicted by CGM to about 18 ms, still much longer than experimentally measured. Further investigation in this direction is therefore required, as well as exploration of other models for nonlocal transport, such as those based on the use of fractional derivatives.[51,52]
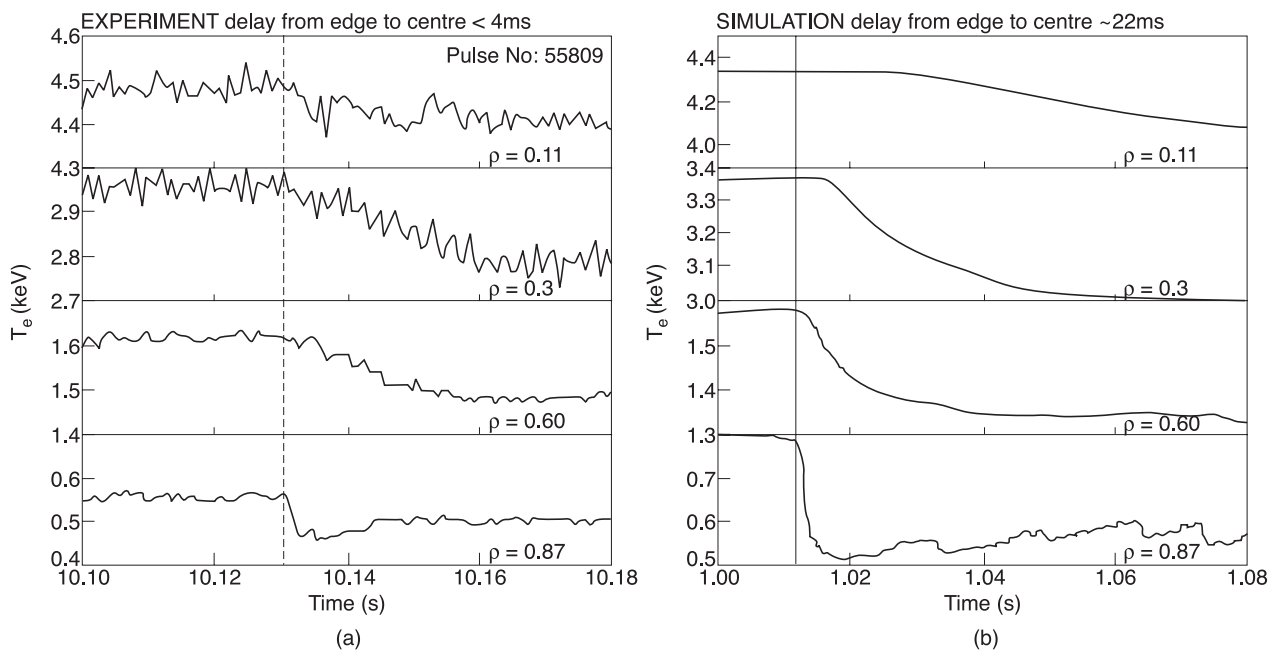

Fig. 19. (a) Experimental and (b) simulated [using critical gradient model Eq. (7)] T_e time traces for cold-pulse propagation in shot 55809. The X-axis range of the simulation plot has an arbitrary time offset. From Ref. 27.

II.J. Ion Heat Transport Studies in JET

Due to lack of sufficient time resolution of the charge-exchange recombination spectroscopy (CXRS) diagnostic, detailed perturbative studies of ion heat transport could not be performed to improve the information from steady-state data to address the issues of stiffness, threshold, and validation of theoretical models. Some initial effort in this direction has started recently but is too preliminary to be included in this review. It is, however, a very relevant topic to be addressed in the near future.

The existence of stiffness also in the ion heat channel, besides being predicted theoretically, is confirmed experimentally by the correlation found between edge and core temperatures, as shown for electrons in Fig. 11. The analogous plot for ions is shown in Fig. 20 (Ref. 28). In the absence of dedicated heat flux scans or T_i modulation studies, however, nothing can be safely assessed about ion threshold or stiffness levels.

The most complete study of JET ion heat transport based on steady-state data under the assumption of the existence of a critical ion temperature gradient length is reported in Ref. 53. Figure 21 (Ref. 53) shows an example of the dependence of the ion heat flux on R/L_{T_i} for a typical H-mode discharge. This plot resembles the one for electrons in Fig. 12 and points to the existence of a threshold value for R/L_{T_i} that the plasma cannot exceed,

Fig. 21. Normalized ion heat flux as a function of R/L_{T_i} for JET H-mode shot 51860. The plot has been obtained from the radial profiles of the respective quantities, covering a radial range of $\rho \sim 0$ to 0.7. From Ref. 53.

Fig. 20. Core [on-axis (circles) and at $\rho = 0.32$ (triangles)] T_i versus pedestal values for the same discharges as in Fig. 11. L-mode and H-mode are, respectively, open and closed symbols. The lines indicate the maximum temperature achievable under the hypothesis of a threshold uniform along the radius. From Ref. 28.

thereby suggesting very strong stiffness in the ion channel. However, a very delicate point in such interpretation is that the excursion of the ion heat flux on the vertical axis of Fig. 21 is obtained from the increase of the heat flux with radius using profiles at different radial positions from $\rho = 0$ to $\rho = 0.7$ within the same shot, which is unlike in Fig. 12, where the heat flux variation was obtained by varying the power deposition profile in a given plasma region in a set of similar shots, with, in addition, the T_e modulation on top. Because the threshold is likely not uniform in space, the slope of the curve in Fig. 21 is the mixed result of stiffness and radial variation of the threshold, thereby falsifying the quantitative determination of the actual ion stiffness level. In particular, the expected dependence of the ITG threshold on q, such that the increase of q in the outer region would lead to a reduction of the threshold, may contribute to giving an apparently higher stiffness in plots such as the one in Fig. 21. In Ref. 53 an attempt also was made to estimate the impact of T_e/T_i and $\omega_{E\times B}$ on the threshold, but the data did not allow separation of these two effects. These studies therefore will have to be performed using methodologies similar to those used for electrons, now that at JET an improved CXRS system is available with time resolution of ~ 5 to 10 ms and spatial resolution of ~ 7 cm, and making use of the versatility of the JET heating system to decouple the effect of T_e/T_i from that of rotation.

II.K. Conclusions

This section reviews progress in core heat transport understanding in JET since early observations in the JET Joint Undertaking to recent experimental campaigns under the European Fusion Development Agreement (EFDA). The idea of a threshold in the inverse critical gradient length (R/L_{T_e}) described by theory of electrostatic instabilities is consistent with JET experimental results and implies the existence of some degree of stiffness of temperature profiles above threshold. For electrons, thresholds and stiffness factors have been measured via perturbative experiments. Thresholds are found to be consistent with theory predictions of TEM, and stiffness levels are found to be of the same magnitude as those of other devices in pure electron–heated plasmas, with a trend to increase for significant levels of ion heating. Ion stiffness studies have just started. These observations and the dependence of stiffness on temperature lead to the expectation that stiffness will dominate temperature profiles in ITER conventional scenarios. Some attempts to validate existing 1-D transport models against perturbative data or steady-state data yield mixed results, calling for further work before a validated model suitable for extrapolation to ITER can be achieved. Finally, although a critical gradient paradigm can explain the majority of transport observations in JET, the peculiar evidence of fast propagation of cold pulses and their difference in behavior with respect to temperature modulation suggests that some nonlocal features may need to be introduced, either via the concept of turbulence spreading or that of fractional derivatives.

III. CORE PARTICLE AND IMPURITY TRANSPORT STUDIES IN JET

III.A. Introduction

Particle and impurity transport are no less important for reactor plasmas than are the other transport channels. They control the transport of fuel to the hot core and they transport He ash away from it. Impurities are usually seen as unwanted loss sources in the form of radiation, in addition to diluting the fuel, especially when accumulating in the plasma core. Impurities with suitably chosen atomic numbers may increase radiation losses near the last flux surface and in the divertor, with the beneficial effect of reducing the heat loads to the divertor wall components.

JET has conducted systematic experimental and modeling investigations that are crucial for the understanding of particle and impurity transport. These include the injection of trace amounts of tritium to study fuel transport, the injection of gases such as He, Ne, and Ar, as well as of small amounts of metals such as Ni, to study impurity transport, and an assessment of the ubiquitous convective phenomena, which control the peakedness of electron density, fuel density, and impurity density profiles. As a result of this work, carried out by a substantial number of contributors at JET and many collaborating institutions, we are currently in a much better position than we were a few years ago to extrapolate particle and impurity transport behavior to fusion reactor conditions and to identify issues that require further investigation.

III.B. Density Profile Behavior

In stationary conditions, electron density profiles are generally moderately peaked [with peaking factors $n_e(0)/\langle n_e \rangle$ in the range 1 to 2 in JET]. This observation is in stark contrast with the former general expectation of a flat density profile in ITER (Refs. 54 and 55). Since peaked density profiles would provide a significant boost of fusion power in a reactor, for a given average density and stored energy, the behavior of density profiles has received increasing attention in recent years. In steady state, density gradients are determined by a balance of sources, diffusion, and convection such that the density gradients satisfy $1/L_{ne} = \Gamma_s/(n_e D) - v/D$, where Γ_s is the outward flux associated with the particle source, v is the convective or pinch velocity, D is the particle diffusion coefficient, and $1/L_{ne} = -\nabla n_e/n_e$. Both neutral beam and edge fueling may contribute to the source. Neoclassical pinches, notably the Ware pinch, $v_W \propto E_\phi/B_\theta$ (Ref. 56) (which is inward in the usual case when the plasma current and the toroidal electrical field are in the same direction) and anomalous pinches due to drift wave turbulence[14,41,57] can also allow us to sustain density gradients, even in the absence of sources. The latter comprise the curvature pinch (also referred to as turbulent equipartition), with $v/D \approx -c_q \nabla q/q$ and thermodiffusion, characterized by $v/D \approx -c_{T_e}/L_{T_e}$, where $1/L_{T_e} = -\nabla T_e/T_e$. Explicit expressions for the coefficients c_T and c_q are only obtained from simple models and are typically smaller than unity. Thermodiffusion is sensitive to the direction of mode propagation; for electrons it is outward for modes rotating in the electron diamagnetic direction (such as TEMs) and inward for modes in the ion diamagnetic direction (ITG modes).

The most strongly peaked density profiles in ELMy H-modes are observed at opposite ends of the JET operating domain, in very collisional discharges at high Greenwald fraction, $1.6 \gtrsim N_G \gtrsim 0.8$ (Ref. 58), often with Ar seeding,[59] and at $N_G \lesssim 0.3$, with collisionalities approaching those expected for ITER (Ref. 60). The former are rarely stationary and are accompanied by a loss of sawtooth activity and core impurity accumulation.[61] The observation of increased peaking toward low collisionality agrees with an earlier study on ASDEX-Upgrade.[57] Although this observation suggests that ITER may have a substantially peaked density profile, this conclusion should

be drawn only if the underlying mechanisms are identified. In particular, if this trend with collisionality results from the Ware pinch or from particle sources, then the expectation for ITER would be a flatter density than that obtained in JET.

III.B.1. Ware Pinch and Neutral Beam Fueling

The loop voltage is highest, and hence the Ware pinch is strongest, in highly collisional, resistive plasmas.[58,59,61] Figure 22 shows the results of a transport analysis of such a discharge, in which χ_{eff} was obtained from the power balance and the diffusion coefficient D was obtained as $D = (\Gamma/n_e + |v_W|)L_{n_e}$, assuming no anomalous particle pinch.[58] For the example chosen, these contributions are of similar magnitude, $\Gamma/n_e \approx 0.06$ m/s and $|v_W| \approx 0.04$ m/s at $\rho = 0.4$. In these plasmas a combination of NBI fueling and the Ware pinch can account for density peaking if $D/\chi_{eff} \sim \frac{1}{4}$ is assumed for the core region[58] ($\rho < 0.5$). In the confinement zone ($\rho \gtrsim 0.5$), lower values of D/χ_{eff} are necessary for consistency with a model including only NBI sources and the Ware pinch.

At lower density, since temperatures are higher, the Ware pinch decreases, beam penetration improves, and the NBI source term dominates over the former. We may relate the effective heat diffusivity $\chi = -q/(n_e\nabla T_e + n_i\nabla T_i) \approx -q/(2n_e\nabla T_e)$ to Γ_{NBI} and v_W as follows, where q is the total heat flux and gradients are understood as flux surface averages:

Pulse No: 52979

$\chi_{eff/4}$

D

v_{Ware}
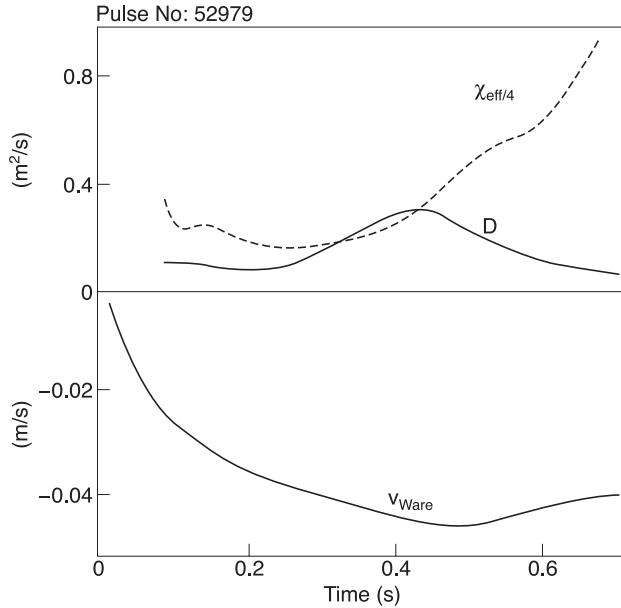
Fig. 22. Transport analysis of an ELMy JET H-mode discharge at high collisionality (from Ref. 58). $I_p = 1.9$ MA, $B_T = 2$ T, $N_G \approx 1$, $\langle n_e \rangle \approx 8 \times 10^{19}$ m^{-3}, $T_e(0) = 2.1$ keV, and $\nu_{eff}(0.5) \approx 1.5$.
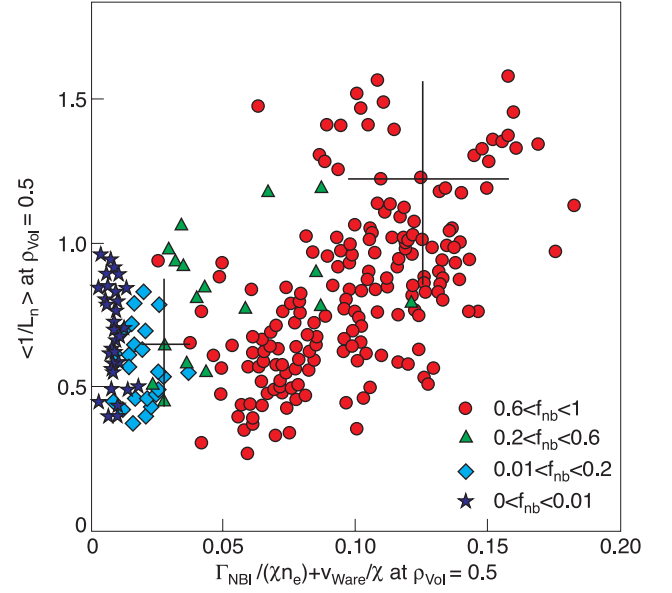
Fig. 23. $1/L_{n_e}$ versus $\Gamma_{NBI}/(\chi n_e) + |v_W|/\chi$. Symbols refer to fraction of NBI heating $f_{nb} = P_{NBI}/P_{tot}$ (from Ref. 62).

$$\frac{\nabla n_e}{n_e} = \frac{\Gamma_{NBI}}{Dn_e} + \frac{v_W}{D} \approx \frac{\chi}{D}\left(\frac{T_e}{q/\Gamma_{NBI}}\frac{2\nabla T_e}{T_e} + \frac{v_W}{\chi}\right) . \quad (10)$$

For entirely beam-heated plasmas, $E_b = q/\Gamma_{NBI}$ is the average beam energy ($\sim$90 keV at JET). For a typical NBI-heated plasma with $1/L_{T_e} \sim 2$ m^{-1} and $T_e \sim 3$ keV at midradius, D would have to be $\sim$10 times smaller than χ in order to explain a density gradient $1/L_{n_e} \sim 1$ m^{-1}. In Fig. 23, we plot the flux surface–averaged experimental $1/L_{n_e}$ versus $\Gamma_{NBI}/(\chi n_e) - v_W/\chi$, evaluated at midradius for a large variety of H-modes.[62] The contribution of the Ware pinch is comparable to, or larger than, the NBI contribution only for $P_{NBI} < 2$ MW, corresponding typically to $f_{nb} = P_{NBI}/P_{tot} < 0.2$, where P_{tot} is the total heating power. Considering also ICRH-dominated discharges and ICRH-only discharges (stars in Fig. 23), it becomes plain that there is no obvious correlation between $1/L_{n_e}$ and $\Gamma_{NBI}/(\chi n_e) - v_W/\chi$. In addition, the magnitude of D/χ required would have to be implausibly low, $\sim$10^{-2} for most of the ICRH-only H-modes. We conclude that the combined beam fueling and Ware pinch are unable to account for the observed density gradients in the confinement zone; however, beam fueling may still be a significant contributor, depending on the real value of D/χ.

III.B.2. Edge Particle Source

Whereas the neutral beam source can be calculated with codes such as PENCIL (Ref. 63) and TRANSP (Ref. 64), the absolute magnitude of the source associated with edge neutrals is more uncertain. Although the

mean-free-path of cold neutrals is far shorter than the JET minor radius, deuterium (or hydrogen or tritium) neutrals can penetrate to the bulk via a chain of charge exchange reactions with deuterium ions. The average number of steps is given by the ratio of the rate coefficients for charge exchange and ionization, typically around 4 for deuterium ions in deuterium plasmas at temperatures of a few keV. For helium neutrals this figure drops to near 0.5 because of the low cross section for double charge exchange. Penetration of deuterium edge neutrals into JET plasmas has been modeled with neutral particle transport codes such as AURORA3 (Ref. 65), FRANTIC (Ref. 66), and KN1D and DOUBLE (Ref. 67). These codes also predict fluxes of energetic neutrals escaping from the plasma and the brilliance of D_α radiation, which can serve to "calibrate" the calculated sources by comparison with measured levels of radiation or neutral particle fluxes. Since the above codes assume simplified 1-D or two-dimensional (2-D) geometries, with no provisions for asymmetries and inhomogeneities in the edge source distribution and edge plasma parameters (such as are introduced by a divertor), absolute estimates of core fueling by edge neutrals are still very uncertain. However, all of them predict a shallow penetration of neutrals. Calculations using FRANTIC and the measured D_α radiation have nonetheless suggested that the edge source may be sufficient to account for the moderate density gradients established in JET if the D_α emission from the divertor, which exceeds the main chamber D_α emission by an order of magnitude, is included.[66] As a result of such uncertainties, some of the modeling treats the absolute magnitude of the edge source as an adjustable parameter.[68] If peaked density profiles are to be explained without introducing a pinch, the calculated particle flux Γ_s has to match the diffusive flux $-D\nabla n$, where D itself is generally not known. Turbulent drift wave theory suggests,[14] however, that D may be taken to be roughly proportional to the heat diffusivity χ_{eff}. If this is correct, modeling the density profile without a pinch fails because Γ_s and $-D\nabla n$ cannot be made to match over the full profile,[69] no matter what the absolute values of Γ_s and D are, as shown in Fig. 24. Density profiles sustained only by the neutral source would be much flatter than generally observed. The shallowness of the neutral penetration has been confirmed by gas modulation experiments.[65] These experiments demonstrate the presence of an inward pinch proportional to the diffusion coefficient with $R_0 v/D \approx -2.4$. JETTO modeling has also confirmed that the edge source and the Ware pinch are insufficient for explaining density peaking.[70]

A further confirmation of the relative unimportance of the edge particle source has been obtained in He plasmas with a residual deuterium concentration of only $\sim 10\%$. Because of the low cross section for double charge exchange, neutral penetration by charge exchange is practically absent in He plasmas. Despite this fundamental
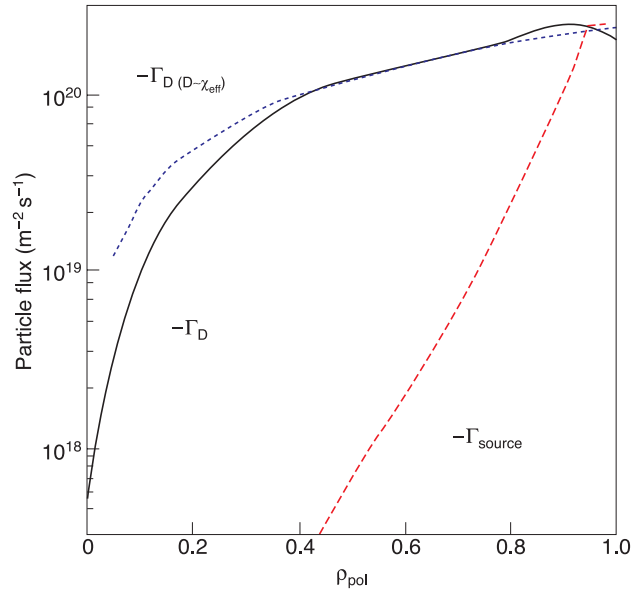
Fig. 24. DOUBLE simulation for a JET H-mode discharge (58114, with $t = 57.5$ s, $I_p \cong 2.5$ MA, $\langle n_e \rangle \cong 7 \times 10^{19}$ m^{-3}, $B_T \cong 3.5$ T, $v_{eff}(0.5) \cong 1$, and $n_{e0}/\langle n_e \rangle \cong 1.25$) of particle flux due to the edge neutrals (labeled Γ_{source}) and electron diffusive flux (labeled Γ_D) from experimental electron density gradient assuming $D(\rho) = \chi_{eff}(\rho = 1)(\rho^2 + 0.1)$ and $D(\rho) \propto \chi_{eff}(\rho)$. From Ref. 67.

difference, the peaking factor in He plasmas is no lower than that in D plasmas produced under otherwise identical conditions.[67]

III.B.3. Density Peaking in L-Modes

The density profiles in a range of JET discharges have been modeled using the transport code JETTO. Figure 25 (Ref. 71) shows an example of results for a low-density L-mode plasma with $\langle n_e \rangle \approx 1 \times 10^{19}$ m^{-3} and $T_{e0} \cong 6$ keV, heated only with 4 MW of ICRH. The figure compares the steady-state experimental profile to profiles simulated using the empirical Bohm–gyro-Bohm model without an anomalous convective term and with convective terms of the form $v_a = -c_T D/L_{T_e}$ and $v_a = -c_q D\nabla q/q$, with $c_T = 0.25$ and $c_q = 0.75$. The functional forms are inspired by theory and represent thermodiffusive and curvature pinches. The diffusion coefficient in JETTO is empirically related to the electron and ion heat diffusivities as $D = S(r)\chi_i\chi_e/(\chi_i + \chi_e)$, where the form factor $S(r)$ decreases from 1 at $r = 0$ to 0.3 at the last closed flux surface. Results from the physics-based Weiland model with and without off-diagonal terms (which represent convective transport) are also shown. The density gradients obtained without an anomalous pinch are mostly due to the edge particle flux, modeled using

Fig. 25. Modeling of density profiles in an ICRH-heated L-mode discharge (51034, with $I_p = 2.3$ MA, $B_T = 2.6$ T, $N_G \approx 0.2$, $\langle n_e \rangle \approx 1.3 \times 10^{19}$ m^{-3}, $T_e(0) \approx 5$ keV, $\nu_{eff}(0.5) \approx 0.2$, and $q_{95} \approx 3.3$). From Ref. 69.
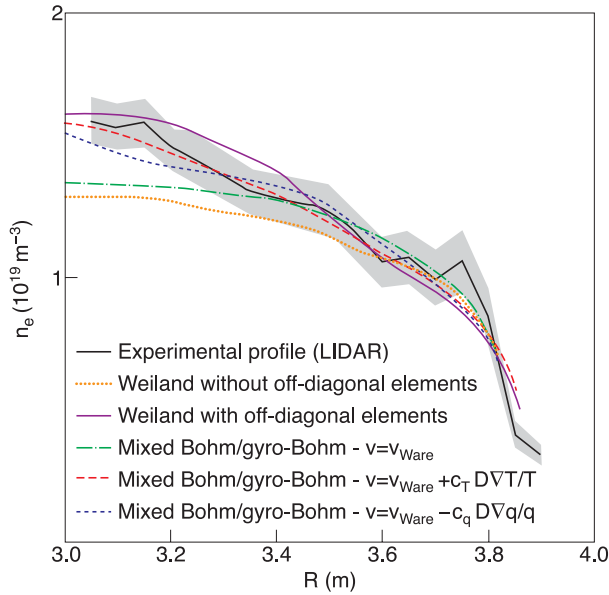
FRANTIC. While profiles modeled without an anomalous pinch fall short of the peaking observed, fair agreement is obtained when anomalous pinches are allowed for. This modeling, however, cannot answer the question of the relative importance of thermodiffusion and the curvature pinch.

A series of discharges with partial and complete lower hybrid current drive (LHCD) and no NBI has provided clear signatures of the dominance of a curvature-type pinch in L-modes at positive magnetic shear.[60,72] In these plasmas, which had constant $q_{95} = 8$, the addition of up to 3.6 MW of LH power deposited near $r/a = 0.4$ led to a broadening of the current profile and a reversal of the magnetic shear for $r/a < 0.4$ for $P_{LH} > 2.5$ MW. The core particle source from edge neutrals, as determined by KN1D, was insufficient to account for the peaked density profiles. The density profile broadened in close relation with the current profile, $n_{e0}/\langle n_e \rangle \approx 1.6 l_i$, as expressed by the internal inductance l_i (Fig. 26). In the regions of positive shear, the density profiles are in good agreement with the simplest of theoretical models, Turbulent Equi-Partition, as introduced by Ref. 73. The density gradients there, however, are significantly more pronounced than predicted by more recent theoretical models.[14,74,75] The symbols refer to normalized temperature gradients and show that there is no dependence that would be suggestive of a thermodiffusive pinch (whether temperatures are measured by lidar Thomson scattering or ECE). There are also no dependencies on collisionality (unlike in H-modes), electron density, and loop voltage. The den-

sity profiles remain peaked at zero loop voltage, confirming investigations in fully current driven discharges in TCV (Ref. 69) and Tore Supra.[76] A survey of other types of L-modes in JET (ICRH, NBI, and ohmic) also yields a rough scaling with l_i, $n_{e0}/\langle n_e \rangle \sim 1.4 l_i$, and no other discernible dependencies.

III.B.4. Density Peaking in H-Modes

Using measurements from a profile database (JET-PEAK) of a wide variety of JET H-modes, including hybrid scenarios, scalings of the peakedness of the density profiles suitable for extrapolation to ITER were developed.[62] Figure 27 shows the density profile peaking factor $n_e(0)/\langle n_e \rangle$ against the effective collisionality $\nu_{eff} \cong 10^{-14} R Z_{eff} n_e / T_e^2$ (T_e in eV) at midradius in stationary ELMy discharges over the entire JET operating domain for the same data as in Fig. 23. JETPEAK contains equilibrium profiles from EFIT reconstructions and particle and power deposition profiles, allowing steady-state heat and particle balances to be computed for each of the 291 time-slice samples in the H-mode database. Table I shows the range of variation of the most important number of dimensional and dimensionless parameters, which encompasses the entire JET operational domain.

The parameters that are the most strongly correlated with $n_{e0}/\langle n_e \rangle$ and R/L_{n_e} are $N_G = 10^{-14} \pi a^2 \langle n_e \rangle / I_p$, ν_{eff}, ν^*, and $\Gamma^* = \Gamma_{NBI}/(\chi n_e)$. Correlations with R/L_{T_e} (whether measured by lidar Thomson scattering or ECE), R/L_{T_i}, and l_i are weak, and no correlation is found with ρ_e^*. No correlation of R/L_{n_e} with magnetic
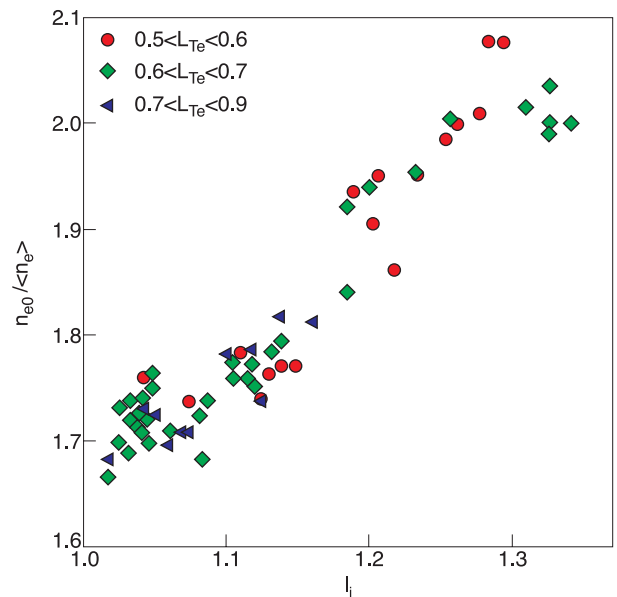

Fig. 26. Dependence of density peaking on internal inductance in LHCD L-mode discharges. (Original figure using L-mode data set presented in Refs. 60 and 72.)
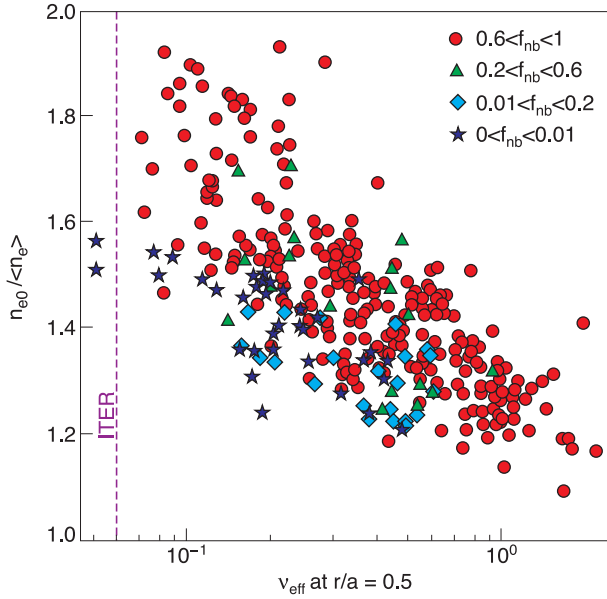
Fig. 27. Density peaking versus effective collisionality ν_{eff}. Symbols represent the fraction of NBI heating. ICRH H-modes are shown as blue stars. From Ref. 62. (Color online)

shear at $r/a = 0.5$ is found in a subset of data in which EFIT reconstructions constrained by polarimetry are available, despite the presence of conventional H-modes with finite shear and hybrid H-modes with very small core shear. The lack of a correlation with local or global measures of shear (except possibly at the lowest collisionalities[70]) and the presence of a strong correlation with collisionality are in stark contrast with L-mode behavior. The best-fitting H-mode scaling relations are

$$n_{e0}/\langle n_e \rangle = 1.15(\pm 0.07) - 0.12(\pm 0.02)\ln \nu_{eff}$$

$$+ 0.17(\pm 0.13)\Gamma^* + 0.13(\pm 0.08)T_i/T_e \ .$$

$$(11)$$

In the above expression ν_{eff} is taken as $2 \times 10^{-14} \langle n_e \rangle R_0/\langle T_e \rangle^2$, where the angle brackets denote volume averages, while T_i/T_e and Γ^* are taken at midradius. An extrapolation to ITER, using this fit and assuming $T_i/T_e = 0.9$,

provides $n_{e0}/\langle n_e \rangle \approx 1.47$ (Ref. 77), a result that is consistent with regressions based on a combination of JET and AUG data.[78] A local fit to the normalized density gradients around midradius provides

$$R/L_{n_e} = 0.97(\pm 0.34) - 0.65(\pm 0.1)\ln \nu_{eff}$$

$$+ 1.46(\pm 0.63)\Gamma^* + 0.65(\pm 0.4)T_i/T_e \ . \quad (12)$$

This scaling relation leads to an expectation of $R/L_{n_e} \approx 2.6$ near midradius in ITER. The coefficient (1.46 ± 0.63) of the local fit for Γ^* is an estimate for χ/D and is consistent with a theoretical expectation $(\chi/D = 1.5)$ for anomalous transport[69] and with the range of χ/D_T observed in trace tritium experiments[79] (also see Ref. 80 in this issue). Since χ/D_T may itself depend on plasma parameters, it should be viewed only as an average over the data set. The ratio χ/D so obtained, however, is significantly lower than was assumed in early investigations of density profiles on JET, indicating that the contribution of particle sources to density peaking was overestimated.

A density profile with a peaking factor of 1.47 would provide a boost of fusion power of more than 30% for fixed β and N_G with respect to the usual assumption of a flat density profile (Fig. 28), assuming that the temperature profile is as provided by the modeled reference scenario,[54,55] i.e., that $T_i(0) = 18$ keV and $T_i(0.95a) \cong 0.17 T_i(0)$, and that there is no change in He and impurity concentration. This relative benefit would be increased or reduced for a respectively lower or larger relative pedestal temperature.[77] On the downside, we also have to consider that for fixed N_G and β, density peaking unavoidably leads to a reduction of the pedestal density below the average density, by nearly 30% for the above ITER projections. This may affect divertor performance by making detachment more difficult. However, if the density limit is linked to the pedestal density, rather than the line average density, a simple remedy may be to raise the edge density to the target value with a corresponding temperature reduction to conserve β. Then, the effect of peaking is still beneficial, although somewhat less than at fixed average density. Density peaking may provide a natural means to recover core fusion performance (but not divertor performance) if the edge density limit drops to half of the

TABLE I

Range of Parameters in H-Mode Data Set

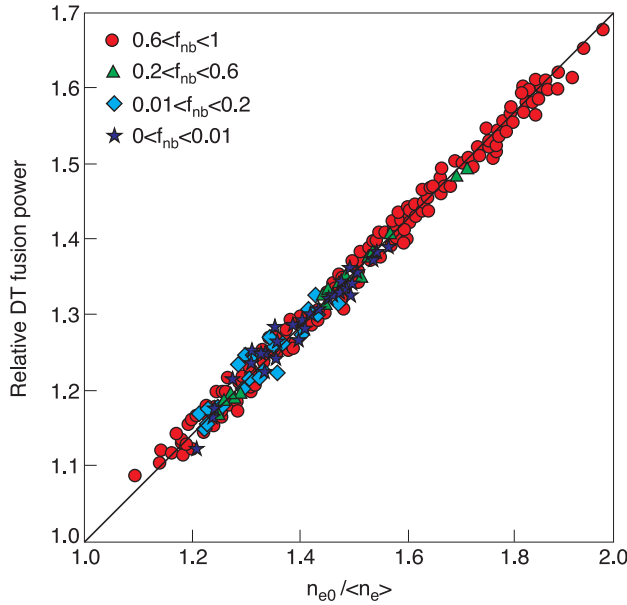|	I_p (MA)	B_T (T)	n_{e19}	P_{NBI} (MW)	P_{IC} (MW)	P_{LH} (MW)	ν_{*ei}	ν_{eff}	ρ^*	β_T (%)	β_N	T_i/T_e	q_{95}	l_i	N_G
Minimum	0.9	0.8	1.7	0	0	0	0.01	0.05	0.002	0.44	0.5	1.8	2.25	0.68	0.2
Maximum	3.7	3.7	10	18	11	3	0.4	2	0.01	3.9	3.3	0.5	6.4	1.1	1

Fig. 28. Relative fusion power increase as a function of density peaking assuming a fixed ion temperature profile as in Ref. 55, together with the whole range of density profiles observed in JET H-modes. From Ref. 77.

expected value as expected from Ref. 81. At constant β, fusion power with peaking expected for ITER would still exceed the flat reference case by nearly as much as when N_G is constant.[62]

At the time of writing, no specific studies of density profiles in ITB plasmas have been undertaken. Experiments have shown that ITBs are resilient to peripheral pellet fueling but are destroyed if the pellet penetrates to the barrier region.[71] The evolution of plasma profiles (including density profiles) in real-time-controlled (RTC) advanced scenarios have been successfully modeled using the JETTO code.[82]

III.C. Impurity Transport

III.C.1. Summary of Early Work on Impurity Transport

The direct impact of impurities on plasma dilution in conjunction with the expected advantage for a reactor of a radiating mantle at the edge have strongly motivated the study of the impurity behavior at JET.

Transport of impurities is inferred by comparing the radiation emitted by the impurities in the form of spontaneous radiation (spectral lines and continuum radiation, typically in the X-ray domain) and of actively excited spectral lines via CXRS with the predictions of transport models.[83,84] A linear relationship between impurity flux and impurity density gradient is generally assumed: $\Gamma_Z(r) = -D(r)\partial n_Z(r)/\partial r + v(r)n_Z(r)$, where v and D are the convection velocity and diffusion coefficients of the impurities of charge Z, respectively. Although these transport coefficients may be taken from theory, the analytical procedure consists in general of finding the spatial profiles of D and v that best reproduce the observations. The equilibrium gradient of the impurities is defined by the ratio $v(r)/D(r) = 1/n_Z(r)\partial n_Z(r)/\partial r$. With the source of the impurities being at the edge for all impurities except He ashes, the observation of a peaked impurity profile implies the existence of inward convection ($v < 0$).

A general finding well documented since the early works of the JET Joint Undertaking is that both in low-(L-) and high- (H-) confinement modes, impurity transport is generally anomalous, i.e., faster than predicted by neoclassical theory, especially in the outer region of the plasma. In neoclassical theory, impurity transport results solely from collisions and drift orbits in the tokamak field geometry, and the effects of collective modes, i.e., microinstabilities, are neglected. In a simplified approach $v_{neo}(r)/D_{neo}(r) = Z[1/n_D \; \partial n_D(r)/\partial r - H1/T_D \; \partial T_D(r)/\partial r]$, where H depends on collisionality and is around $\frac{1}{3}$ and n_D and T_D are the density and temperature of the main particles.[85] The neoclassical forces exerted on impurities by temperature and density gradients of the main particles are opposite, with the former term acting as a screen against impurities, and the resulting gradient is proportional to the impurity charge. As a result, peaked electron density profiles are of concern for impurity accumulation, especially in the presence of high-Z elements.

Transients events, such as those generated by injecting extrinsic impurities by means of gas puffing or laser blowoff (LBO), have been used over the years to discriminate between convection and diffusion terms and to characterize the transport regimes in the various experimental scenarios. Work at JET has also incentivized a continuous progress in the knowledge of atomic physics data required for impurity analysis, progress that has been mostly condensed in the ADAS database.[86] Important progress also has been made in the theoretical understanding of the anomalous transport, opening the way toward more reliable extrapolations to reactor regimes and toward concepts for impurity control.

Early experiments[83] using trace amounts of medium- and high-Z impurities injected into ohmic and ICRH-heated discharges provided measurements of the spatial dependence of the transport coefficients, revealing that impurity transport coefficients are close to neoclassical in the central region (typically inside the sawtooth inversion radius) and are clearly anomalous outside it. Such a radial dependence of the impurity transport of L-mode plasmas is a very general feature and pertains also to H-mode plasmas.[87] Transport is greatly enhanced during sawtooth crashes, effectively expelling impurities that may have accumulated in the center between successive crashes. Transport is also increased by additional ICRH power. H-mode plasmas were found to feature an impurity transport barrier at the edge,[88] corresponding to a sharp increase of the ratio v/D in a narrow region near the

plasma edge. In the attempt to find a physical explanation for the radial shape of the diffusion parameter, it was shown that in L-mode plasmas the extent of the low-transport core region varies with the magnetic field and with the total plasma current and is broadly correlated with the edge value of the safety factor as well as with the width of the central region with low magnetic shear.[89] More specifically, the diffusion parameter undergoes a rapid transition from near-neoclassical to highly anomalous levels in the vicinity of the radial position where the dimensionless shear parameter $1/r \, dq/dr \approx 0.5$. These findings are compatible with the picture of impurity transport carried by ITG/TEM instabilities. In fact, the marked increase of D in the outer region of the discharge occurs when the power per particle is raised or, alternatively, when the temperature and its gradient grow in that region. In Ref. 89, theoretical attempts to analyze the radial structure of the microturbulent fluctuations associated with ITG modes yielded a strong positive dependence of anomalous diffusion on the magnetic shear, as observed in the experiments.

The confinement time of nonrecycling injected impurities was measured in a wide range of L-mode discharges and, remarkably, was found to be lower than the energy confinement time.[90] Such a behavior would be favorable in a reactor, since it would ensure evacuation of impurities and in particular of the He ashes from the fusion reactions in a time shorter than the energy confinement time. However, in ELMy H-modes evidence of impurity accumulation is common in association with peaked electron density profiles.[91]

A finding that makes the general picture of the impurity behavior even more complex is the existence of poloidally nonsymmetric distributions of the impurity profiles in various conditions.[92] In optimized shear tokamak plasmas with fast toroidal plasma rotation, nickel ions have been observed to accumulate on the outboard side of the poloidal cross section.[93] In an rf-heated optimized shear plasma, nickel ions have instead been seen to accumulate on the inboard side.[94]

The most recent work on impurity transport at JET has characterized the impurity behavior in the advanced scenarios, corresponding to the most promising regimes in a reactor perspective, such as discharges with internal transport barriers, hybrid regimes and impurity seeded discharges. Specific studies have addressed the effect of electrostatic microinstabilities present in the plasma, with specific regard to their relationship with the impurity pinch as well as to the possibility to actively control the impurity density profile.

III.C.2. Impurity Behavior in Transport Barriers

In the presence of transport barriers in the plasma core, the impurity content in the plasma center is sensitive to the strength of the barrier. In the case of a "strong" transport barrier, the impurity diffusion coefficient in the

center can be an order of magnitude lower than that in plasmas with "weak" transport barriers. An inward convection of the impurities in the vicinity of the transport barrier is required to account for the measurements.[95] Similar results pertain also to experiments in which argon radiation has been used to control the edge and prolong the duration of optimized shear discharges with ITBs (Ref. 96).

This fact results in weak barriers that are less prone to disruptions. Argon accumulates in the core region due to a strong inward convection in the ITB region, combined with a weak inward convection in the core.

Further experiments[97] showed that in reversed shear ITB discharges, neon and nickel impurities accumulate when there is excessive peaking of the main ion density profile, in agreement with neoclassical convection. Also, the strength of the impurity peaking increases with the impurity charge and is low for the relatively low-Z elements C and Ne. The origin of the accumulation is associated with an inward drift inside the ITB radius. Figure 29 shows an example of Ni and Ne behavior in a strong ITB.
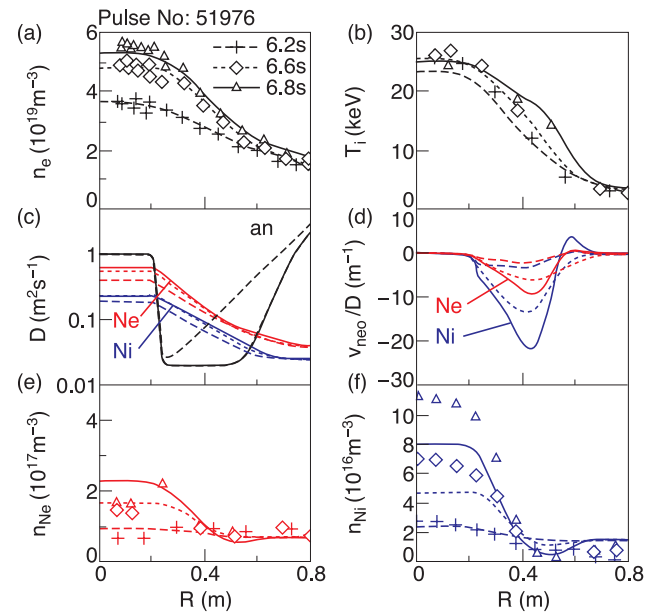
Fig. 29. Radial profiles of (a) electron density, (b) ion temperature, (c) calculated D, (d) v_{neo}/D of Ni and Ne, and (e) Ne and (f) Ni densities at three times in a JET discharge with a strong ITB. Convection is assumed to be neoclassical. In (f) the symbols show the experimental profiles and the lines are the results of the transport simulation. In (c) the diffusion is the sum of a neoclassical D_{neo} and an anomalous D_{an} term. In the barrier transport is neoclassical and the peaking factor v_{neo}/D is large and inward. Ni density increases more than the density of electrons and Ne. Discharge 51976 featured $I_p = 2.5$ MA, $B_T = 2.5$ T, $\langle n_e \rangle \approx 2.0 \times 10^{19}$ m^{-3}, $T_{e0} \approx 8$ keV, $P_{NBI} = 17$ MW, and $P_{ICRH} = 4$ MW. From Ref. 97.

Transport is more convective for Ni (Fig. 29d), and the peaking of Ni is more pronounced than that of Ne (Figs. 29e and 29f). The simulation of the impurity density profile evolution, which assumes a dominant neoclassical transport, is qualitative only for Ni (Fig. 29f) and underestimates the experimental peaking by 30%. The discrepancy reflects the uncertainties in the choice of D_{an} and in the measured profiles, which are critical for the neoclassical transport description.[97]

In weak positive shear ITBs instead Ne does not accumulate and its convection is outward.[98] In some cases, magnetohydrodynamic (MHD) events in the core flatten the radial profile of the metallic impurity. Accumulation of Ni and weak peaking of C are found in monotonic shear discharges with a strong ITB.

III.C.3. Impurity Transport in Standard H-Modes and Hybrid Scenarios

In H-modes the strength of the main gas puff was found to control the extent to which noble gas impurities penetrate and redistribute inside the main plasma, opening perspectives for impurity control in a reactor.[99] The latter are contained near the separatrix in discharges with a relatively strong level of main gas puffing, whereas reducing the main gas puffing below a certain level leads instead to impurity accumulation in the core, presumably due to the change of the sign of the neoclassical convective velocity for impurities from positive to negative within the edge transport barrier (ETB). A systematic study in a wide variety of standard H-modes and hybrid scenarios has shown that intrinsic carbon impurity profiles remain flat or slightly hollow inside $r/a < 0.7$, irrespective of the peaking of the electron (and hence main ion) profiles.[60]

In JET, investigations of the impurity transport in hybrid scenarios have been carried out by puffing mixtures of Ne and Ar (Ref. 100). No signs of significant accumulation were found, although Ar features an inward pinch at midradius. Figure 30 shows an example of the results of transport analysis of Ar and Ne based on absolute value data from CXRS, soft X rays, and emission spectral lines. Diffusion and convection of Ar and Ne are anomalous, although convection can be close to the neoclassical values at the edge. An intermittent, slow sawtooth mode present in all hybrid scenarios examined appears to be responsible for the confinement reduction of the impurities near $r/a \sim 0.3$. A scan of the plasma triangularity and of ρ^* (the Larmor radius normalized to the temperature logarithmic gradient) has shown a change from outward to inward convection at the edge when increasing triangularity for both low and high ρ^*, without leading to impurity accumulation, however.

With impurities in ITER ranging from He to W, investigating the charge dependence on impurity has been a priority in the JET experimental program. By injecting gases into the same discharges using the gas puff system and Ni using LBO (Refs. 100 and 101), it has been pos-
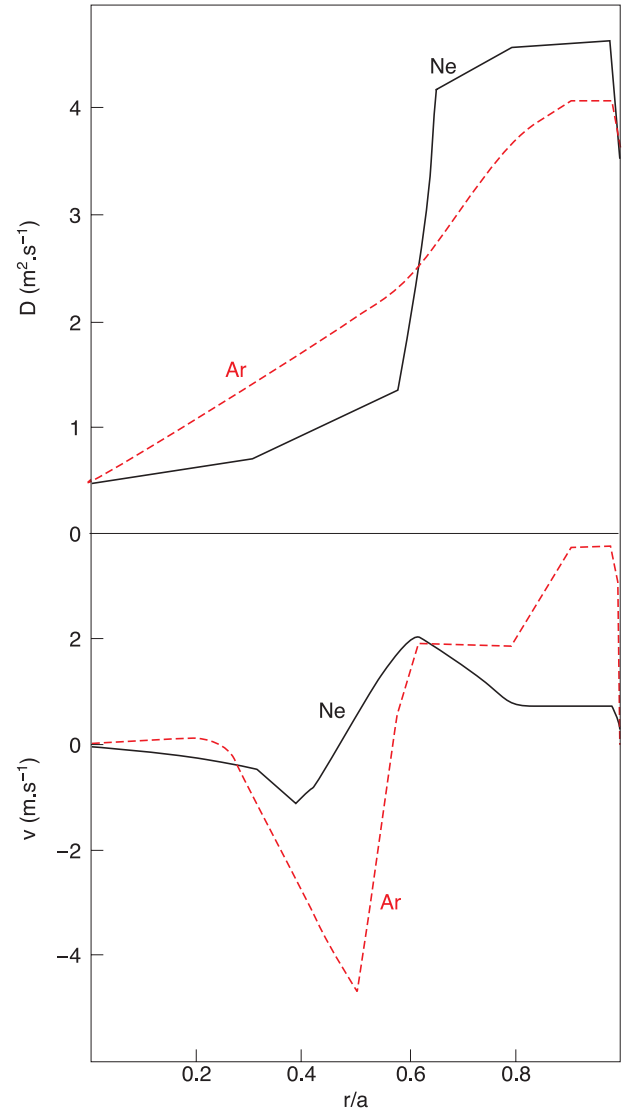
Fig. 30. D and v for Ne and Ar in JET pulse 60932 ($I_p = 2$ MA, $B_T = 2.4$ T, $\langle n_e \rangle \approx 3.1 \times 10^{19}$ m^{-3}, $T_{e0} \approx 7$ keV, and $P_{NBI} = 15$ MW) in the hybrid scenario. From Ref. 100.

sible to evaluate the Z dependence of impurity transport in various plasma conditions. Figure 31 shows the impurity peaking factor $-Rv/D$ at $r/a = 0.55$ in an ELMy H-mode discharge (JET pulse 66134, $I_p = 1.5$ MA, $B_T = 3$ T, $\langle n_e \rangle \approx 3 \times 10^{19}$ m^{-3}, $T_{e0} \approx 4.5$ keV, $P_{NBI} = 8$ MW, and $P_{ICRH} = 2$ MW) for C, Ne, Ar, and Ni (closed circles). The latter three have peaked profiles whereas for intrinsic carbon $\nabla n_c/n_c$ is positive at midradius, corresponding to slightly hollow carbon profiles. In the core, inside $r/a \sim 0.2$, the measured gradients have a strong dependence on the impurity charge.[101] Figure 31 also shows the anomalous transport component after subtraction of the neoclassical coefficients (open circles), compared at midradius with the results from
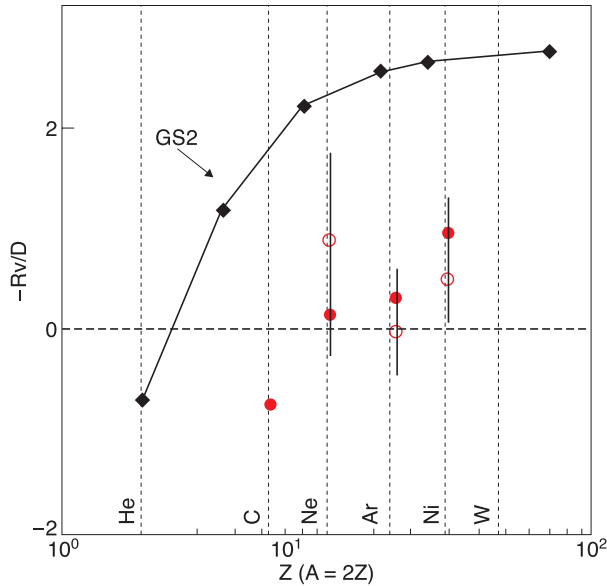
Fig. 31. Impurity peaking factor at $r/a = 0.55$ for four impurities from experiment (closed circles), after subtraction of the neoclassical transport coefficients (open circles) and linear gyrokinetic calculations (diamonds). From Ref. 101.

Fig. 32. D and v values for three JET Ar-seeded discharges: 52136 ($I_p = 2.5$ MA, $B_T = 2.5$ T, $\langle n_e \rangle \approx 7.5 \times 10^{19}$ m^{-3}, and $T_{e0} \approx 3.5$ keV) with NBI only ($P_{NBI} = 12$ MW); 53015 ($I_p = 2.5$ MA, $B_T = 2.5$ T, $\langle n_e \rangle \approx 6.5 \times 10^{19}$ m^{-3}, $T_{e0} \approx 3.5$ keV, $P_{NBI} = 12$ MW, and $P_{ICRH} = 2$ MW); and 53548 ($I_p = 2.5$ MA, $B_T = 2.5$ T, $\langle n_e \rangle \approx 9 \times 10^{19}$ m^{-3}, $T_{e0} \approx 3$ keV, $P_{NBI} = 14$ MW, and $P_{ICRH} = 2$ MW) (high triangularity) with additional 2 MW of ICHR deposited in the center. Note the dramatic change in the convection[107] in the discharges with additional ICRH.

quasi-linear gyrokinetic calculation [GS2 (Ref. 38), diamonds].[101,102] The values of $-Rv/D$ obtained only from neoclassical theory are in the range 18 to 65 (not shown), far above the experimental ones. They rise with Z. The turbulence-driven impurity peaking factors, inferred after subtraction of the neoclassical part (open circles), are of the same sign as the predictions but significantly smaller than predicted by GS2. Also, helium is calculated to have an outward pinch, i.e., $-v/D < 0$, as a result of outward thermodiffusion, as shown in Fig. 31. An experimental confirmation that $v/D > 0$ for He is still outstanding at the time of writing. It would offer a considerable operational advantage for a reactor in terms of He pumping requirements.

III.C.4. Effect of ICRH on Impurity Transport

Ar seeding has been used on JET to contrast the degradation of confinement with increasing densities typical of ELMy H-mode plasmas and to explore the feasibility of a radiative boundary.[103–105] In high-collisionality ($\nu_{eff} = 1$), high-triangularity H-mode discharges, it has been found that approximately 2 MW of centrally deposited ICRH power in addition to about 12 MW of NBI heating flatten the electron density profile and reduce the inward pinch convection of Ar typical of pure NBI–heated H-mode plasmas (see Fig. 32) (Refs. 106 and 107).

In other papers[66,108] the expelling capability of centrally deposited ICRH has been associated with the inherent control of the central q profile.

The effect of ICRH has been investigated in some detail through the analysis of the behavior of nickel injected via LBO in L-mode and H-mode JET discharges at ITER-relevant collisionality[109] ($\nu_{eff} = 0.1$). In discharges with $B_T = 3.25$ T, $I_p = 1.6$ to 1.8 MA, and 12 to 14 MW of NBI power, ICRH heating applied in mode conversion to heat the electrons or in minority heating to heat the ions systematically produced opposite effects on nickel transport, yielding flat or slightly hollow nickel density profiles in the case of mode conversion and peaked nickel density profiles in the case of minority heating. In the minority heating discharges, the diffusion coefficient in the plasma center is low, close to the neoclassical value, and the pinch velocity is inward throughout the radius. By contrast, with mode conversion heating, the central Ni diffusivity is higher than that of the neoclassical and the pinch velocity is slightly outward or nearly zero as shown in Fig. 33.

The curvature pinch and thermodiffusion already introduced in Sec. III.B (with T_e replaced by T_z in the thermodiffusion term) also affect impurities, with the important difference that thermodiffusive impurity pinches are opposite in sign to those affecting electrons,
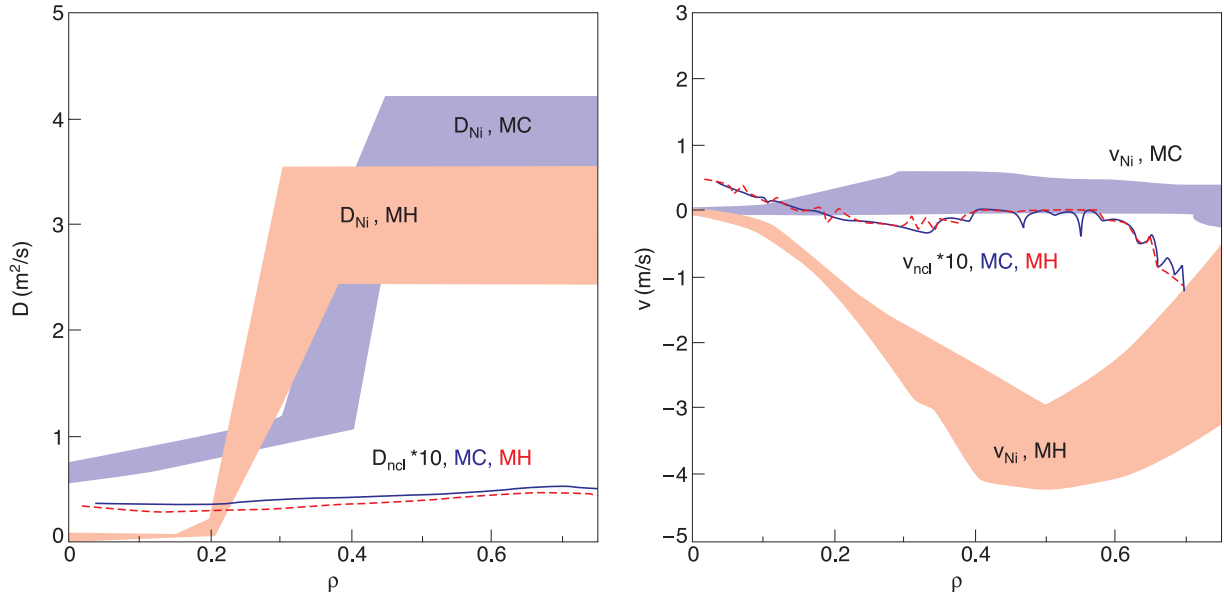
Fig. 33. Comparison of nickel transport coefficients in JET discharges with additional rf heating in mode conversion (MC-blue, 58149, $I_p = 1.8$ MA, $B_T = 3.3$ T, $\langle n_e \rangle \approx 2 \times 10^{19}$ m^{-3}, $T_{e0} \approx 6.5$ keV, $P_{NBI} = 15$ MW, and $P_{ICRH} = 5$ MW), featuring small or outward convection, and minority heating (MH-pink, 58144, $I_p = 1.8$ MA, $B_T = 3.3$ T, $\langle n_e \rangle \approx 2 \times 10^{19}$ m^{-3}, $T_{e0} \approx 6.5$ keV, $P_{NBI} = 15$ MW, and $P_{ICRH} = 5$ MW) with inward convection. Shading indicates the regions of the parameters space yield equally acceptable reconstructions of the experimental data. The neoclassical transport parameters are also shown. From Ref. 109. (Color online)

and they decrease with Z. A recently identified third effect is connected with the parallel compression of parallel velocity fluctuations produced along the field lines by the fluctuating electrostatic potential. This mechanism drives a pinch proportional to charge and inversely proportional to the ion mass, with a sign opposite to that of ion thermodiffusion.[110] The parametric dependence of impurity transport has been studied in Refs. 100, 109, and 110 with linear gyrokinetic calculations by means of the GS2 code.[38] In particular, it has been shown that when there is TEM turbulence, as occurs in the presence of dominant electron heating, the term driven by fluctuation of the parallel velocities can produce an outward pinch large enough to overcome the opposite thermodiffusion. A combination of all three mechanisms is proposed as an explanation for the differences of behavior in Fig. 33 (Ref. 109), balancing each other in the case of mode conversion.

III.D. Conclusions

One of the important contributions of JET in the area of particle transport is the accumulation of evidence for particle pinches, leading to the expectation of moderately peaked density profiles and significantly increased fusion power in ITER (compared to a flat profile) for a given average density and stored energy. Peaked density profiles, however, raise the issue of accumulation of impurities in the core, where particle and impurity transport are often close to neoclassical. In these conditions peaking of medium- and high-Z impurity profiles is observed when the electron density profile is peaked, such as in ordinary H-mode discharges and in discharges with internal transport barriers. Documentation of transport dependence on Z up to Ni and Mo shows that extrapolation to elements as heavy as tungsten is unfavorable unless turbulent transport dominates. Enhanced core transport by central ICRH has become a regular tool for preventing Ar accumulation in Ar-seeded plasmas at high collisionality. Ni accumulation is also prevented in JET H-modes at low triangularity plasmas at ITER-relevant collisionality using ICRH applied mainly to electrons. This is a very promising observation since the ITER heating systems as well as fusion alpha particles will mainly heat the electrons.

Future work at JET is aimed at a better understanding of the complex mechanisms of turbulent driven particle and impurity transport by means of detailed comparisons between theory and experiments. Special regard will be given to the role of the heating channels and collisionality in order to provide more reliable means to predict and control the impurity behavior in reactor plasma.

IV. CORE MOMENTUM TRANSPORT STUDIES IN JET

IV.A. Introduction

Of all the transport channels relevant to a tokamak, the transport of momentum is the least well studied or understood. The plasma rotation is of interest, however, since a sheared rotation can lead to the quenching of turbulence[111] and, hence, an improvement in confinement. Such an improvement can be both moderate as well as dramatic through the formation of a transport barrier. For the latter phenomenon experiments indicate that the toroidal and in particular the poloidal velocity play important roles in the dynamics of ITBs. In addition, toroidal rotation gives stability against beta-limiting resistive wall modes by making the stationary wall more conducting.[112,113] For these reasons the study of momentum transport is currently an active area of research, both theoretically as well as experimentally.

The radial force balance equation for E_r and the $E \times B$ flow shear $\omega_{E \times B}$ (Ref. 34) are written as follows:

$$E_r = \frac{1}{eZ_i n_i} \frac{\partial p_i}{\partial r} - v_{\theta,i} B_T + v_{\phi,i} B_p$$

and

$$\omega_{E \times B} = \frac{r}{q} \frac{\partial (q v_E / r)}{\partial r} \quad , \tag{13}$$

where

Z_i = charge number

n_i = density

p_i = pressure

$v_{\theta,i}$ = poloidal velocity of the ion species i

$v_{\phi,i}$ = toroidal velocity of the ion species i

v_E = $E \times B$ velocity

q = safety factor

B_T = toroidal component of the magnetic field

B_p = poloidal component of the magnetic field.

From these it becomes clear that both toroidal and in particular poloidal velocities play a crucial role in affecting the triggering mechanisms of the transport barriers through $E \times B$ flow shear.

This section reports on experimental and modeling studies of both toroidal and poloidal momentum transport on JET. The section is organized as follows: All the analyses of toroidal rotation and toroidal momentum transport are discussed in Secs. IV.B, IV.C, and IV.D, and those of poloidal velocities in Secs. IV.E and IV.F. Section IV.B is devoted to studies of the global toroidal momentum and energy confinement times. The local trans-port analysis of momentum and ion heat diffusivities is carried out in Sec. IV.C. Predictive transport simulations with self-consistent treatment of toroidal momentum transport are presented in Sec. IV.D. In Sec. IV.E the experimental results on the measurement of the carbon poloidal velocities in plasmas with strong ITBs are shown and are compared with neoclassical velocities. The consequences of the measured anomalous poloidal velocity profiles applied in transport simulations are demonstrated in Sec. IV.F. Finally, Sec. IV.G presents a summary of the results and conclusions. Not included in this section are the flows and momentum transport within the edge pedestal, L-H transition, and scrape-off layer (SOL).

IV.B. Global Toroidal Momentum and Energy Confinement Times

It has been reported in several large tokamaks that the toroidal momentum confinement time τ_ϕ is very similar to the energy confinement time τ_E (Refs. 114 and 115). This similarity, $\tau_E / \tau_\phi \sim 1$, has been observed on JET ELMy H-mode and L-mode plasmas, as illustrated in Fig. 34a, although some deviation in the hot-ion H-mode can be observed.[116] More recently, an analysis of a large rotation and momentum JET database consisting of hundreds of discharges (0.99 T $< B_T <$ 3.56 T, 0.98 MA $< I_p <$ 3.99 MA, 3.9×10^{19} m$^{-2} < \bar{n}_e < 28.2 \times 10^{19}$ m^{-2}, 1.85 MW $< P_{NBI} <$ 21 MW, and 0 MW $< P_{ICRH} <$ 7.45 MW) has confirmed the similarity between the energy and momentum confinement times, in particular in high- and medium-density plasmas.[117,118] This is illustrated in Fig. 34b. Here, τ_ϕ and τ_E are defined as the total momentum content divided by the torque and total energy content divided by the total heating power, respectively. There is no clear trend in the ratio of the momentum and energy confinement times in Fig. 34b among the different plasma operation scenarios. Still, within one scenario, there seems to be always a trend toward higher τ_E / τ_ϕ ratios at lower density.

IV.C. Analysis of Local Toroidal Momentum and Ion Heat Diffusivities

Based on the results from studies of global momentum and energy confinement, one could expect to have very similar momentum and ion heat diffusivities in tokamaks. However, although the global momentum and energy confinement times would be the same, the local diffusivities in the core plasma may well be different, in particular because the edge momentum pedestal is often weaker, although the knowledge of local momentum transport within the pedestal is rather limited. On the other hand, equal diffusivities $P_r = \chi_\phi / \chi_i = 1$ (based only on the diagonal terms in transport matrix, i.e., excluding any pinch terms) in the plasma core were predicted a long time ago in the early days of the ITG theory.[119] This assumption has been also commonly used in ITER predictions.
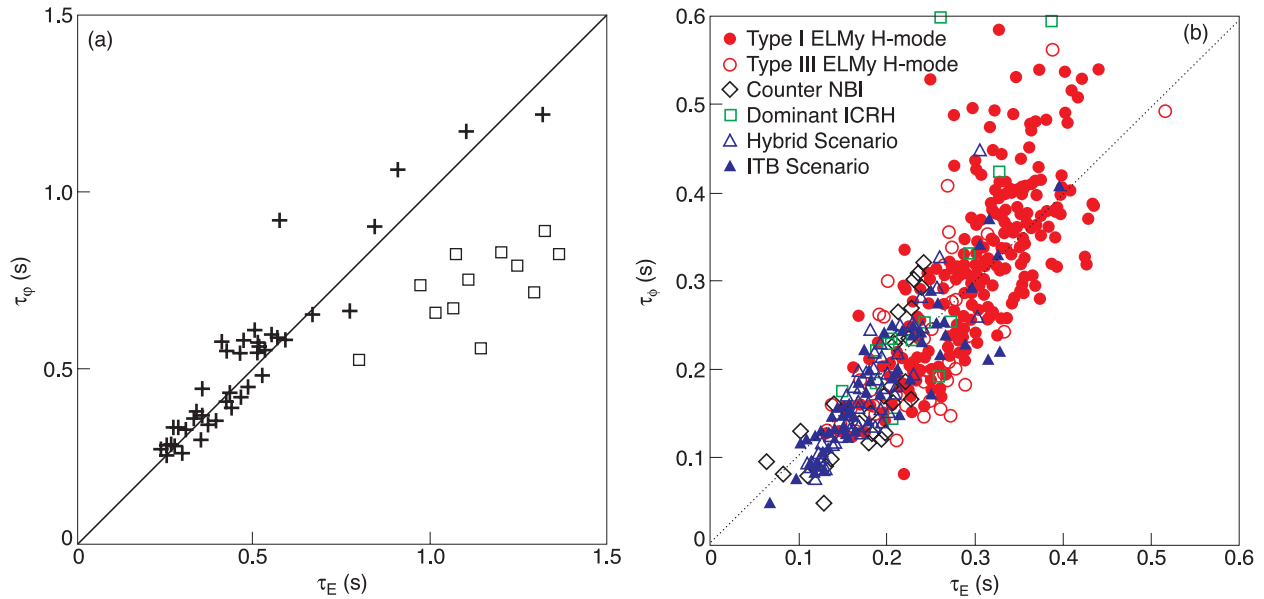
Fig. 34. (a) Momentum confinement time as a function of energy confinement time for L-mode and ELMy H-mode discharges (crosses) and for hot-ion H-mode shots (squares) (reproduced from Ref. 116). (b) The momentum confinement time as a function of the energy confinement time for several hundreds of shots covering several plasma operation scenarios (reproduced from Ref. 118).

Using the momentum database, it is possible to calculate the effective diffusivities and effective Prandtl number $P_{r,eff} = \chi_{\phi,eff}/\chi_{i,eff}$ from

$$\chi_{\phi,eff} = \frac{\Gamma_\phi}{\nabla mnR\omega_\phi} \qquad (14)$$

and

$$\chi_{i,eff} = \frac{q_i}{n\nabla T_i} \ , \qquad (15)$$

where

q_i = heat flux

Γ_ϕ = torque flux

ω_ϕ = angular frequency

T_i = ion temperature

n_i = ion density

m = mass

R = major radius.

Here, the torque flux Γ_ϕ includes only the NBI-driven torque, and therefore the torque sources from intrinsic rotation and ICRH are neglected. However, these sources in the NBI-heated JET plasmas turn out to be very small, as explained in detail shortly.

The relation of effective momentum diffusivity to the ion heat diffusivity is shown in Fig. 35 for a large number of discharges from the JET momentum database, covering pulses from several different plasma scenarios.

Fig. 35. Effective momentum diffusivity versus effective ion heat diffusivity for several hundred JET discharges from several plasma operating scenarios (reproduced from Ref. 120).

The values of the diffusivities are averaged over the gradient region at $\rho = 0.4$ to 0.7.

It is to note that $P_{r,\text{eff}}$ on JET is significantly smaller than 1, the average value being around $P_{r,\text{eff}} = 0.25$. This number is smaller than unity, commonly used in ITER predictions and often appearing in the ITG theory.[119] It is important to note here that the effective diffusivities calculated from the experimental data also include, besides the diffusive terms, all the possible pinch terms, whereas theoretical studies, such as the ones in Ref. 119, include only the diagonal, purely diffusive terms. Since the neoclassical ion heat diffusivity is small, typically a few percent of the total ion heat diffusivity, around midradius between $\rho = 0.4$ to 0.7, the ratio $\chi_\phi/(\chi_i - \chi_{i,\text{neo}})$ is within the measurement accuracy the same as the ratio χ_ϕ/χ_i, although from the physics point of view, the use of the ratio $\chi_\phi/(\chi_i - \chi_{i,\text{neo}})$ is more justified.

There are two important aspects not mentioned earlier that can affect both the trends in the global confinement times and the ratio of the effective momentum diff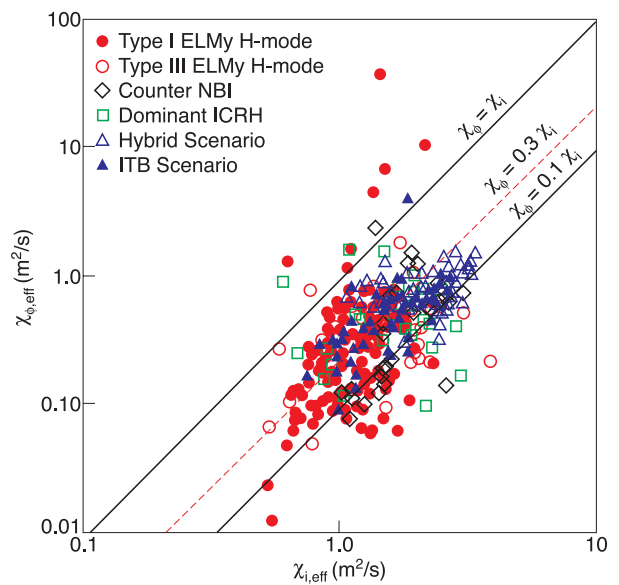usivity to the effective ion heat diffusivity: the role of momentum pinch and the spontaneous or intrinsic rotation. A momentum pinch velocity is indeed predicted by theory[121–123] (and more recently, Refs. 124, 125, and 126). With the pinch velocity included, the momentum flux can be divided between the contributions from the pinch velocity and diffusivity χ_ϕ rather than having only the momentum flux, yielding the effective diffusivity $\chi_{\phi,\text{eff}}$. Then, $P_{r,\text{eff}}$ can be significantly different from P_r. Dividing the momentum flux into the diffusive and pinch terms, one can write the effective diffusivity as

$$\chi_{\phi,\text{eff}} = \chi_\phi \left(1 + \frac{Rv_{pinch}}{\chi_\phi} \frac{1}{R/L_{v\phi}} \right) \, , \qquad (16)$$

where χ_ϕ is the actual momentum diffusivity, v_{pinch} is the momentum pinch velocity (negative value inward), and

$$L_{v\phi} = -\frac{1}{v_\phi} \frac{dv_\phi}{dr} \ \ .$$

The ratio Rv_{pinch}/χ_ϕ is defined as the pinch number. As can be seen in Eq. (16), $P_{r,\text{eff}}$ can be significantly different from the Prandtl number with diffusive terms only ($P_r = \chi_\phi/\chi_i$) if the momentum pinch velocity is large. However, steady-state analysis does not allow us to separate the relative weight of the diffusion and pinch terms in the momentum flux, and therefore transient momentum transport experiments are needed to study the momentum transport processes more deeply.

Very recent perturbative NBI modulation experiments on JET have indeed given indications of the presence of a significant inward momentum pinch, of the order of several meters per second.[120] This pinch term allows for P_r of around 1, consistent with theoretical predictions, together with a low effective Prandtl number, $P_{r,\text{eff}}$, consistent with the steady-state database value

$P_{r,\text{eff}} \sim 0.1$ to 0.3. The experimental results, i.e., the high P_r value and pinch, are in good qualitative and to some extent also in quantitative agreement with linear gyrokinetic simulations with the LINART code.[127]

The role of spontaneous rotation on many tokamaks has been reported in several papers.[128–131] The magnitude of intrinsic or ICRH-induced toroidal rotation was also reported recently in JET ohmic and in ICRH-heated plasmas.[132] That paper shows that the magnitude of intrinsic rotation in JET ohmic plasmas (LHCD only) is about 20 km/s in the plasma center, whereas in the database of about 20 discharges with ICRH, v_ϕ in the center varies from -10 to $+20$ km/s. These numbers should be compared with plasmas with NBI heating, in which the range of v_ϕ in the plasma center varies typically from 200 km/s (high-density ELMy H-mode) up to 600 km/s (strong ITBs). As a consequence, the intrinsic or spontaneous rotation with ohmic or ICRH-heated plasmas is only 3 to 10% of that in NBI-heated plasmas (spontaneous rotation is roughly within the measurement accuracy of the diagnostics), and thus it cannot affect the results and trends reported in Figs. 34 and 35, provided of course that the spontaneous rotation stays at the same level in NBI-heated discharges as in discharges without it.

IV.D. Simulations of Toroidal Momentum Transport

Toroidal momentum transport has been studied extensively with the JETTO transport code for high- and low-density ELMy H-mode discharges, hybrid scenario discharges, and L-mode discharges. A version of the Weiland model including self-consistent treatment of the toroidal velocity has been used.[133,134] A comparison of the toroidal velocity, ion and electron temperatures, and ion heat diffusion coefficients between the experiment and predictions with the new version of the Weiland model as well as with the GLF23 transport model[39,135] is illustrated for one typical high-density ELMy H-mode discharge in Fig. 36. The turbulent modes for this high-density, high-collisionality discharge are expected to be completely ITG dominant, and this is also confirmed with the linear gyrokinetic flux tube code KINEZERO (Ref. 31). The boundary conditions are tried to match at $\rho = 0.8$, although the simulation range expands up to the separatrix, since the models often have numerical problems close to the plasma edge. The agreement between the predictions with both models and the experimental profiles is very good and of the same accuracy as the predictions for the temperatures. This kind of good agreement of v_ϕ and T_i between the predictions and experiments is generally true for other transport simulations of high-density ELMy H-mode discharges existing in the JET momentum database, with the root-mean-square (rms) error in v_ϕ being on average 14% among the six simulated high-density shots with the Weiland model. The rms error for T_i is about 12% in the same simulations. A detailed analysis of the simulations with the errors can be
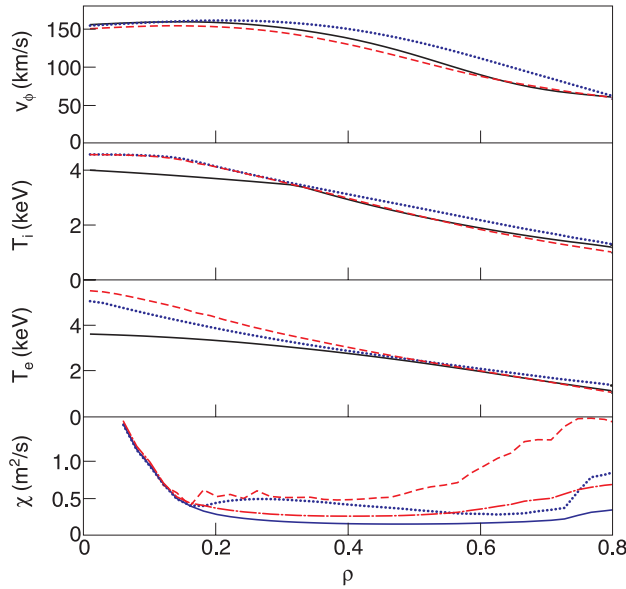
Fig. 36. Experimental values (solid curves) and values pre-
dicted by GLF23 (dotted curves) and Weiland model
(dashed curves) of v_ϕ (top frame), T_i (second frame),
and T_e (third frame) for pulse 57865 ($B_T = 2.7$ T, $I_p =$
2.5 MA, $n_{e0} = 10^{20}$ m^{-3}, and $P_{NBI} = 17$ MW). The
bottom frame shows χ_ϕ and χ_i predicted by the GLF23
(blue solid and dotted curves) and by the Weiland
model (red dashed-dotted and dashed curves) (repro-
duced from Ref. 136). (Color online)

found in Ref. 134. In addition, although in the simulation
shown in Fig. 36 the momentum pinch is excluded, the
simulations in Ref. 134 include it. Both models also pre-
dict that the ratio of χ_ϕ/χ_i is around 0.2 to 0.5 in the
gradient region, consistent with interpretive local trans-
port analysis of the diffusivities presented in Sec. IV.C.
This ratio is clearly smaller than 1, the value derived
from the early ITG without taking into account the full
toroidal geometry and trapped particles,[136] with the main
differences coming from the inclusion of toroidicity and
trapping. A general conclusion from the transport simu-
lations is that the models predict the rotation and tem-
peratures for high-density JET plasmas as well as or better
than those for the low-density ones.

IV.E. Experimental Results of Poloidal Velocities in ITB Plasmas on JET

In general, the poloidal velocity is assumed to be
neoclassical in tokamaks. However, recent JET results
indicate that this assumption is not correct in plasmas
with ITBs. Similar results with v_θ exceeding the standard
neoclassical estimate have been also found in TFTR
(Ref. 137) and DIII-D (Ref. 138). The experimental ion
temperature, density, and toroidal and poloidal velocities
are shown in Fig. 37 for a typical JET ITB discharge at

four instants. The poloidal velocities can reach values of
up to $v_\theta = -50$ km/s within the fully developed ITB,
whereas before ITB formation they stay around 5 to 10
km/s. A negative value of v_θ is defined to flow in the ion
diamagnetic drift direction. The comparison between car-
bon poloidal velocity v_θ and the neoclassical predictions
for the carbon ion velocity calculated with the neoclas-
sical transport code NCLASS (Ref. 139) is shown in
Fig. 38 (left frames) for two JET discharges. The mea-
sured carbon v_θ is an order of magnitude larger within the
ITB than its neoclassical estimate for both cases. Even
the sign of the measured carbon v_θ is different from the
neoclassical one in some radial regions, and furthermore,
it can change sign within the ITB. Similar results are
obtained for other JET ITB discharges.[140] Note that for
this discharge, the maximum ion temperature gradient
length is about twice the ion poloidal Larmor radius,
indicating that the neoclassical theory begins to be at the
verge of its validity, although it still satisfies the standard
validity condition. Another point worth mentioning here
is that because of the observed large poloidal rotation,
the possibility of a strong electric field should be in-
cluded in the orderings for the equilibrium, and hence
mainly an issue of self-consistency in the standard neo-
classical treatment. Therefore, when the applicability of
the standard neoclassical theory becomes marginal, as is
the case here, then it has to be kept in mind that the real
neoclassical transport and the level of neoclassical trans-
port predicted by the standard neoclassical theory might
differ significantly.

IV.F. Transport Modeling of ITB Plasmas Using the Experimental v_θ

As shown later in Sec. V, predicting the dynamics of
the ITBs has turned out to be one of the biggest chal-
lenges for transport models. In particular, the first-
principle transport models often fail to predict the onset
of the ITB or the correct radial location.[141] There are
probably several reasons for difficulties in reproducing
ITBs, but one of the reasons, not taken into account ear-
lier, is that past transport simulations have always as-
sumed that the poloidal rotation velocity is neoclassical.
As shown above, this is not a good assumption, and there-
fore the $E \times B$ flow shear used in the transport simula-
tions has not been appropriate.

To illustrate the changes in the modeling results due
to the different source of v_θ, two predictive simulations,
with both the Weiland transport model and GLF23, are
compared in Fig. 39 for JET ITB discharge 59193. The
only difference between the two simulations with both
models is that the first ones (blue dotted for the Weiland
model and green long-dashed for GLF23) use the neo-
classical poloidal velocity from NCLASS, whereas the
second ones (magenta short-dashed for the Weiland model
and yellow dashed-dotted for GLF23) employ the exper-
imentally measured v_θ in the calculation of E_r and $\omega_{E\times B}$
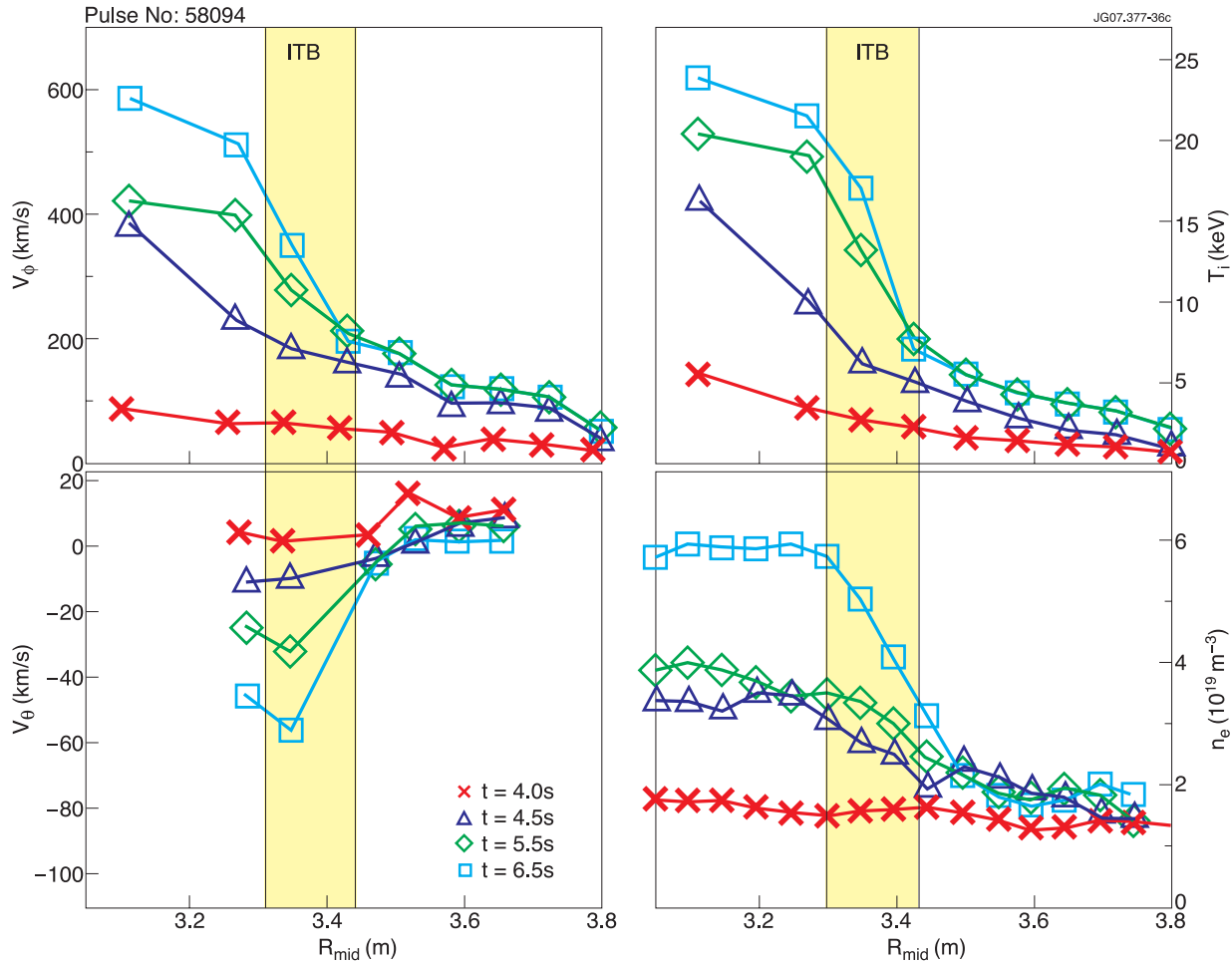
Fig. 37. Toroidal and poloidal rotation, ion temperature, and electron density profiles at four instants for a typical JET ITB discharge ($B_T = 3.45$ T, $I_p = 3$ MA, $n_{e0} = 4 \times 10^{19}$ m^{-3}, and $P_{NBI} = 21$ MW). The yellow shaded region indicates the location of the ITB (reproduced from Ref. 140). (Color online)

flow shearing rate (color online). In all the cases, the simulations are run from $t = 5.0$ s until $t = 6.8$ s, thus covering the phase without an ITB roughly before $t = 6$ s, toward the ITB formation phase, and until the ITB sustainment phase. All the initial conditions and boundary conditions on top of the H-mode pedestal are taken from the experimental data from pulse 59193 at $t = 5.0$ s. The q profile is rather flat in the core region (slightly reversed in the very center, well inward from the location of the ITB), and thus the negative magnetic shear does not act as the main mechanism to form the ITB for this pulse. Instead, the $q = 2$ surface is believed to play a significant role in triggering the ITB for this discharge, as for many other JET ITB pulses.[142,143]

The Weiland model and GLF23 correctly predict no ITB in the ion and electron temperature profiles in the phase before the ITB has formed with both options of poloidal velocity. When the experimental poloidal rotation is used, the Weiland model predicts the ion ITB at

just the right radial location and the right instant and with roughly the same ITB strength as measured in the experiments. The same is also true for GLF23. On the other hand, otherwise identical simulations, except with v_θ from NCLASS instead of the experimental one, does not exhibit any sign of an ITB in either case, and the agreement in T_i and T_e is much worse. Worth noting are the also large differences in E_r as a strong well appears at the location of the ITB with measured v_θ, instead of a gentle hill with neoclassical v_θ. Furthermore, the $\omega_{E \times B}$ shearing rates are locally larger by an order of magnitude, thanks to the deep E_r well with measured poloidal velocity, and exceed significantly the growth rates. This clearly demonstrates that one of biggest deficits in transport simulations of ITB plasmas has been the lack of knowledge of v_θ, further leading to the wrong estimate for the $\omega_{E \times B}$ shearing rates. However, using the measured poloidal velocities does not necessarily improve our predictive capabilities to model ITBs, although now when imposing
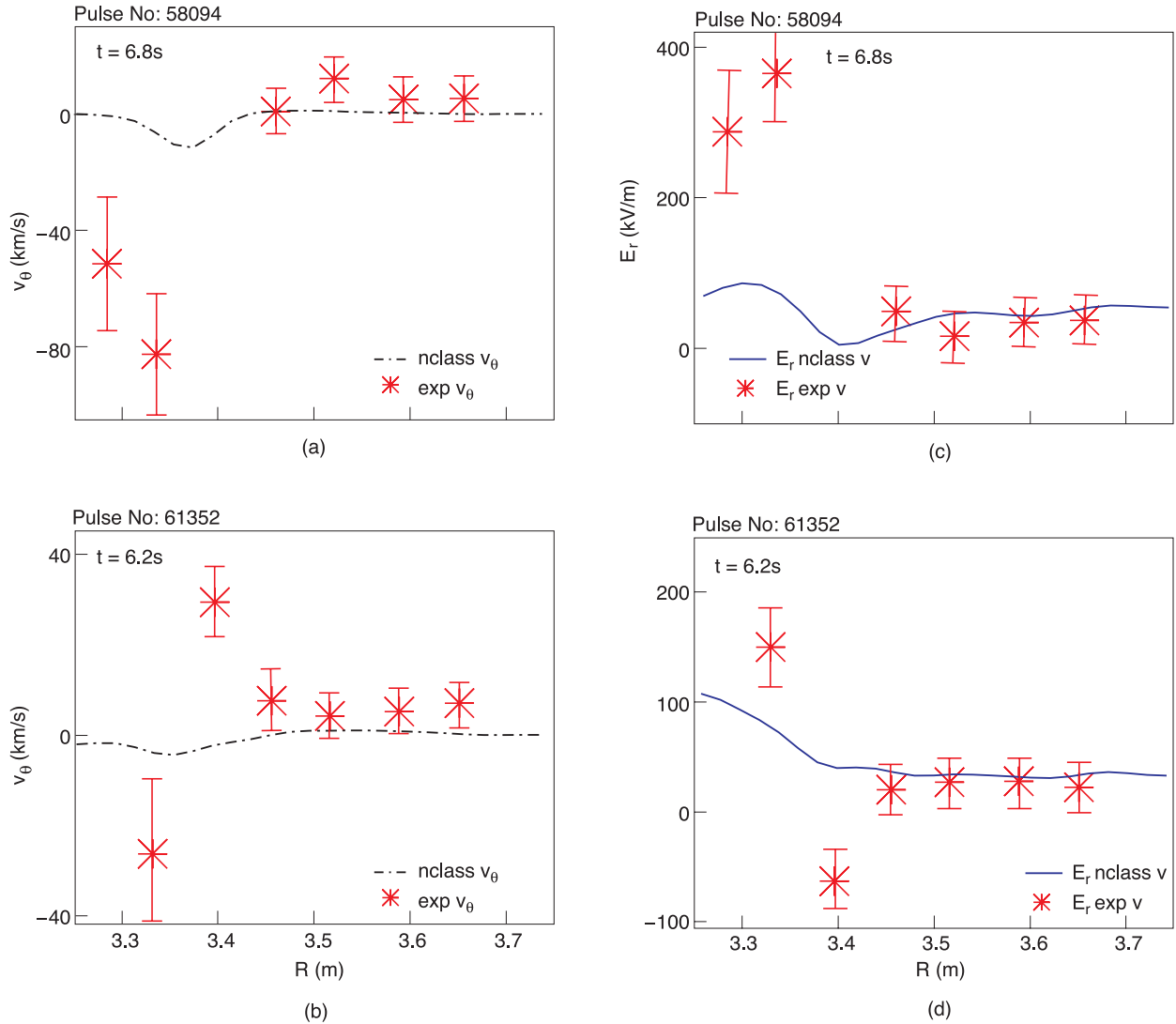
Fig. 38. Shots 58094 ($B_T = 3.45$ T, $I_p = 3$ MA, $n_{e0} = 4 \times 10^{19}$ m^{-3}, and $P_{NBI} = 21$ MW) and 61352 ($B_T = 3.2$ T, $I_p = 2.5$ MA, $n_{e0} = 4.5 \times 10^{19}$ m^{-3}, and $P_{NBI} = 18$ MW). (a) and (b) Comparison of measured carbon v_θ profiles with neoclassical predictions by NCLASS. (c) and (d) E_r profiles calculated using the force balance equation, with the measured (stars) and the NCLASS v_θ (line) results (reproduced from Ref. 140).

more experimental data, we can form ITBs. To genuinely improve our predictive capabilities, one should also be able to predict the increase in v_θ self-consistently, rather than using the experimentally measured data. An additional issue to be clarified in future is to understand the link between the integer or the rational surfaces of the q profile, which are known to play a role in ITB triggering, and the spin-up of v_θ and the onset of the ITB. Certainly there are some causality chains between these three events. However, the standard versions of the two models do not have any role from the integer values of q, and for them to become self-consistent and fully predictive, more development of the models is needed.

IV.G. Summary and Conclusions

The toroidal momentum database has confirmed the observation that $\tau_E / \tau_\phi \sim 1$ in all the different plasma scenarios employed on JET. Still, it is worth noting that the scatter among the different discharges is significant, ranging roughly from $\tau_E / \tau_\phi \approx 0.6$ up to $\tau_E / \tau_\phi \approx 1.5$. On the other hand, locally in the gradient region the effective Prandtl number is on average $\chi_{\phi,eff} / \chi_{i,eff} \approx 0.3$, determined from the local interpretive transport analysis. Again, there is a large scatter among the discharges, but certainly one can conclude easily that in the core plasma on JET tokamak, momentum is better confined than energy.

Fig. 39. Predictions for the ion temperature, radial electric field and $\omega_{E \times B}$ shearing rate for shot 59193 ($I_p = 1.5$ MA, $B_T = 3.1$ T, $P_{\text{NBI}} = 14$ MW, and $n_{e0} = 2.8 \times 10^{19}$ m^{-3}) before the ion ITB formation, at $t = 5.7$ s (left frame), and after it, at $t = 6.2$ s (right frame), using both the Weiland model and GLF23 with either measured or neoclassical poloidal velocity (reproduced from Ref. 136).
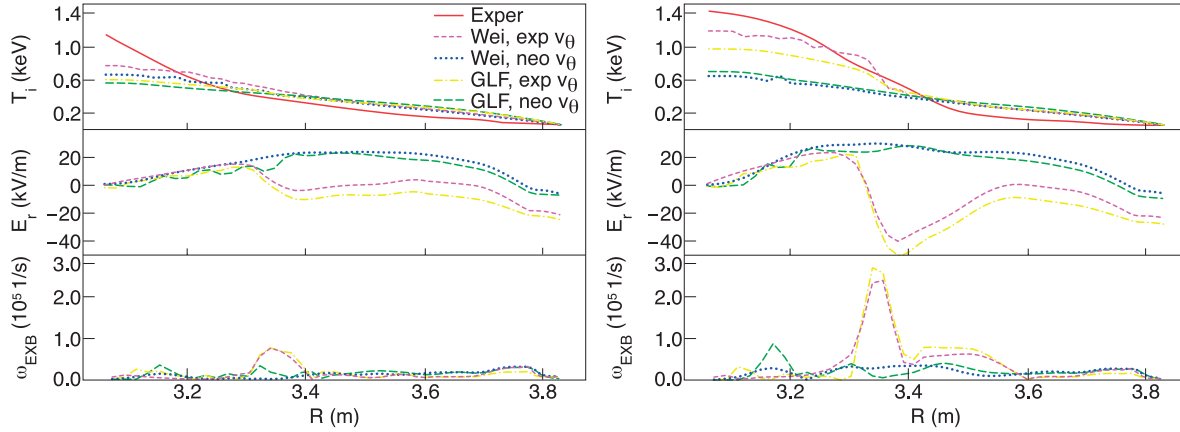
Furthermore, there is a discrepancy in the momentum and ion heat transport between the global and local transport; i.e., while $\tau_E / \tau_\phi \sim 1$, $\chi_{\phi,eff} / \chi_{i,eff} \approx 0.3$, and this can be understood by the fact that the momentum transport at the pedestal is larger than that of energy.[118]

A detailed momentum transport analysis from the perturbative torque modulation experiments on JET have shown that the Prandtl number based on diffusive terms only is close to $\chi_\phi / \chi_i \approx 1$. This value, combined with the significant inward pinch velocity found, results in a low effective Prandtl number $\chi_{\phi,eff} / \chi_{i,eff} \approx 0.3$, yielding the core momentum confinement being better than that of energy. These experimental results are in good qualitative and to some extent also in quantitative agreement with linear gyrokinetic simulations, which typically predict the ratio roughly $\chi_\phi / \chi_i = 0.7$ (Refs. 124 and 144).

The second point that may affect the fact that the effective Prandtl number is so low is the magnitude of the intrinsic toroidal rotation. However, the magnitude of intrinsic rotation in JET ohmic plasmas (LHCD only) is about 20 km/s in the plasma center, whereas in the database of about 20 discharges with ICRH, v_ϕ in the center varies from -10 to $+20$ km/s (Ref. 132). Therefore, the intrinsic or spontaneous rotation with ohmic or ICRH plasmas is only 3 to 10% of that in NBI-heated plasmas, and thus it cannot affect the global momentum confinement time or the momentum diffusivities and trends reported in this paper. To extrapolate the toroidal velocities in the ITER core plasma, a reassessment is needed since the standard assumption $\chi_\phi / \chi_i = 1$ is not justified from the JET results. The self-consistent transport simulations of toroidal momentum with the Weiland model and GLF23 predict v_ϕ roughly with the same accuracy as T_i, with the agreement being better for high-density plasmas.

Anomalous carbon poloidal velocities, exceeding the neoclassical estimate by a factor of 10, are measured within the ITB on JET (Ref. 140). This changes the calculated E_r and $\omega_{E \times B}$ shearing rates significantly and improves the success of first-principle transport models in predicting the dynamics of the ITBs. Both the Weiland model and GLF23 reproduce the onset, location, and strength of the ITB well when the experimental poloidal velocity is used, whereas they do not predict the formation of the ITB using the neoclassical poloidal velocity in time-dependent transport simulations. Consequently, the use of neoclassical poloidal velocity in the calculation of the $E \times B$ is one of the major reasons that the first-principle transport models have not been successful in reproducing the dynamics of the ITBs. It should be noted here, however, that neoclassical theory may not be fully valid under these kinds of plasma conditions, and therefore the neoclassical transport predicted using an equilibrium treatment that would take into account the modifications due to the large radial electric field could give significantly different results from that of the standard neoclassical theory. Major unresolved issues are the causality between anomalous v_θ, the onset of the ITB, and the appearance of the $q_{\min} =$ integer surface, as well as the sign of v_θ, since neither the experiments nor the simulations reveal any clear parametric dependence so far. More work is needed both on the experimental front and on the modeling side to solve the causality question and fully understand the reason for the spin-up of the v_θ within the ITB.

V. PHYSICS OF ITBs ON JET

V.A. Introduction

Since the early observation of "optimized shear" plasmas on JET (Ref. 145), a tremendous effort has been

undertaken to understand the physics of ITBs. The experimental progress in advanced tokamak scenarios in JET is reported separately in Chapter 4 of this issue[146] and also was reviewed earlier.[147] ITBs can be defined as regions of the core plasma in which turbulent transport is reduced or quenched. Triggering and sustainment of ITBs are complex issues and are known to depend on a large number of factors. However, it is widely admitted that two ingredients play an important role in the dynamics of ITBs: the local magnetic shear, which depends on the profile of the safety factor together with the Shafranov shift (defined as the difference between the centers of the last magnetic flux surface and the magnetic flux surface at a given ρ) and the $E \times B$ flow shear. Even if the analysis is restricted to these two elements, the overall situation remains difficult to understand in detail, and several issues need to be resolved.

The first issue deals with the relative role of magnetic shear and flow shear. If the flow shear is the main trigger mechanism, the transition is expected to be of first order; i.e., a jump of temperature gradient is expected above a critical thermal flux. This implies that the transition should occur above a power threshold, and also that some hysteresis is expected. If magnetic shear is the main ingredient, one may expect a second-order transition, i.e., no abrupt discontinuity of temperature gradient at threshold. In principle, neither power threshold nor hysteresis are expected in this case. Of course, reality is more complex since some power is needed to shape a current profile. Still, this classification is quite useful, and the understanding of the mechanisms that underlie the transition is certainly a central issue, which can be addressed by analyzing the JET database. This analysis confirms that the amount of $E \times B$ flow shear needed to trigger an ITB depends on the magnetic shear. However, an analysis of the database cannot remove the ambiguity on the nature of the transition. It turns out that heat modulation experiments provide a powerful tool to investigate this point.

A related open issue is the role of magnetic surfaces associated with low-order rational values of the minimum safety factor. Experiments at JET have clearly shown that these surfaces often play an important role when an ITB is being formed. This puzzling behavior raises a fundamental difficulty, since most theoretical models do not predict a special role of these surfaces. This question may be related to another surprising observation, namely, values of the poloidal flow well above the values predicted by neoclassical theory.

The third issue is related to the location and width of the barrier. Does the barrier appear at zero or negative magnetic shear? Does a barrier cover the whole central region, or does it exhibit a finite radial width? Again, the database provides some elements of response, but error bars do not allow a definitive answer. Turbulence measurements and heat modulations experiments have provided invaluable information, although somewhat contradictory at first sight.

The interpretation and preparation of future experiments, but also the extrapolation of the present performances to next-step devices such as ITER, require the development and validation of accurate modeling tools, ranging from 1-D transport predictive modeling to five-dimensional turbulence simulations. The JET profile database, which covers a large variety of steady and transient regimes, has been used extensively to test these models. Again, dedicated experiments have proved their usefulness since their analysis usually leads to a deeper exploration of the model capabilities.

In summary, this section aims to seek an answer to the following open issues, listed also in a recent review paper[148]:

1. Which are dominant mechanisms for ITB formation? Can the dominant term(s) be different with different plasma parameters, such as B_T, P_{in}, q, etc.? Can the dominant term be different for different transport channels? Does the onset of an ITB have a characteristic of a first- or second-order transition?

2. What is the role of the integer and rational surfaces of the q profile? Is it needed to trigger a barrier? Does the minimum value of q ($s = 0$) have a special role?

3. How is the turbulence reduced; is a full suppression needed or can partial suppression lead to an ITB? Does the suppression of turbulence extend radially from the footpoint of the ITB up to the center of the plasma, or is it limited to a narrow layer around the ITB?

4. Why do the theory-based transport models struggle so much in predicting the time dynamics of the ITBs?

This section is organized as follows: General considerations on ITB formation and sustainment are presented in Sec. V.B. Experiments dedicated to understanding the physics of ITBs are presented in Sec. V.C. Predictive modeling and turbulence simulations are reviewed in Secs. V.D and V.E. A conclusion follows in Sec. V.F.

V.B. General Considerations on Barrier Formation and Sustainment

V.B.1. Microstability and Criterion for Triggering ITBs

The explanation for the formation and sustainment of ITBs is usually based on a mixture of linear stabilization and turbulence quench due to flow shear stabilization (in its linear or nonlinear form). The local magnetic shear is often considered to be the main reason for improved stability. Two mechanisms have been identified for magnetic shear stabilization. First, the interchange drive decreases with magnetic shear. Interchange modes ultimately become stable at negative magnetic shear.[149] What counts is the local magnetic shear, which depends on the Shafranov shift of magnetic surfaces. A simple rule states that the local magnetic shear on the low-field

side is of the order of s-α, where $s = rdq/qdr$ (q is the safety factor) and $\alpha = -q^2 Rd\beta/dr$, hence the name α stabilization (plasma beta defined as $\beta = 2\mu_0 n_e(T_e + T_i)/B^2$). Second, a rarefaction of resonant surfaces occurs at zero magnetic shear and may lead to stabilization.[150] However, the latter mechanism is still subject to controversy, since it requires very low values of the toroidal wave numbers to be effective.[151] Other parameters may play a role, such as the impurity content, the ratio of the ion to electron temperature, or the density gradient. The impurity content has a diluting effect (fast particles also have a similar effect) that influences the effective pressure gradient in the interchange drive, whereas increasing the ratio T_i/T_e increases the threshold for ITG modes, leading to the favorable hot-ion regime. The effect of density gradient is more subtle. For pure ITG modes, density peaking is stabilizing. On the other hand, TEMs are destabilized by the density gradient. An important parameter that controls the transition from one regime to the other is the collisionality. For high collision frequencies, ITG modes are dominant, whereas in weakly collisional regimes, TEMs are usually unstable.

A common way to assess the overall stability is to compare the $E \times B$ shear rate $\omega_{E \times B}$ to a maximum linear growth rate γ_{lin} (Refs. 152, 153, and 154). Full stabilization is often considered to be reached when $\omega_{E \times B} > \gamma_{lin}$. This simple criterion has been widely used to assess the formation of barriers. In particular, two operational criteria can be built on the basis of this simple rule. Assuming for practical reasons that the electron temperature gradient length L_{T_e} is a good estimate of all gradient lengths, the linear growth rate γ_{lin} of ITG/TEM modes can be approximated as in Eq. (17) and the diamagnetic part of the $E \times B$ shearing rate in Eq. (18):

$$\gamma_{lin} = \frac{c_s}{\sqrt{RL_{T_e}}} \tag{17}$$

and

$$\omega_{E \times B} = \frac{\rho_s c_s}{L_{T_e}^2} \ , \tag{18}$$

where c_s is the sound speed. The condition $\omega_{E \times B} > \gamma_{lin}$ then transforms into a threshold for

$$\frac{\frac{R}{\sqrt{L_{T_e}}} \rho_s}{L_{T_e}} \ . \tag{19}$$

For reason of simplicity, this criterion is written as

$$\rho_T^* = \frac{\rho_s}{L_{T_e}} > \rho_{T_{crit}}^* \ . \tag{20}$$

In principle, $\rho_{T_{crit}}^*$ depends on the magnetic shear α and the Mach number (which comes into play via the contri-

bution of the toroidal velocity to the flow shear) and possibly on the density gradient and impurity content. In practice, an analysis of the JET database shows that this criterion works well when choosing a constant value $\rho_{T_{crit}}^* = 0.014$ (Ref. 155). Another criterion corresponds to a loss of "stiffness." Stiffness means here that the temperature gradient length (for ions or electrons) is close to a threshold value $R/L_T = R/L_{T_{crit}}$. A natural definition of an ITB then corresponds to a region in which the threshold is well above the L-mode value. This leads to a criterion of the form $R/L_T > R/L_{T_{crit}}$ for the ITB formation. This rule can be written as a condition on the ratio of core-to-edge temperature. A large class of ion ITBs was found to satisfy this criterion using a critical value $R/L_{T_{crit}} \approx 6$ (Ref. 53). It should be noted here that these kinds of criteria can be considered only as working hypotheses for practical purposes to detect experimentally the existence, location, and strength of the ITBs. To really verify experimentally the existence of the ITB, one must study, for example, the heat wave propagation across the layer of the "expected" ITB and, from the damping of the heat wave, to deduce ultimately whether an ITB exists or not.

The question of a power threshold to trigger an ITB is not an easy task to answer. The ITBs can be formed in a variety of plasma conditions; they can appear at various plasma radii, on various plasma profiles at various plasma power levels, and with various plasma heating systems, different q profiles, etc.[156] For example, JET experiments with a monotonic q profile (positive magnetic shear) indicated that the power threshold needed to form an ITB increases with increasing toroidal magnetic field B_T (Ref. 156). However, this scaling dependence on B_T disappears if the q profile is tailored, for example, with LHCD, to be reversed (negative magnetic shear). Consequently, it is unlikely that a universal power threshold, similar to that of the L-H transition, which is based only on global plasma parameters, can be found for ITB formation. In fact, since the ITB formation is clearly linked to the local values of parameters such as magnetic shear, q profile, $E \times B$ velocity shear, etc., a threshold to form an ITB depends on the local physics parameters rather than on the level of heating power. In addition, it was found on JET that the minimum power level required to observe a local transport reduction (weak ITB) is often significantly lower than the value at which steep pressure gradients (strong ITB) can be achieved.[156] Furthermore, the actual trigger mechanism of the ITB may well be different from the mechanisms governing the subsequent sustainment and dynamics of the ITB. There is strong experimental evidence on JET that the role of integer surfaces of the q profile in triggering ITBs is significant, both in positive magnetic shear[142] and negative magnetic shear at q_{min} (Ref. 143), whereas their impact on ITBs is less clear after the triggering event. Very recently, it was reported that the triggering event of the ITB actually occurs just before, typically a few tens of milliseconds,

$q_{\min}$ reaches the rational surface m_0/n_0 (Ref. 157). This result is based on the fact that the steepening of the temperature gradients is observed to occur before the appearance of the Alfvén cascades. The role of integer and rational surfaces of q is discussed in more detail in Sec. V.E. Moreover, the ITBs can be categorized into strong ITBs, in which turbulence is fully suppressed and the transport is reduced to neoclassical levels, and weak ITBs, in which turbulence is partly suppressed and transport stays above the neoclassical level but below the level without the ITB.

V.B.2. Local Stability Analysis

The criteria described above are quite useful for practical purposes, in particular, for real-time control of fast analysis of data.[158,159] However, a more detailed and local analysis is needed to better understand the physics at work. This can be done by making a more accurate use of the criterion $\omega_{E\times B} > \gamma_{lin}$. Several fluid and kinetic stability codes are currently used in JET to calculate the growth rates of ITG/TEM modes and the flow shear rate.[160-163] Fluid linear growth rates are usually estimated by using the Weiland[164] and Rogister[165] models. Kinetic growth rates require numerical tools such as the KINEZERO (Ref. 31) or GS2 (Ref. 38) codes. The $E \times B$ velocity shear is calculated from the radial force balance equation using the neoclassical estimate for the poloidal rotation velocity from the NCLASS code,[139] or by using the expression given by Ref. 166. An example is given in Fig. 40, where these models are compared on JET pulse 51976 (details can be found in Ref. 167). Most models do predict stabilization, due to negative (or

weak) magnetic shear and/or the Shafranov shift to trigger the barrier. Here and usually when there is negative magnetic shear, the Weiland model predicts a growth rate that remains larger than the flow shear rate. This model is being updated to better account for magnetic shear stabilization, and the progress made is reported in Sec. V.D.2.

The JET database has been analyzed using a systematic stability analysis. A linear empirical threshold condition shown in Eq. (21) has been found for the onset of the ion ITBs using the JET positive magnetic shear ITB database[168]:

$$\frac{\omega_{E\times B}}{\gamma_{lin}} > 0.68s - 0.095 \ , \tag{21}$$

where

$$s = \text{magnetic shear}$$

$$\omega_{E\times B} = \text{flow shearing rate}$$

$$\gamma_{lin} = \text{approximate value of the linear growth rate of the ion temperature gradient instability.}$$

This empirical threshold condition for the ITB formation provides a clear indication of the strong correlation of the magnetic shear and the $E \times B$ flow shearing rate when the ITB forms. The database consists of ITB discharges from a wide range of plasma parameters; the toroidal magnetic field varies between 1.8 and 4.0 T, the plasma current between 1.8 and 3.5 MA, the auxiliary heating power between 10 and 30 MW, and the diamagnetic energy between 3 and 12 MJ. The linear
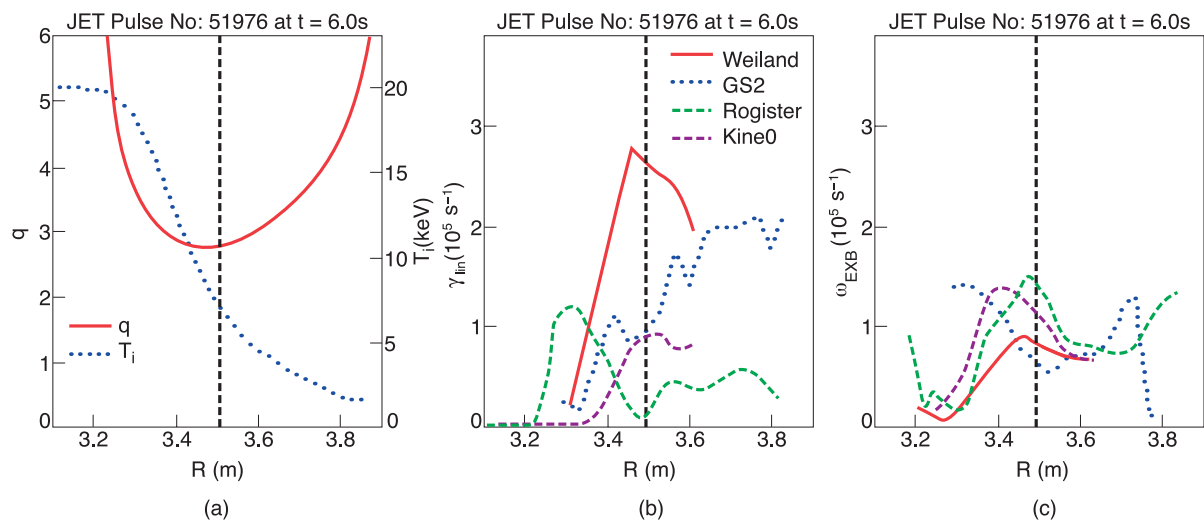

Fig. 40. Profiles of safety factor and ion temperature, linear growth rates, and the velocity shear rate of JET pulse 51976 ($I_p = 2.5$ MA, $B_T = 3.45$ T, $P_{NBI} = 21$ MW, and $n_{e0} = 3.5 \times 10^{19}$ m^{-3}) at $t = 6$ s. The vertical line shows the radial footpoint of the ITB (reproduced from Ref. 167).
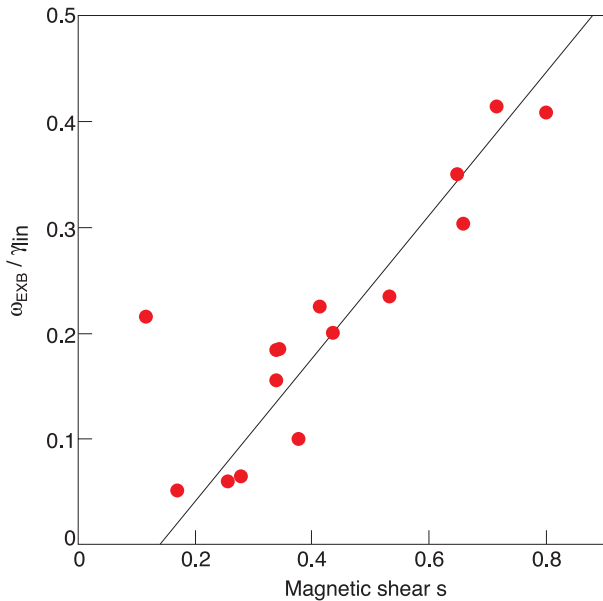
Fig. 41. $E \times B$ flow shearing rate divided by an estimate of the ITG growth rate versus magnetic shear at the location and onset of the ITB, yielding the empirical ITB threshold condition (reproduced from Ref. 168).

empirical threshold condition is illustrated in Fig. 41. The scatter plot exhibits a linear trend, indicating that a linear regression is reasonable. The estimated regression line takes the form $\omega_{E \times B}/\gamma_{lin} = 0.68s - 0.095$ in Fig. 41.

The trend to need larger $\omega_{E \times B}$ shearing rates with increasing magnetic shear is consistent with other, similar works.[169,170] This is also predicted by theory since the growth rates of ITGs and TEMs are expected to increase with magnetic shear, unless the magnetic shear reaches large values ($s \geq 1$), after which the growth rates start to decrease again.[152] However, at the footpoint of the ITB, the value of the magnetic shear is always smaller than 1 in JET, as shown in Fig. 41. This empirical threshold condition does not reveal whether a separate trigger, such as a rational surface of q, is needed for the ITB to form. The triggering event of an ITB may be different and separate from the mechanisms that after triggering govern the physics of the ITBs (Refs. 142 and 143). In this context it would mean that the rational surfaces of the q profile act as the triggering mechanism for the ITB, whereas all or some of the other aforementioned mechanisms take over to govern the physics (existence, expansion, shrinkage, strength, etc.) of the ITB after the triggering event. The further evolution of the ITB, at least in the case of strong ITBs, probably has some positive feed loop in some of the mechanisms to further help in suppressing the instabilities and strengthening the ITB.

V.B.3. First- and Second-Order Transitions and Consequences for the Power Threshold

The transition types of transport barriers (both ITBs and ETBs) are traditionally classified into first- and second-order transitions. A first-order transition is characterized by a sudden change of gradient, which occurs when the control parameter (usually the heat flux) crosses a threshold. On the other hand, in the second-order transition the temperature gradient varies continuously, and there is no obvious power threshold (or heat flux threshold); for example, the electron ITB forms if just the magnetic shear is negative enough, even at minimal power level. For a first-order transition, the threshold in the control parameter, like the heat flux, depends on local plasma parameters and thus varies from plasma to plasma, not allowing us to define, for example, an unambiguous universal power threshold, as already discussed in Sec. V.B.1.

A first-order transition may occur because of the reinforcement of flow shear with gradients. This is a consequence of the force balance equation, which indicates that the radial electric field in a tokamak increases with the density and temperature gradients and also with the toroidal velocity. This link allows a positive loop in which enhanced gradients lead to a larger shear rate, which in turn further improves the confinement. A bifurcation is therefore expected above a critical flux.[171,172] It is stressed here that mechanisms other than flow shear stabilization may lead to a first-order transition. For instance, a positive loop may be provided by the interplay between current and pressure profiles via the bootstrap current. Also α stabilization may lead to a positive feedback on the pressure gradient.[173] Finally, we note that first-order transitions are characterized by hysteresis, i.e., different critical fluxes for the forward and back transitions.

There exist several mechanisms for explaining a second-order transition. One mechanism is provided by a strong increase of the instability threshold within a layer (because of combined large α and negative magnetic shear, for instance), in other words, a linear stabilization of modes. Nonlinear effects may also lead to an effective monotonic curve, which leads also to a soft transition.

The question of first- or second-order transition is quite important since it determines the existence of a power threshold, but also the barrier robustness, since hysteresis improves the barrier resilience to external perturbations. It is found that a minimum heating power is needed to trigger an ITB in JET (Ref. 156). Impressive hysteresis effects also have been observed.[174] However, none of these observations demonstrates that a first-order transition takes place since in both cases the current profile was found to be very different. In fact, it was found that the power threshold is sometimes very low, when the current profile is optimized.[175] This latter observation

indicates that if the transition is first order, the transition curve cannot be universal. In fact, very low values of the power threshold rather advocate in favor of a second-order transition. It remains that flow shear stabilization is needed when the magnetic shear is not low enough, for example, in positive shear plasmas, and also likely ensures the robustness of the barrier.

V.C. Experiments Dedicated to Understanding the Physics of ITBs

V.C.1. Heat- and Cold-Pulse Propagation Across ITBs

Electron heating power modulation experiments have been used to probe the physics of ITBs by looking into the propagation of the heat pulses on JET (Ref. 176). The heat pulses are produced with modulated electron heating power by ICRH system. By Fourier transforming the temperature data at the modulation frequency, it is possible to obtain the amplitude and phase of the propagating heat wave. Two important questions under debate regarding the physics of the ITBs that can be answered are

1. whether the improved confinement is limited to a narrow layer or rather extends to the whole core region inside the ITB layer (and then the ITB would not be called a layer)

2. whether the ITB is a region of stiff transport characterized by a threshold in R/L_{T_e} larger than in conventional plasmas or rather a region below

threshold where turbulence is suppressed, leading to a loss of stiffness.[18]

In addition, the question as to whether ITBs experience first- or second-order transition can be studied by following the propagation of the cold pulse launched from the edge of the plasma.

The main plasma profiles as well as the amplitudes A and phases φ of the heat wave are illustrated in Fig. 42. ICRH used in the mode conversion scheme produces two heat waves, the mode-converted (mode conversion) one propagating from the outer region toward the center and the fast wave (FW) one propagating from the center outward. Regarding the two questions outlined in this section, the following conclusions can be drawn:

Figure 42b shows sharp discontinuities in the heat wave propagation (i.e., in the slopes of the A and φ profiles), both at the foot and at the top of the high-∇T_e region. This indicates that at least for these reversed shear ITBs with dominant ion heating, the ITB is indeed a narrow layer with low χ_e embedded in a higher χ_e plasma, rather than a general improvement of confinement in the whole core region extending to the center of the plasma. According to KINEZERO simulations, ITG is the dominant microinstability in this plasma.[177]

Figure 42b also shows that the heat wave is strongly damped when meeting the ITB from either side. This is consistent with a situation of complete loss of stiffness due to the plasma having become fully subcritical with respect to an increased threshold value. In this case, χ_e does not depend on ∇T_e, the perturbative χ_e coincides with the power balance χ_e and is low, the two heat waves
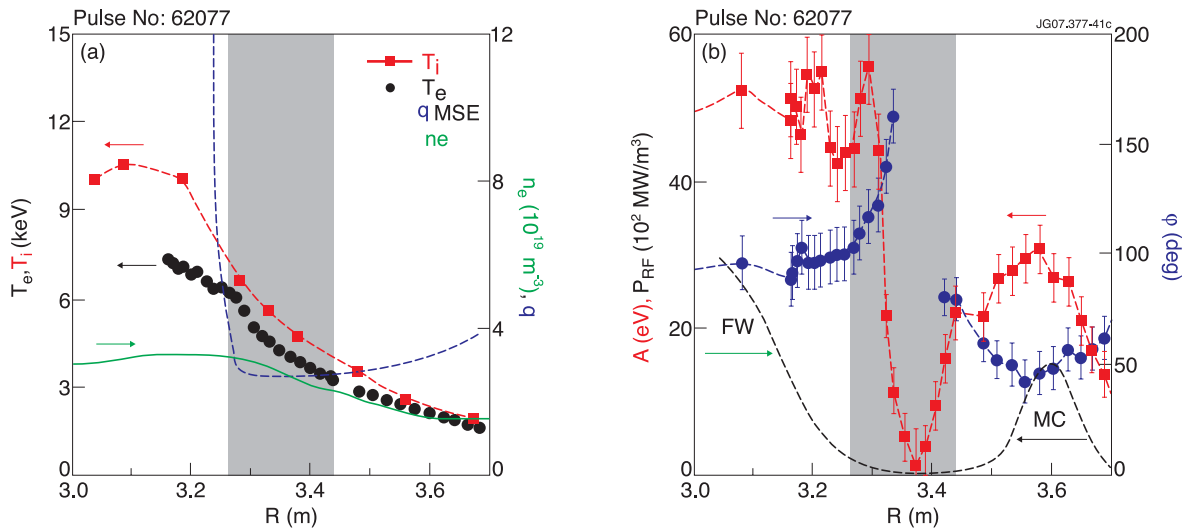
Fig. 42. (a) Experimental profiles of T_e, T_i, n_e, and q for shot 62077 ($I_p = 2.6$ MA, $B_T = 3.25$ T, $P_{NBI} = 18$ MW, $n_{e0} = 4 \times 10^{19}$ m^{-3}, ^{3}He $\sim 20\%$, and $f_{ICRH} = 37$ MHz) at $t = 5.5$ s. The ITB region is highlighted. (b) Profiles of Fourier component of A (red squares) and φ (blue circles) at the modulation frequency (20 Hz) during the time interval 5.5 to 5.7 s. The rf power deposition profiles are also plotted (dashed black line) (reproduced from Ref. 176).

are strongly damped and cannot cross the ITB, and, moreover, the phase exhibits a sharp jump.

Another observation is that the inner slope of the amplitude A within the ITB layer is steeper than the outer one, likely indicating a nonuniform turbulence stabilization and χ_e within the ITB (Ref. 176). This is in agreement with the experiments in which the cold-pulse induced at the edge showed first a growth when meeting the foot of the ITB and then strong damping farther inside.[45] The growth of the cold pulse when meeting the foot of the ITB can be regarded as a strong indication in favor of the second-order transition since no growth would be expected in the first-order transition.[176] This behavior has been recovered with turbulence simulations (see Sec. V.E.1).

V.C.2. Turbulence Measurements in ITB Plasmas

Reflectometry is used to measure the core turbulence on JET (Ref. 178). The core and edge density fluctuations are monitored using four X-mode heterodyne reflectometer channels (at 75, 92, 96, and 105 GHz), and 10 O-mode heterodyne reflectometer channels (between 18 and 69 GHz). The three main observations are as follows:

1. The formation of a core region of high radial shear in the plasma toroidal velocity is correlated with the suppression of long-wavelength turbulence ($k_\perp \rho_i \ll 1$) and with a decrease in the ion thermal conductivity χ_i in plasmas with dominant ion heating.[179]

2. The formation of the electron ITB is correlated with a suppression of shorter-wavelength turbulence ($k_\perp \rho_i \sim 1$) (Ref. 180).

3. At least in the case of dominant electron ITBs with no or small NBI heating resulting in no or low levels of ITG turbulence, low-frequency ($f < 50$ kHz), long-wavelength fluctuations (dominantly TEM) are reduced for the whole region from the plasma center out to the foot of the electron ITB (Ref. 181).

The measured fluctuation levels showing clearly point 3 is illustrated in Fig. 43. In plasmas with dominant electron heating (pure or dominant electron ITBs), the turbulence reduction coincides with a region of negative shear and reduced electron thermal diffusion (calculated with the TRANSP code), as shown in Fig. 43 (Ref. 180). The analysis of turbulence measurements also suggests that the dominant instabilities are TEMs, and their suppression due to negative magnetic shear leads to the formation of the ITB.

It is interesting to note here a difference between the above results in dominant TEM plasmas, for which the electron ITB is a whole region inside the foot, and those with power modulation reported in Sec. V.C.1, in which the ITG turbulence was found to be the dominant micro-instability[177] and the electron ITB appeared to be a nar-
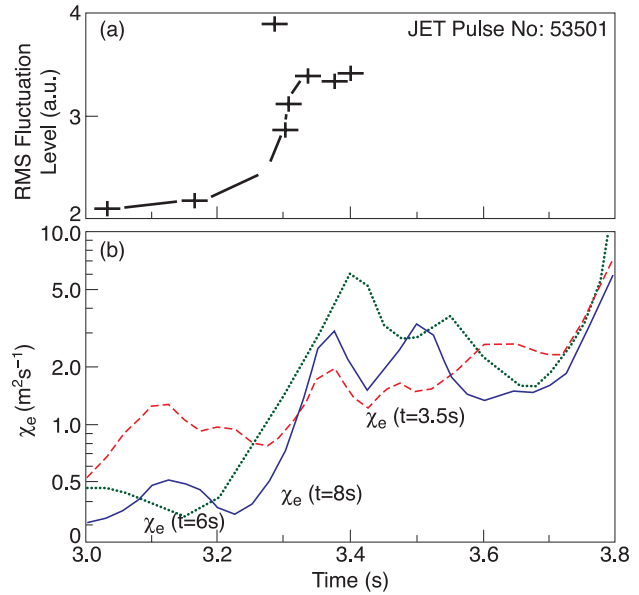

Fig. 43. (a) The rms fluctuation level profile (3 to 500 kHz) and (b) the electron thermal diffusivity χ_e profile from TRANSP at various times in electron ITB shot 53501 ($I_p = 2.4$ MA, $B_T = 3.45$ T, and $n_{e0} = 1.2 \times 10^{19}$ m^{-3}) (reproduced from Ref. 180).

row layer. This suggests that turbulence stabilization and the physics of the ITB may be governed by two different mechanisms between the two types of plasmas/experiments: In the second case the ITG-driven component of electron transport would play a significant role and would be less sensitive to magnetic shear, both the toroidal and even more the slab ITG branch, so that they would survive in the most internal part near the axis and be stabilized only in a narrow layer. In addition, there was a current hole in the plasma center in the plasmas with the power modulation, and therefore the analysis of the propagation of the heat between the center of the plasma and the ITB layer might be affected by the peculiarities due to the current hole, removing the apparent contradiction between the two different results.

V.C.3. Dedicated Experiments to Explore the Physics of ITBs

An experimental database of ITB pulses with dominant electron heating, characterized by $T_e > T_i$, has been created in JET (Ref. 181). The relation between the radial position of the electron ITB and the q profile is an important issue, ideally clarifying the role of magnetic shear and rational surfaces of q in the physics of ITBs. The experimental results show that the electron ITB moves inward at the same rate as the radius of the minimum value of the q profile but seems to be located in the negative shear region. The latter observation is consistent with linear stability analysis using the KINEZERO

code[182] and also with the stability code LORB5 (Ref. 183). The footpoint of the electron ITB is typically at a 5- to 10-cm smaller radius than the minimum value of the q profile, which is, however, still inside the error bars of the measurements. Therefore, it cannot be excluded that the footpoint of the electron ITB actually coincides with the minimum value of the q profile. Concerning the triggering of the ITB, there is strong evidence in general that there is a clear correlation between the triggering of the ITB (and its radial location) and the location of the integer surface of q_{min} ($q = 2$ or 3) (Ref. 143). After the triggering, there seems to be no link between the radial location of the ITB and the absolute value of q, since q is strongly evolving with time. As a consequence, it looks very plausible that although the triggering of the ITB is often associated with the integer values of q (at least with low heating power), the further evolution of the ITB after the trigger is not linked to those but is governed by other physics mechanisms such as negative magnetic shear, the $E \times B$ flow shear, and others discussed in Sec. V.B.1. The roles of integer surfaces of q and triggering versus further mechanisms governing the physics of the ITB are discussed more extensively in Sec. V.E and in the following paragraph.

Most of the ion ITBs on JET have been achieved with strong NBI heating and thus strong external toroidal momentum input. However, it has been possible to form an ion ITB without any momentum input with significant amount of ICRH in an ion heating scheme.[184] In these experiments, intense LHCD creates first an electron ITB in the region of negative magnetic shear. The ion ITB tends to appear when q_{min} crosses the value of 2, similar to those reported in Ref. 143. The behavior of these ion ITBs under those plasma conditions suggests the following two important implications:

1. Negative magnetic shear is not a sufficient condition for an ion ITB to form.

2. No large toroidal rotation and thus no $E \times B$ flow shearing rate above the normal diamagnetic level is necessary for the ion ITBs to form.

However, the second point was not confirmed from the shearing rate point of view since the predictions for the growth rates were not significantly above the diamagnetic levels of the $E \times B$ flow shear in those plasmas. Concerning point 1, it is of course clear that negative magnetic shear is not a necessary condition either for the ion ITB formation, for example, from Refs. 142 or 185.

The role of the q profile and in particular that of the magnetic shear was emphasized also in Ref. 162, in which one discharge shows a clear ITB whereas in another with almost identical $E \times B$ the flow shear does not show any ITB. The only difference between the two discharges was that the one with an ITB had 2 MW of LHCD, whereas the one without an ITB did not have LHCD. This resulted in negative magnetic shear for the pulse with an ITB (and

LHCD) and positive magnetic shear for the pulse without it. Although this experiment does not rule out the role of $E \times B$, it tends to emphasize the importance of negative magnetic shear in governing the physics of the ITB.

V.D. Predictive Transport Modeling of JET ITB Plasmas

There are several ways to carry out predictive transport simulations of ITBs, and the conclusions based on the simulation results may depend on the simulation methodology adopted. For example, the predictive simulations can be either time dependent, aiming at reproducing the trigger, expansion, or shrinkage and the collapse of the ITB, or, alternatively, a simulation around a given stationary state at one time slice. The time-dependent transport simulations of ITBs challenge maximally the transport models since the whole process governing the dynamics of the ITBs includes nonlinear phenomena such as bifurcations and instability thresholds, large changes in the plasma profiles from the preheating phase until the high-power phase, and strong interaction between different plasma profiles. Another example of having a different simulation approach or methodology is that one can predict, for example, electron and ion temperatures while taking the density, q profile, and toroidal rotation profile from the experimental database, versus fully predictive simulations in which all of them are predicted.

V.D.1. Empirical and Semiempirical Transport Models

The original Bohm–gyro-Bohm transport model,[13] modified to include the empirical ITB threshold condition[168] (discussed in Sec. V.B.2), has been extensively used to predict ITBs in JET. The turbulence stabilization mechanisms to form an ITB in the Bohm–gyro-Bohm model are based on the combined effect of the $E \times B$ flow shear versus a simple estimate for the instability growth rate and the magnetic shear. The model is described in detail in Sec. VI.B. The stabilizing effect of the α stabilization has also been included in some simulations.

The Bohm–gyro-Bohm transport model has turned out to be the most robust model to predict the time dynamics of the ITB evolution in JET plasmas.[186] It usually can predict the onset and time dynamics of the ITB for electron and ion temperatures, density, and toroidal rotation within a fair accuracy. This is illustrated (dashed lines) in Fig. 44 for one JET discharge with positive magnetic shear (pulse 46664) and another with negative magnetic shear (pulse 53521). The main plasma parameters for these discharges are $I_p = 3.4$ MA, $B_T = 3.4$ T, $n_{e0} = 4 \times 10^{19}$ m^{-3}, and $P_{NBI} + P_{ICRH} = 22$ MW for shot 46664 and $I_p = 2.0$ MA, $B_T = 3.4$ T, $n_{e0} = 5.5 \times 10^{19}$ m^{-3}, and $P_{NBI} + P_{ICRH} = 22$ MW for shot 53521. Both simulations have been carried out from the preheating phase until the end of the high-performance phase, at the end of which are the profiles shown in Fig. 44. Although the model does not reveal the deep insight of the physics of
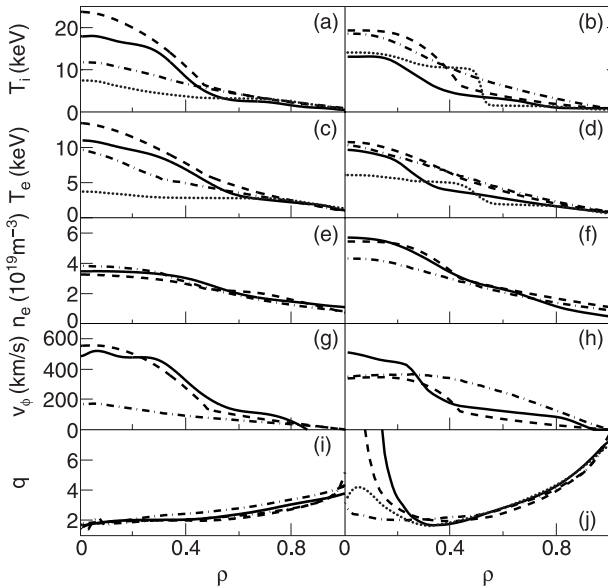
Fig. 44. Profiles of (a) and (b) the ion temperature, (c) and (d) the electron temperature, (e) and (f) the electron density, (g) and (h) the toroidal rotation, and (i) and (j) q for JET discharges 46664 (I_p = 3.4 MA, B_T = 3.4 T, $P_{NBI} + P_{ICRH}$ = 22 MW, and $n_{e0} = 4 \times 10^{19}$ m^{-3}) at t = 6.0 s (left-hand side) and 53521 (I_p = 2.0 MA, B_T = 3.4 T, $P_{NBI} + P_{ICRH}$ = 22 MW, and $n_{e0} = 5.5 \times 10^{19}$ m^{-3}) at t = 12.0 s (right-hand side). The solid lines correspond to the experimental data and the dashed, dashed-dotted, and dotted lines to the predictions with the Bohm–gyro-Bohm, Weiland, and GLF23 models, respectively (reproduced from Ref. 186).

the ITBs because of its empirical nature, it has been extensively applied in order to understand and prepare experiments with the real-time control of ITBs and the q profile.[187]

The model has emphasized the combined role of $E \times B$ flow shear and magnetic shear in governing the physics of the ITBs. In addition, there is an indication of the importance of the α stabilization, shown in the ITB simulations of a multitokamak database of JET, JT-60U, and DIII-D plasmas.[186] The model also suggests that the long-wavelength turbulence is suppressed inside the ITB (from the center up to the footpoint of the ITB) and not just within the narrow layer around the foot of the ITB, while the short-wavelength turbulence remains also in that region.[188]

Another empirical transport model used to predict the electron ITBs on JET is called the RTP transport model.[189] The model is based on the radial variations in the electron diffusivity at integer and rational surfaces of the q profile. The model predictions are in fairly good agreement with the JET ITB experiments with positive magnetic shear.[190] The model does not give any consideration on transport channels other than T_e, but because

of that, it shows that the electron ITBs may be governed and explained, at least in part, by physics mechanisms different from those of ion ITBs. Another widely used empirical transport model is the CGM (Refs. 17 and 18). It has been mainly used to model the transient transport experiments of the heat-pulse propagation (power modulation) and cold-pulse propagation from edge induced by laser ablation or shallow pellets. The model has been able to reproduce qualitatively the experimental results discussed in Sec. V.C.1 (Refs. 176, 191, and 192) and also in Sec. II.

V.D.2. Physics-Based Transport Models

The agreement of the model predictions with experiment when using the physics-based transport models depends strongly on the simulation methodology, i.e., on whether the simulations are carried out in a time-dependent manner and in a fully predictive (equations for T_e, T_i, n_e, q, and v_{tor} solved) or partly predictive (some of them imposed) way. The Weiland model[164] and the GLF23 transport model[39,135] have been used to predict the time evolution of the ITBs in the multitokamak database with JETTO (Ref. 43) and CRONOS (Ref. 193) transport codes. Both transport models include qualitatively the same microturbulence stabilization mechanisms, i.e., $E \times B$ flow shear, magnetic shear, α stabilization, the dilution effects, and the density gradient. The predicted profiles at the end of the high-performance phase for two JET discharges are illustrated in Fig. 44 (Ref. 186). The Weiland model (dashed-dotted lines) does not predict a clear ITB for any of the plasma profiles. The linear growth rate is only weakly dependent on magnetic shear in the Weiland model. However, both the experimental and empirical evidence discussed earlier show the strong dependence of ITBs on the magnetic shear and the q profile. Therefore, the inability of the model to predict ITBs indirectly further emphasizes the major role played by the magnetic shear in governing the physics of the ITBs.

The GLF23 transport model (dotted lines) often predicts an ITB, but not at the right location. The simulation results are very sensitive to variations, for example, in the multiplier of the $E \times B$ flow shear, q profile, and Z_{eff}, which manifest themselves in the simulations as the radial location of the ITB moving continuously. It is worth mentioning that the multiplier of the $\omega_{E \times B}$ term in GLF23 in these simulations was 1, whereas more recent simulations using the global gyrokinetic simulations with GYRO suggest that the appropriate coefficient in front of the Waltz formula is not 1 but rather 0.5 (Ref. 194). The GLF23 transport model tends to predict the heat transport outside the ITB more accurately than the other transport models. It is also able to predict ITBs in only one of the transport channels but not necessarily in another channel, whereas, for example, the Bohm–gyro-Bohm model always predicts an ITB in either all or no transport channels. This is a serious deficit in the Bohm–gyro-Bohm

transport model. It should be noted here that at the time of writing of Ref. 186, the equations for density and toroidal rotation were not available in the CRONOS code, and thus the predictions for those two profiles with the GLF23 transport model in CRONOS code could not be performed.

When the simulations are run in a time-independent mode, finding a solution of a stationary state at a given time slice, both the Weiland model with a version depending more strongly on magnetic shear[195] and the GLF23 model[135] are able to predict ITBs rather well in some cases. This indicates that although the physics of the ITBs can be explained to some extent with the physics-based transport models, the time dynamics of the ITBs, including the onset, nonlinear interaction between the different plasma profiles, bifurcative processes with thresholds, etc., are understood to a much smaller extent. One reason could be that none of the models takes into account the role of the integer surfaces of the q profile as a separate ITB-triggering mechanism. This issue is further discussed in Sec. V.E. Because the predictions with the physics-based models are in better agreement with standard ELMy discharges than with ITB ones, it becomes clear that our understanding of the physics of the ITBs lags significantly behind the knowledge of the heat, particle, and momentum transport physics in plasmas without the barriers. For impurity transport, the situation is somewhat more satisfactory since the pinch velocity within the barrier is often found to agree with the values predicted by neoclassical theory.[97]

V.E. Turbulence Simulations of JET ITBs

V.E.1. Fluid Simulations

The TRB (Refs. 196 and 197) and CUTIE (Ref. 198) fluid codes have been used to simulate ITBs in JET. TRB is a full-torus, global electrostatic code solving fluid equations for ITGs and TEMs. The evolution of electron density and pressure, vorticity, parallel ion velocity, and ion pressure is computed at the fixed flux, whereas the q profile is frozen. CUTIE is a global electromagnetic fluid turbulence code. It solves the evolution equations for the fluctuating electron density, electron and ion temperatures, velocity, potential, and magnetic field, but it does not include trapped particle physics.

Ion ITBs are found with the TRB code. Improvement comes from a mixture of stabilization via negative magnetic shear and rarefaction of resonant surfaces (in particular close to a safety factor that is a low-order rational number).[167] This "gap" in the density of resonant surfaces is wider when q_{min} is close to a low-order rational number (see Fig. 45). Also, several gaps may appear simultaneously, leading to multiple barriers. This mechanism is supported by recent measurements based on Alfvén cascades, which show that the ITB forms before the appearance of a rational value of q_{min} (Refs. 157 and 199). Nevertheless, these theoretical results were not recovered in gyrokinetic simulations done with the GYRO code, which indicate that nonresonant modes fill the gap.[200]
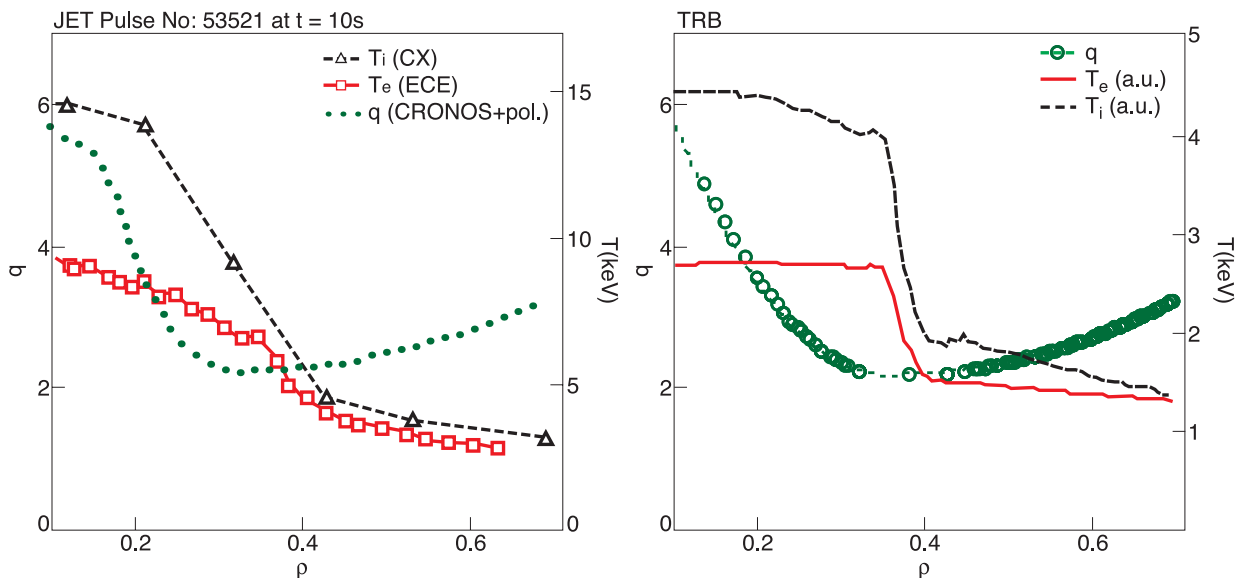

Fig. 45. Left: Experimental profiles of safety factor and electron and ion temperatures of JET pulse 53521 at $t = 10$ s. Right: TRB turbulence simulation showing the predicted ITB with the same q profile. Circles are the positions of $k_\theta \rho_{s0} < 1$ resonant surfaces on the q profile (reproduced from Ref. 167).

The CUTIE code also finds that rational values of q_{min} are important.[201] This comes from a turbulent dynamo effect, which modifies the local magnetic shear, and a localized velocity shear generated by turbulence. This mechanism is difficult to verify experimentally, although large transients in the $E \times B$ flow have been observed in JET (Ref. 140) and also on TFTR (Ref. 202) and DIII-D (Ref. 203).

Finally, a third explanation has been proposed for the role of rational surfaces, namely, the onset of MHD modes located at rational values of q that generate a localized velocity shear.[142] This explanation does find some support from the correlation observed in JET between ITB formation and MHD activity in positive (optimized) shear plasmas. On the other hand MHD activity is not always observed in reversed shear plasmas, apart from the Alfvén cascade itself. However, tearing modes located at $q = 2$ surfaces may be difficult to detect.

ITBs in the electron transport channel are also found by the TRB code.[204] The effect of negative magnetic shear has been confirmed in the TRB code. In the latter simulations, an electron transport barrier appears when the magnetic shear is negative. This effect is amplified for values of α of the order of unity. For electron modes, theory predicts stability when $s < 3\alpha/5 - 3/8$ (Ref. 205).

Both the CUTIE and TRB codes have been used to simulate plasmas with pellet injection.[206] With a shallow pellet (pellet ablated at the plasma edge well outside the ITB), both codes reproduce the general features of the experiment. In particular, it is found that the ITG and trapped electron turbulence level increases as a consequence of pellet injection, leading to the fast relaxation of the postpellet density profile observed experimentally. Also, the barrier is found to survive the shallow pellet injection, as in the experiment. For deep pellet injection, on the contrary, differences appear between the TRB and CUTIE findings. TRB simulates well the increase of turbulence and associated diffusivity following pellet injection, but it is not able to reproduce the destruction of the ITB that is observed in experiments. CUTIE simulates reasonably well most of the experimental features. In particular, it does find the loss of the ITB when pellet injection is too deep or the barrier is not strong enough, due to a change of the zonal flow dynamics.

V.E.2. Nonlinear Gyrokinetic Simulations

The nonlinear gyrokinetic codes GS2 (Refs. 38 and 207) have been used to analyze JET plasmas. All gyrokinetic codes confirm that stability is improved before the ITB formation. On the other hand, a quantitative agreement is rarely found in nonlinear regime. For instance, careful simulations of pulse 51976 with the GS2 code led to calculated fluxes much larger than the experimental values.[160] One explanation is that flow shear was not included in these simulations. However, this may not be the unique explanation. These simulations with fixed gradient are delicate since a small change of gradient may lead to very different fluxes (profile stiffness). Therefore, simulations done at fixed flux may improve the situation in future simulations.

V.F. Conclusion

This section is a summary of the studies carried out in JET to understand the physics of ITBs. Experimental, empirical, modeling, and theoretical studies are reported. It becomes clear that the triggering, formation, and dynamics of the ITBs are rich in phenomena governing the physics of the ITBs. It is unlikely that a universal power threshold, similar to that of the L-H transition, which is based only on global plasma parameters, can be found for ITB formation. The practical $\rho^*_{T_e}$ criterion was derived from the JET ITB database to identify the existence of an ITB and classify its strength (strong versus weak ITBs). This criterion is, however, only indicative of an ITB, but indeed it is very useful in detecting the existence and location of an ITB, in particular in real-time control experiments[158,159] and modeling.[187]

Many experimental results in JET are consistent with barrier dynamics controlled by flow shear and local magnetic shear (in a broad sense, i.e., including α stabilization). These results also indicate that the onset of an ITB is highly sensitive to the profile of the safety factor (q profile). Part of these observations can be explained by the parametric dependences of the linear growth rate and are qualitatively consistent with turbulence simulations. Models based on a transport reduction due to magnetic shear combined with velocity shear also reproduce the data in a satisfactory way. Pure electron transport barriers usually develop in regions in which the magnetic shear is negative. Also, neoclassical theory predicts that the $E \times B$ velocity shear is small in this case, since the density and ion temperature gradients are small and there is no external source of toroidal momentum. Hence, it can be safely said that the current profile plays a major role in the formation of electron ITBs. The situation is less clear for ion transport barriers. Many ion barriers in JET appear at zero magnetic shear and low-order rational q_{min}. Ion ITBs may develop with ICRH only, i.e., without an external source of toroidal momentum. Finally, the level of $E \times B$ velocity shear rate that is needed to trigger a barrier decreases when the local magnetic shear becomes smaller (when $s < 1$). These observations suggest that a strong $E \times B$ velocity shear rate is not mandatory for ion ITB formation, provided that the q profile is appropriate. This conclusion must be softened by the fact that diamagnetic flow shear is never negligible when an ion barrier builds up. Hence, it cannot be fully ascertained that an optimized q profile alone is sufficient for ion ITB formation. The ITB on the toroidal momentum transport channel appears simultaneously with the ion ITB, and thus the turbulence stabilization mechanism is supposed to be the same as for the ion heat-transport channel.

The interplay between flow shear and magnetic shear is also related to the question of the transition order. Thanks to the analysis of cold-pulse propagation across ITBs, the amplification of the thermal wave that is observed at the ITB is consistent with a second-order rather than first-order transition.

An explanation based on a combination of flow shear and magnetic shear is unable to explain the full range of barriers observed in JET. There are two reasons at least for this statement: the role of rational q_{min} and the coexistence of several barriers. The favorable role of a low-order rational value of the minimum safety factor has been confirmed thanks to the observation of Alfvén wave cascades. Also, a transition is often observed between a single barrier localized at negative shear and a double barrier, when q_{min} crosses a low-order rational number. Finally, coexistence of barriers has been observed both in electron and ion channels. Three explanations have been proposed to explain the role of rational q_{min}:

1. the onset of MHD modes located at rational values of q that generate a localized velocity shear

2. the enhancement of turbulent flow generation close to rational q values

3. the existence of gaps in the density of magnetic surfaces in places where the safety factor is a low-order rational number.

To date there is no strong argument for endorsing or dismissing each of these mechanisms. Hence, this question remains an open issue.

The results for predictive modeling are contrasted. Although semiheuristic transport models have been proved to simulate JET discharges with a fair degree of accuracy, theory-based models often fail to predict the barrier formation at the right time and location. When the barrier formation is correctly predicted, the location and/or the shape of the ITB are sometimes poorly reproduced. Possible ingredients missing in the models are, first, that most transport models do not encompass a particular role of rational surfaces, which is known to be important from experiment. Second, they usually assume that the poloidal flow is consistent with the neoclassical prediction, whereas anomalous values have been observed within the ITBs on JET. Thus, the improvement of transport models certainly remains a key issue and a challenge for future developments.

VI. INTEGRATED PLASMA MODELING AT JET

VI.A. Introduction

Several experimental results in JET and other devices in the 1990s indicated the necessity to develop transport tools that allow an integrated modeling of the entire plasma, from the SOL to the center, covering a wide range of phenomena usually not properly linked in 1-D transport codes. In the first instance, this is related to the modeling of H-mode plasmas, which develop a thin layer of plasma with a reduced level of turbulence (the so-called ETB) near the separatrix to separate the hot core plasma from the SOL. In fact, the ETB cannot simply separate the core from the edge: Its mere existence strongly depends on the plasma parameters on both sides of the barrier. The resultant plasma is a complex self-organized medium, for which the global characteristics strongly depend on both core and SOL. Another example of this integral behavior is contamination of plasma by external impurities. Impurities (apart from He ash) always originate in the SOL, but they can penetrate through the ETB and contaminate the plasma core.

At JET the development of an integrated model in the 1990s was followed along two related, but to some extent independent, lines. On one side, essentially empirical models were developed and carefully calibrated against experimental results, using the codes JETTO (core energy and hydrogen isotopes transport),[43] SANCO (core impurity transport),[208] and EDGE2D (2-D energy and particle transport in the boundary region, including the SOL with plasma-wall interactions).[209] On the other side a new tool was developed by linking these codes into a single code starting with JETTO and EDGE2D (Ref. 210) and extending the link to SANCO first with one impurity species[77] and then with two impurity species.[211] This tool, called COCONUT (Combined Codes Numerical Utility for Tokamaks) also maintains the interfaces of the component codes with the JET experimental databases, a very useful ingredient for validating models at JET.

The numerical splitting technique adopted to link the core and boundary codes has proved to be very robust, allowing us to deal with very different timescales such as those required to study the effect of an ELM crash in the boundary and SOL regions and transport in the core region.

The structure of COCONUT is such that transport models for energy, hydrogen isotopes, and impurities can be developed and tested using independent components. An integrated model is then tested only in discharges for which a sufficiently complete set of experimental results for the plasma core and the plasma boundary region exists.

The main effort in developing transport models at JET in the period 1995 to 1999 has been dedicated to the so-called Bohm–gyro-Bohm model.[13] This is an empirical model for energy transport that has been tested extensively on JET discharges as well as in discharges available in the ITER profile database.[212] It includes nonlocal features, allowing the simulation of various kinds of heat pulses in JET L- and H-modes.[10] The model also allows for the formation of a neoclassical transport barrier just inside the separatrix for H-modes and the formation of ITBs (Ref. 213). A simple model for type-I ELMs is also included, assuming that an ELM crash takes place when the pressure gradient within the H-mode barrier exceeds the ballooning stability limit.[214]

Hydrogen isotope transport was simply related to the energy transport via the simple assumption $D \propto \chi_e$, with or without an inward pinch velocity v. A similar D and v transport model was normally used for impurity transport in the plasma core, with D and v spatially shaped to simulate the experimentally determined distribution of impurities.

Perpendicular transport in EDGE2D, in line with other 2-D edge codes, was usually represented by constant transport coefficients and pinch velocity. On the other hand, parallel transport for energy and particles was derived on the basis of the classical 21-moment Grad approach and includes drift terms and heat flux limiters for plasmas with long mean-free-path in the SOL (Ref. 215).

The transport model briefly described above and the COCONUT code have been used to study the following:

1. the plasma evolution following the L-H transition in hot-ion H-modes

2. type-I ELMs and, in particular, the role of the ELM's frequency on the plasma performance and its possible link to the H-mode transport barrier width

3. the evolution of the total particle content in JET ELMy H-modes and its possible relation to plasma-wall interactions and pumping in the JET divertor

4. neon puffs in JET L-mode discharges

5. helium exhaust in JET ELMy H-modes and ITER.

Although the largely empirical nature of the models suggests caution in the interpretation of these simulations, several generic results on the possible influence of the plasma boundary region on the overall plasma performance have been clearly pointed out, providing a very useful guidance for the understanding of JET experimental results.

Predictive modeling at JET after 1999 underwent considerable changes. First of all, arrival of modelers from other European Union associations brought new ideas, new theory-based transport models, and new codes. Second, the number of users of JET-based transport codes increased from a dozen to more than a hundred. These changes initiated reorganization of the code support and integration of available codes into JET Analysis Cluster (JAC). New theory-based transport models[39,41] were introduced in all available core transport codes. These models were used to simulate "state-of-the-art" scenarios such as optimized shear, hybrid, ELMy H-mode with type-II ELMs, and others. A detailed simulation of the heat pulse induced by ELM in the SOL has been done using either a stand-alone 2-D transport code or the linked core-edge code COCONUT (Refs. 216, 217, and 218). Simultaneously, the system of interconnected, user-friendly codes linked with JET and ITPA profile databases has been developed, which made transport and MHD codes an easy-to-use instrument, available to a large number of users from all associations.

The rest of the section is organized as follows: Early attempts to simulate high-performance JET plasma such as hot-ion H-mode and optimized shear plasma are reviewed in Sec. VI.B. Section VI.C is devoted to a modeling of ELMy H-mode, including development of theory-motivated ELM model with a self-consistent analysis of MHD stability. Section VI.D summarizes modeling of the penetration of impurities from the SOL to the core. An overview of the application of theory-based transport models to study the formation of ITBs is given in Sec. VI.E. Finally, Sec. V.F summarizes recent progress in code benchmarking.

VI.B. Early Modeling of Hot-Ion H-Mode and Optimized Shear Scenario

The development of an empirical transport model for high-performance JET plasma started in the early 1990s, when it was realized that experimentally observed confinement for L-mode plasma scales as Bohm rather than gyro-Bohm with respect to the ion Larmor radius. This led to the development of the so-called mixed Bohm–gyro-Bohm transport model,[13,219] summarized in Eqs. (3), (4), and (5). The model reproduced quite well JET L-mode plasmas. The next challenge came from experiments with externally triggered transient phenomena, such as cooling the plasma edge by sudden ablation of a metal impurity at the plasma edge, fast L-H transition, or ELMs. These experiments have shown[220] that a sudden change of electron temperature near the separatrix propagates deep into the plasma core within a characteristic time that is much shorter than the diffusive time. This fast-pulse propagation was associated with the nonlocal inward turbulence propagation, a theme that is getting more and more popular nowadays.[48] At the time of the first publications from JET, this turbulence nonlocality was implemented in a very simplistic form, in which the Bohm term scaled inversely proportionally to the edge electron temperature gradient length,[13,221] as in Eq. (6).

The transport model in Eqs. (4), (5), and (6) has been successfully used to simulate a number of fast-propagating heat pulses observed at JET. Figure 46 shows one example of such simulations for shot 31327 ($I_p = 2.5$ MA, $B_T = 2.8$ T, and $P_{NBI} = 8$ MW), from Ref. 13, in which a cold pulse, triggered by laser ablation, is followed by an L-H transition.

It was quickly realized that the same model can be applied to an H-mode plasma if the following modifications are implemented:

1. All transport coefficients are reduced to the level of ion neoclassical thermal conductivity within the narrow region near the separatrix to reproduce the formation of an ETB.
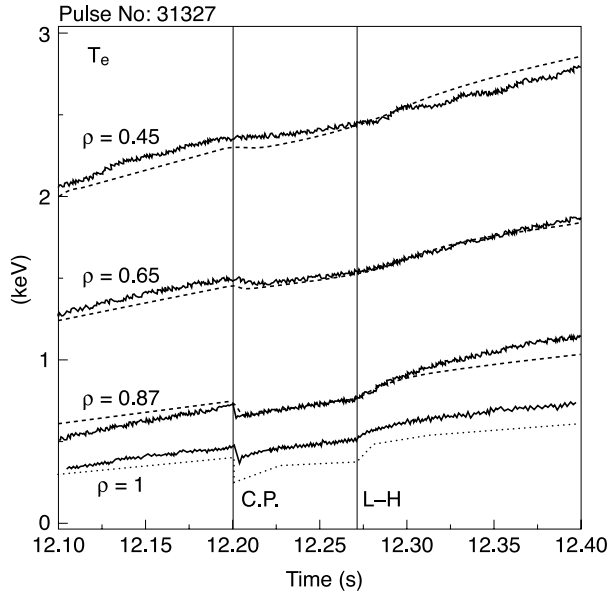
Fig. 46. Comparison of the experimental (solid lines) and computed (dashed lines) electron temperature evolution at different radial positions throughout the cold pulse (at $t = 12.2$ s) and the L-H transition (at $t = 12.27$ s) for shot 31327 ($B_T = 2.8$ T, $I_P = 2.5$ MA, and 2×10^{19} m^{-3} < n_e < 3×10^{19} m^{-3}). The dotted line indicates the prescribed boundary condition.

Fig. 47. Time traces of the main plasma parameters for 40305 ($I_P = 3.8$ MA and $B_T = 3.45$ T), measured and computed (reproduced from Ref. 213).

2. The nonlocal multiplier in the Bohm term $(T_{e(\rho=0.8)} - T_{e(\rho=1)})/T_{e(\rho=1)}$ in the H-mode takes the electron temperature at the top of the ETB instead of the separatrix. This makes the model independent of boundary conditions, with the caveat that it does not provide timing for the L-H transition.

The transport model assumes that the L-H transition leads to the formation of a transport barrier just inside the separatrix with the characteristic width $\Delta \propto \sqrt{a \times \rho_{\theta i}}$ and that transport within the barrier is of the order of ion neoclassical thermal conductivity: $\chi_e \approx \chi_i \approx D \approx \chi_i^{neo-cl}$. Such an extended model has been applied to simulate time evolution of the high-performance ELM-free hot-ion H-mode.[213,222] Figures 47 and 48 show the result of the predictive modeling of one of the best JET hot-ion H-mode shots, 40305 ($I_P = 3.8$ MA and $B_T = 3.45$ T), with the model described above. We can conclude that the proposed model reproduces quite satisfactorily both the time evolution and the main profiles. The model also shows that both neoclassical losses through the transport barrier and charge-exchange losses evolve in a similar way and play an equally important role in the energy balance. Analysis indicates that the system has three different limitations: the ballooning stability limit within the ETB, the external kink stability limit, and saturation of plasma confinement due to the density rise. Usually (with the possible exception of when there is a very small
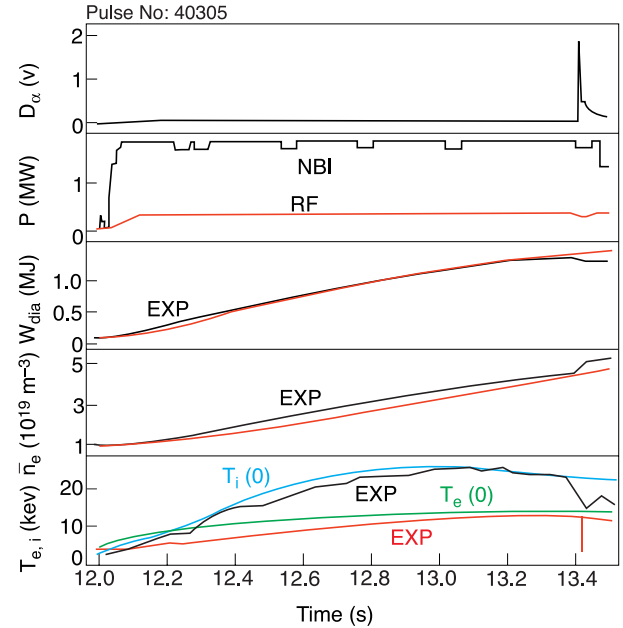
heating power), the plasma exceeds the one or the other MHD stability limit long before it reaches saturation in confinement. Therefore, ELMs and "roll-over" phenomena pose an important limitation to plasma performance in this regime.

It is important to emphasize that a key feature of the hot-ion H-mode lies in its ETB, which controls the energy losses through the separatrix. It has been observed in experiment that the confinement, normalized to ELM-free H-mode scaling prediction (ITER-93-H), rises approximately linearly with time during the ELM-free phase, reaching a factor of ~1.8 at the end of the ELM-free phase. This exceptionally high confinement was partly attributed to a low level of transport within the ETB (low edge density), partly to a good MHD stability, and partly to a very wide edge barrier. It was suggested in Ref. 223 that the ETB width is controlled by the fast ion Larmor radius in hot-ion H-mode with very strong NBI heating. Different models for ETB width have been tested in predictive modeling with transport barrier width scaling as fast-ion Larmor radius, giving better agreement with hot-ion H-mode experiment.

An optimized shear scenario was another type of high-performance JET plasma, which was used during the D-T campaign in 1997. The main advantage of this scenario is that because of intense plasma heating during the current ramp-up phase, plasma develops a region with a flat or even inverted q profile in the central part of the plasma volume.[224] This nonmonotonic q profile, combined with a strong shear in plasma rotation, induced
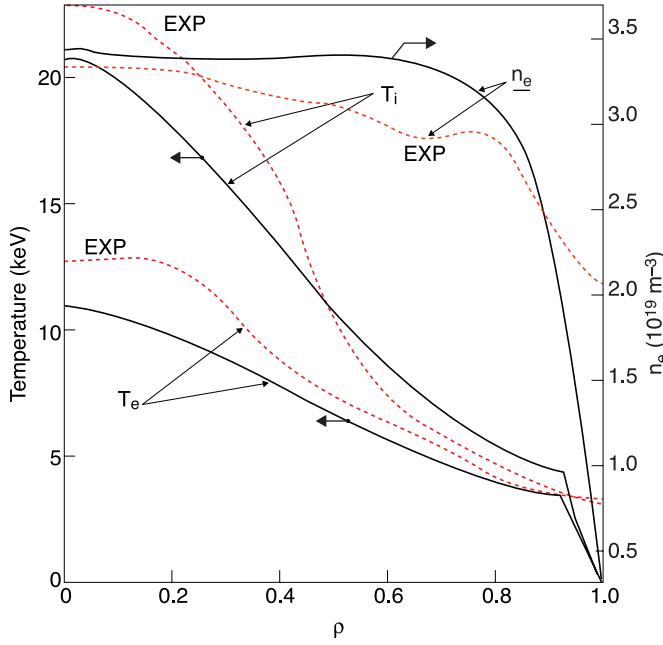
Fig. 48. Comparison of the main measured and computed profiles for 40305 ($I_P = 3.8$ MA, $B_T = 3.45$ T), at $t = 13.0$ s (reproduced from Ref. 213).

the shearing rate is not the only mechanism of turbulence suppression that plays a role in the formation of the ITB. We should also take into account a mechanism of turbulence stabilization (or moderation) by negative or zero magnetic shear.[150,226] Long-wavelength turbulence, which is responsible for the Bohm type of transport, should be particularly sensitive to this mechanism. Since the two above-mentioned mechanisms could work together, we multiplied the Bohm coefficient in Eq. (15) by a step function, which depends on a combination of two control parameters, ζ_1 and ζ_2. The gyro-Bohm term, which represents short-wavelength turbulence, should be less affected by shear in plasma rotation and was left unchanged.

$$\chi_B = \left| \frac{\nabla n T_e}{nB} \right| q^2 \left| \frac{\nabla T_e}{T_e} \right|_{r \approx a} H(\zeta_1 + s - \zeta_2 \Omega) \ . \quad (23)$$

Figures 49 and 50 show the time evolution of the main plasma parameters for a typical ITB pulse 39515 ($I_P = 3.0$ MA and $B_T = 3.45$ T) together with the results of the modeling using the most successful model (a global ITB, which is produced by a combination of magnetic shear plus strong shear in plasma rotation with

mainly by coinjected NBI, generates a strong ITB. Often this ITB evolves in time, usually expanding during the current ramp-up phase. Its further evolution is controlled by the formation of the ETB and by the amplitude of emerging ELMs: strong type-I ELMs lead to gradual erosion, and sometimes to a complete disappearance, of the ITB. To simulate the dynamics of ITB formation and evolution, the Bohm–gyro-Bohm transport model described above has been modified as follows[188]: First of all, it was assumed that long-wavelength turbulence, responsible for the Bohm term in Eq. (15), could be stabilized by a strong shear in the plasma rotation, broadly in accordance with an original idea from Refs. 153 and 225. A dimensionless parameter Ω was introduced[154]:

$$\Omega \equiv \frac{\omega_{E \times B}}{\gamma}$$

$$\propto \frac{R \left| \frac{(RB_p)^2}{B} \frac{\partial}{\partial \psi} \left[\left(\frac{\nabla n_i T_i}{e n_i} - v_\theta B_T + v_\phi B_p \right) \frac{1}{RB_p} \right] \right|}{v_{th,i}} \ ,$$

$$(22)$$

where the poloidal flux $\psi \equiv \int RB_p \, dr$ and $v_{th,i}$ is ion thermal velocity. We might expect that plasma turbulence (the one with long wavelength in particular) is suppressed if the parameter Ω exceeds a certain value, say, $\Omega \geq \delta = O(1)$. Analysis of JET experiments shows that
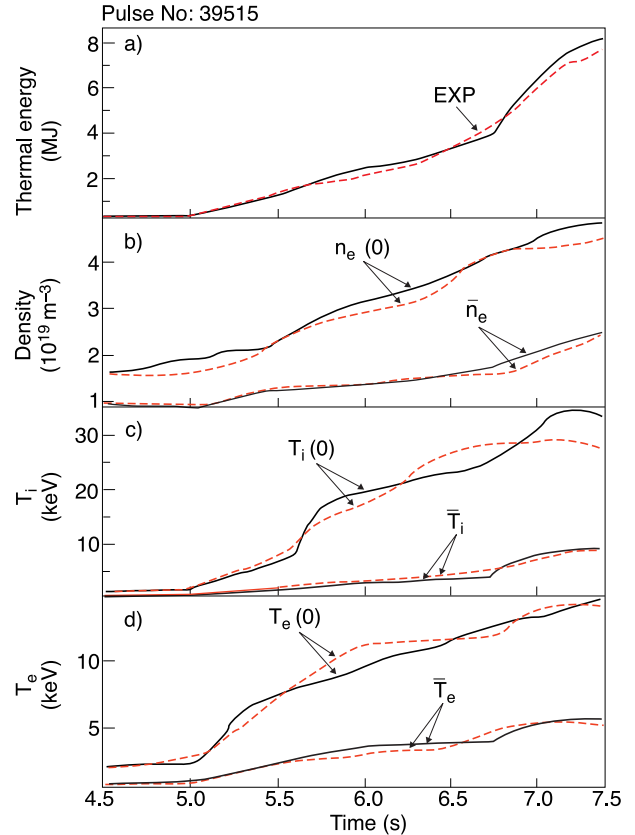

Fig. 49. Measured and computed time traces for optimized shear shot 39515 ($I_P = 3.0$ MA and $B_T = 3.45$ T; reproduced from Ref. 188).
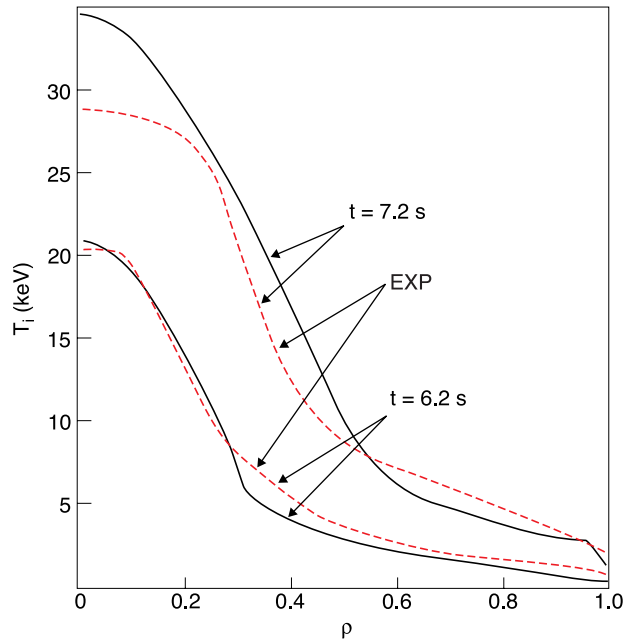
Fig. 50. Measured and computed ion temperature profiles for optimized shear shot 39515 (I_P = 3.0 MA and B_T = 3.45 T; reproduced from Ref. 188).

ζ_1 = 0.1 and ζ_2 = 1.2). Formation, expansion, and the transition to ELM-free H-mode followed by the collapse of the ITB are well reproduced by the model. It is interesting to note that the model manages to reproduce not only the transition to an improved core confinement but also the erosion and subsequent disappearance of the ITB shortly after the L-H transition. It was not necessary to include the effect of additional MHD activity (such as ELMs), although MHD is thought to play a role in some discharges.

VI.C. Modeling of ELMy H-Mode

Modeling of ELMy H-mode is a good example of an integrated approach since the relevant physics involves both the plasma core and the SOL. First of all, the dynamic models have been developed and used in the JETTO code[227] for the formation of the pedestal and the effect of ELMs in H-mode discharges. In this model, all the channels of transport through the pedestal are reduced to the neoclassical ion thermal diffusivity computed at the top (inner edge) of the pedestal. The width of the pedestal is computed using a scaling with the ion Larmor radius. An ELM crash is triggered when either a pressure-driven ballooning mode or a current-driven peeling mode becomes unstable anywhere within the pedestal. The MHD stability criteria that are used to trigger ELM crashes are calibrated for each simulation using the MHD stability code MISHKA (Ref. 228). The ELM crash is simulated by using a 300-fold enhancement of thermal transport

and a 100-fold enhancement of particle transport for a fraction of a millisecond.

This heuristic pedestal and ELM model has been used in the JETTO code to simulate ELMy H-mode JET plasmas with a wide range of plasma parameters. These include a series of discharges with type-I, type-II, and type-III ELMs, which constitute scans in density, ρ^*, and isotope mass, and many others. First of all, the sensitivity of the ELM model with respect to ELM amplitude and duration was tested. These simulations showed that although the ELM frequency does depend on the ELM amplitude (actually, the ELM frequency depends on the product of the ELM amplitude and its duration), the time average confinement time is insensitive to these variations.[218,227] Then it was shown[229] that in plasmas with type-I ELMs, in which the ELM frequency increases with the heating power, the MHD stability of the edge barrier is controlled by a ballooning mode. Later on it was demonstrated that the pedestal temperature rather than the ELM frequency might increase with increasing heating power, as observed in some JET experiments.[230] This trend was explained by the interplay between peeling and ballooning stability. It was also demonstrated that there is a transition from first to second stability as the triangular shape of the plasma is increased.[231] The width and height of the pedestal were shown to increase as the hydrogenic isotope mass is increased.[232] These three effects are shown to enhance the predicted performance of ITER in simulations using the JETTO code.[233] Simulations of JET discharges have shown that either a pressure-driven ballooning mode or a current-driven peeling mode[234] can trigger ELM crashes.

A variation of the basic JETTO model described above has been used to simulate type-I and type-II ELMs in JET discharges.[235] An analytic linear ballooning/peeling mode model has been used to simulate the growth and width of type-I or type-II ELMs using JETTO (Refs. 236 and 237). The effect of gas puffing on ELM behavior was simulated by coupling the JETTO code with the 2-D EDGE2D and COCONUT codes.[238] Traditionally, the plasma core, the ETB, and the SOL regions have been treated separately in predictive modeling, with the motivation that the physics governing transport in these regions is different. Modeling the different plasma regions separately is, however, not self-consistent, because it has become increasingly evident that there is a strong link between the core, pedestal, and SOL so that even a modest variation of the plasma parameters in one region can lead to a dramatic change in overall plasma performance. A good example of such a link, which involves the core, ETB, and SOL, is the effect of external neutral gas puffing in type-I ELMy H-mode plasma, which has been modeled at JET (Ref. 237) using the suite of integrated modeling code COCONUT and linear ideal MHD stability code MISHKA-1. It should be noted that the coupling scheme of the integrated transport code COCONUT makes it possible to self-consistently model the entire plasma

and thereby accurately take into account the strong interaction of the SOL, ETB, and core.

It is well known from experiments that the plasma easily accommodates modest gas puffing (a neutral influx of the order of $\Gamma = 3 \times 10^{22}$ s^{-1} in the case of JET). Higher levels of gas puffing cause a transition to type-III ELMs, i.e., a dramatic increase in ELM frequency followed by the deterioration of plasma confinement. Integrated predictive modeling reveals a chain of causalities that might explain the experimentally observed behavior. An increase in neutral gas puffing initially affects the SOL, something that quickly translates into increased density and reduced ion and electron temperature at the separatrix and beyond it. The evolution of the density and temperature has been modeled for various levels of external neutral gas fueling using COCONUT. With the integrated code, it is possible to self-consistently model the penetration of the neutrals and predict the plasma profiles. Figure 51 illustrates the results of the COCONUT simulations. Shown in the figure are the ion density and ion temperature profiles in a region extending from the SOL to beyond the top of the ETB for six different levels of gas puffing ranging from $\Gamma = 0$ to $\Gamma = 1 \times 10^{23}$ s^{-1}.

The one-and-a-half-dimensional JETTO transport code has been used to further explore the chain of causalities resulting from an increase in external neutral gas puffing, making use of the COCONUT results. Specifically, the boundary conditions in the JETTO modeling have been determined from the plasma profiles calculated self-consistently by COCONUT. As a result of the higher density, the collisionality within the pedestal increases with the gas puffing. The bootstrap current, which scales as $1/(1 + \nu)$, with ν being the collisionality, decreases as a consequence of the higher collisionality. Because of this, the total current, which comprises both bootstrap and ohmic current, also decreases within the pedestal. The decrease in the edge current leads to an increase in magnetic shear, which can cause the plasma to lose access to the second ballooning stability region.

Situations with different levels of neutral gas puffing have been analyzed with the MISHKA-1 MHD stability code. A characteristic result of the analysis is illustrated in Fig. 52, which shows MHD stability diagrams for two different levels of neutral gas puffing. The analysis demonstrates that increasing neutral gas puffing can trigger a transition from second- to first-ballooning stability. In the first-ballooning stability region, infinite-n ballooning instabilities limit the achievable pressure gradient. As a consequence, a much smaller pressure gradient can be sustained there than in the second-ballooning stability region, where typically medium-n ballooning modes determine the achievable pressure gradient.

The reduction of the sustainable pressure gradient due to an increase in the level of neutral gas puffing has been fed back as an adjustment into the relevant JETTO simulations. As expected, such an adjustment leads to a lower pressure at the top of the pedestal and a dramatic increase in the ELM frequency. Because of profile stiffness, the lower pressure at the top of the pedestal translates into lower pressure throughout the core plasma and thus into lower overall confinement.

It should be noted that, in a sense, the edge current plays a dual role in the MHD stability of the pedestal. In
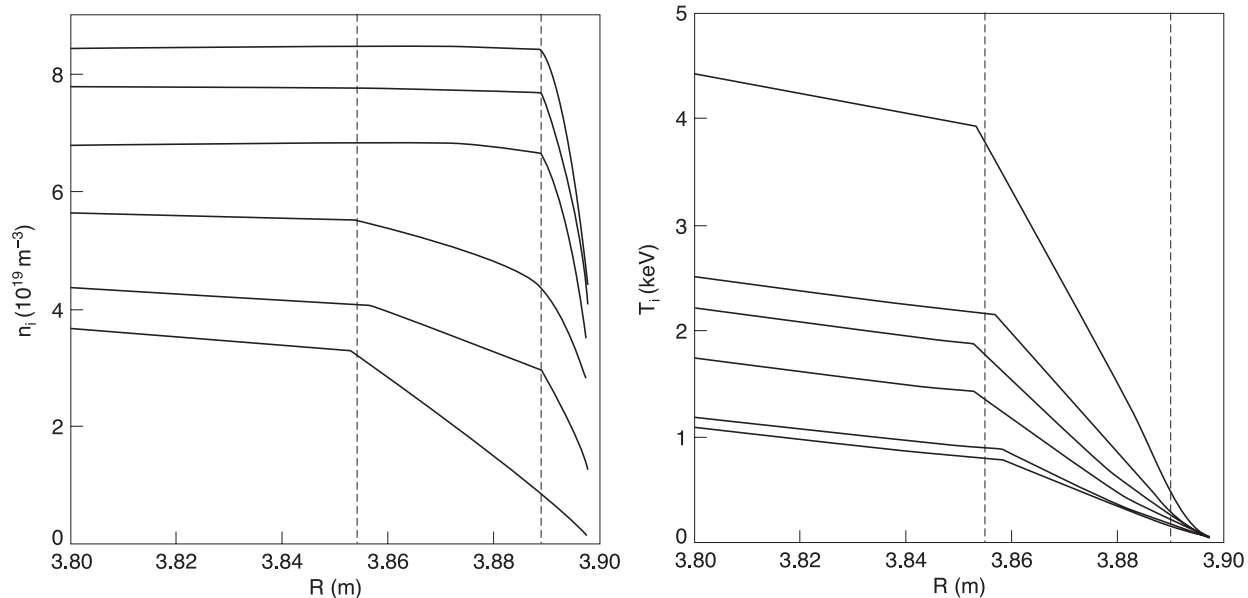

Fig. 51. Ion density and ion temperature profiles in a region extending from the SOL to beyond the top of the ETB for six COCONUT simulations with different levels of gas puffing ranging from $\Gamma = 0$ to $\Gamma = 1 \times 10^{23}$ s^{-1}.
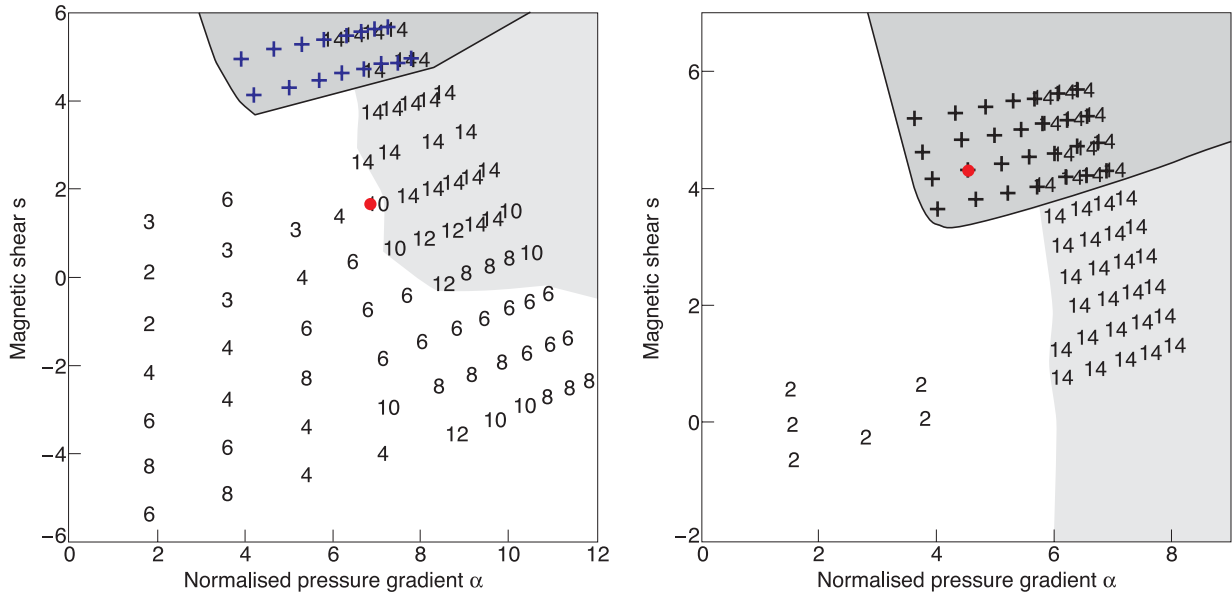
Fig. 52. MHD stability diagrams with the normalized pressure gradient on the horizontal axis and magnetic shear on the vertical axis for two different levels of neutral gas puffing: $\Gamma = 0$ (left) and $\Gamma = 1 \times 10^{23}$ s^{-1} (right). Shown in the figure are the mode numbers of the most unstable peeling and ballooning modes as well as infinite n ballooning instabilities (marked with crosses) and the operation point (marked with a large dot).

addition to changing the ballooning stability indirectly by affecting the magnetic shear, the edge current may also directly destabilize peeling modes and hence cause ELMs.

Based on the chain of causalities discussed above, it has been proposed that the transition from type-I to type-III ELMy H-mode with increasing neutral gas fueling might be explained as a transition from second to first ballooning stability. This demonstrates how sensitively the SOL, ETB, and core are linked together and how they interplay. It is worth noting here that the proposed model obviously contradicts the original idea that type-III ELMs are controlled by a resistive rather than an ideal ballooning mode and is therefore somewhat controversial. On the other hand, the proposed model does not defy the importance of resistivity in ballooning stability but rather point toward the necessity of using a mechanism of sharp change in the level of critical pressure gradient to explain experimental observation. The original idea was not able to explain the experimentally observed sharp transition from one type of ELM to another.

In the simulations presented above, ad hoc assumptions about ELM amplitude and duration were used. This does not allow realistic modeling of an ELM cycle. A more sophisticated theory-motivated model for the evolution of the amplitude of the unstable MHD mode has been developed in Ref. 236. The model couples transport equations in JETTO with linearized equations for the amplitudes of ballooning and peeling modes, which might be destabilized within the edge barrier by

either excessive pressure gradient or current. Separate equations were used for the ballooning and peeling mode amplitudes ξ_b and ξ_p, respectively, whereupon the individual mode amplitudes are added to give a total mode amplitude ξ:

$$\frac{d\xi_b}{dt} = C_b \gamma_b \left(1 - \frac{\alpha_c}{\alpha}\right) H(\alpha - \alpha_c)\xi_b - C_d \frac{c_s}{R}(\xi_b - \xi_0) \ ,$$

(24)

$$\frac{d\xi_p}{dt} = C_p \gamma_p \left(1 - \frac{J_c}{J}\right) H(J - J_c)\xi_p - C_d \frac{c_s}{R}(\xi_p - \xi_0) \ ,$$

(25)

and

$$\xi = \xi_b + \xi_p \ .$$

Here, γ_b is the ballooning mode growth rate, $\gamma_b = c_s/\sqrt{RL_p}$ and, for simplicity, $\gamma_p = \gamma_b$ for the peeling mode growth rate. $C_b \sim 1$, $C_p \sim 1$, and $C_d \sim 0.1$ are constants characterizing the growth rate of the ballooning and peeling mode instabilities, the decay rate of the mode due to nonideal MHD effects, and the level of background fluctuations, respectively. H is the Heaviside function defined as $H(x) = 0$ if $x < 0$ and $H(x) = 1$ if $x \geq 0$, with x being an arbitrary variable, and $c_s = \sqrt{T_e/M_i}$ is the sound speed, where T_e is the electron temperature and M_i is the ion mass. L_p is the pressure scale length, R

is the major radius, and $\alpha = -(2\mu_0 r^2/B_p)(dp/d\psi)/0.64$ is the normalized pressure gradient, where r is the minor radius, B_p is the poloidal magnetic field, and ψ is the poloidal flux co-ordinate; α_c is the critical normalized pressure gradient.

In the pure ballooning model, the stability threshold has been described by a fixed critical pressure gradient, which can be a reasonable approximation in certain circumstances. Similarly, one could use a fixed critical current as the stability threshold in a pure peeling model as a first approximation. However, Ref. 239 proposes a more general localized peeling stability criterion based on the MHD energy principle. By denoting

$$ J = 1 + \frac{1}{\pi q'} \oint \frac{j_\parallel B}{R^2 B_p^3}\, dl - \Delta_v $$

and

$$ J_c = \sqrt{1 - 4D_M}\ , \tag{26} $$

the condition for peeling stability can be expressed as $J < J_c$. Here, D_M is the Mercier index,[240,241] which is proportional to the pressure gradient ∇p, q' is the gradient of the safety factor, $j_\parallel$ is the current density parallel to the magnetic field, B is the magnetic field strength, and Δ_v is a vacuum energy parameter describing the distance from the external surface to the plasma surface.

At each time step, the plasma parameters calculated by JETTO were used to evaluate the mode amplitude ξ given by Eqs. (24), (25), and (26), and the calculated perturbation amplitude determines the level by which transport is enhanced. More specifically, Gaussian-shaped perturbations having amplitudes proportional to the calculated perturbation amplitude ξ are added on top of the radial profiles of the transport coefficients within the ETB and its vicinity. The additional transport perturbations $\delta\chi$ representing ELMs can thus be written as

$$ \delta\chi(r,t) \sim \xi(t)\exp\left[-\left(\frac{r - r_0}{\Delta}\right)^2\right]\ , \tag{27} $$

where r_0 is the radial location of the center of the Gaussian and Δ is the characteristic width of the Gaussian. The use of Gaussian-shaped ELMs is motivated by the fact that the ballooning modes assumed to drive the ELMs have Gaussian shapes in linear theory.

The theory-motivated ELM model with separate equations for the ballooning and peeling mode amplitudes given by Eqs. (24) and (25) is capable of qualitatively reproducing the main features of type-I ELMy H-mode when coupled to a JETTO transport simulation. With a choice of simulation parameters consistent with actual experimental parameters, simulations with this model produce strong periodic oscillations distinctly resembling type-I ELMs with a repetition frequency that increases with the external heating power. This is illustrated in

frames Figs. 53a, 53b, and 53c which show time traces of the ion thermal conductivity at the magnetic surface $\rho = 0.92$ in three predictive transport simulations with different levels of neutral beam heating power, namely 8, 16, and 24 MW. The plots are qualitatively similar to time traces of the D_α signal in type ELMy H-mode discharges. As in type-I ELM experiments, the ELM frequency slowly increases with the heating power.

VI.D. Penetration of Impurities from the SOL to the Core

Predictive modelling of impurity accumulation in the plasma core is another interesting example of the importance of the integrated approach in predictive modelling. Since impurities (apart from He ash) originate in the SOL, both SOL and ETB control their penetration to the core. Experimentally extrinsic impurities (like, N, Ne, Ar) were used at JET to mitigate ELMs. Impurities like Ar and Ne that have high recycling rates can create a poloidally and toroidally uniform mantle near the separatrix in order to increase evenly the radiation and reduce the power flux through the separatrix both during and between ELMs. This should reduce the power load on the divertor target plate as well as reduce ELM amplitude and frequency. With high triangularity, the plasma manages to stay in type-I ELMy H-mode even during a continuous deuterium gas puffing and "blips" of impurity puffing without noticeable degradation in plasma confinement with the reduced ELM frequency and amplitude.[108,242,243] Simultaneously these experiments have shown that the level of the main gas puffing should be kept above a certain level, below which impurities start to accumulate in the core and eventually cause a radiative collapse even in the presence of regular type-I ELMs. Figure 54 shows some examples of this phenomenon.

It was realized[101] that impurities are prevented from accumulating in the core not as much by ELMs but mostly by particle transport within the edge barrier. All available transport codes, starting from core code JETTO/SANCO and finishing with core-edge coupling code COCONUT, were used to simulate impurity penetration through the ETB. Since transport within the ETB is considered to be close to the neoclassical level, a full matrix of the neoclassical transport coefficients for impurities and the main ions was taken from NCLASS. The neoclassical convective particle velocity is probably the most important part of this matrix since it is believed to be responsible for impurity accumulation in the plasma core. Generally, the neoclassical flux not including the Ware pinch can be written in the following form[244]:

$$ \Gamma_z^{neo} = \frac{D}{2Z}\left[K\left(\frac{1}{n_i}\frac{dn_i}{dr} - \frac{1}{Zn_z}\frac{dn_Z}{dr}\right) + \frac{H}{T_i}\frac{dT_i}{dr}\right]\ , \tag{28} $$
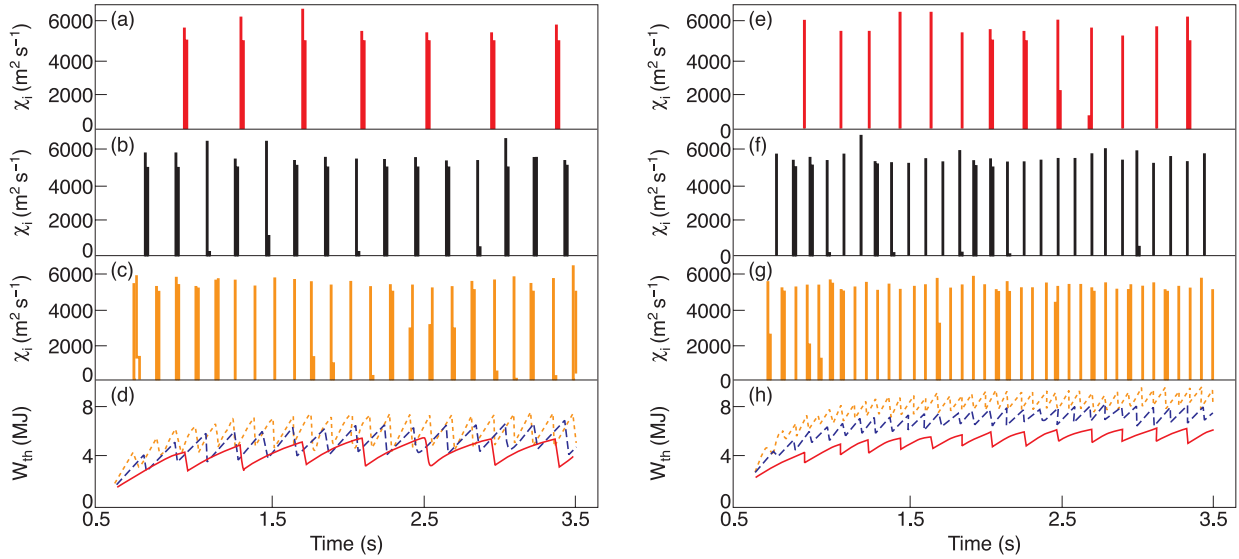
Fig. 53. Simulations with the combined ballooning-peeling ELM model with separate equations for the ballooning and peeling mode amplitudes [Eqs. (24) and (25)]. Ion thermal conductivity as a function of time in three mutually similar simulations with different levels of neutral beam heating power $P_{\rm NBI}$: (a) 8, (b) 16, and (c) 24 MW. The boundary condition $T_{sep} = 25$ eV is used for the ion and electron temperatures at the separatrix. Neoclassical resistivity is not enhanced during the ELMs. (d) Thermal energy content of the plasma as a function of time in the simulations used in frames (a) (long-dashed curve), (b) (short-dashed curve), and (c) (dotted curve). Ion thermal conductivity as a function of time in another series of simulations with different levels of neutral beam heating power $P_{\rm NBI}$: (e) 8, (f) 16, and (g) 24 MW. The boundary condition $T_{sep} = 100$ eV is used for the ion and electron temperatures at the separatrix and neoclassical resistivity is enhanced during the ELMs. Otherwise, the simulation parameters are the same as in the simulations used in frames (a), (b), and (c). (h) Thermal energy content of the plasma as a function of time in the simulations used in frames (e) (long-dashed curve), (f) (short-dashed curve), and (g) (dotted curve).
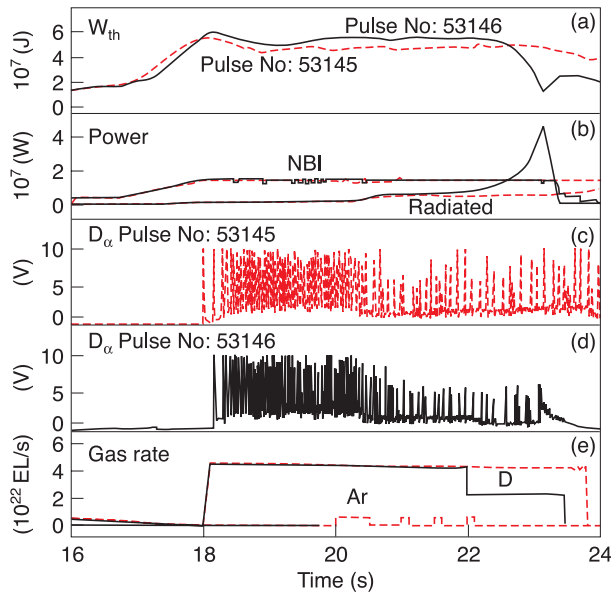

Fig. 54. (a) Energy content, (b) heating power and radiated power, (c) and (d) D_α signal, and (e) gas puffing rate for shots 53145 (red dashed) and 53146 (blue solid) ($I_P = 2.3$ MA, $B_T = 2.4$ T, and $n_e \sim 1 \times 10^{20}$ m^{-3} in both shots). (Color online)

where

$$n_z = \text{impurity density}$$

$$n_i = \text{density of the main ions}$$

$$Z = \text{charge of the impurity}$$

$$D \propto n_z = \text{neoclassical diffusion coefficient}$$

K and H are functions of dimensionless plasma parameters, including ion collisionality (see Ref. 87). Theory predicts that the coefficient $K > 0$ so that the first term in the right-hand side of Eq. (28) causes an inward convective velocity for impurities if $dn_i/dr \leq 0$ for the whole range of collisionalities. The coefficient H, on the other hand, changes sign depending on the collisionality of both main and impurity ions. It follows from the neoclassical theory that usually $(H/K) \approx -0.5$ in JET ELMy H-mode plasmas so that the third term on the right-hand side of Eq. (28) evokes an outward convective velocity, or "screening" effect, if $dT_i/dr \leq 0$. The competition between these two terms determines the fate of impurities: they can be stopped at the edge when there is a relatively strong temperature gradient [if $(K/n_i)(d|n_i|/dr) \leq (|H|/T_i)(d|T_i|/dr)$] or they can
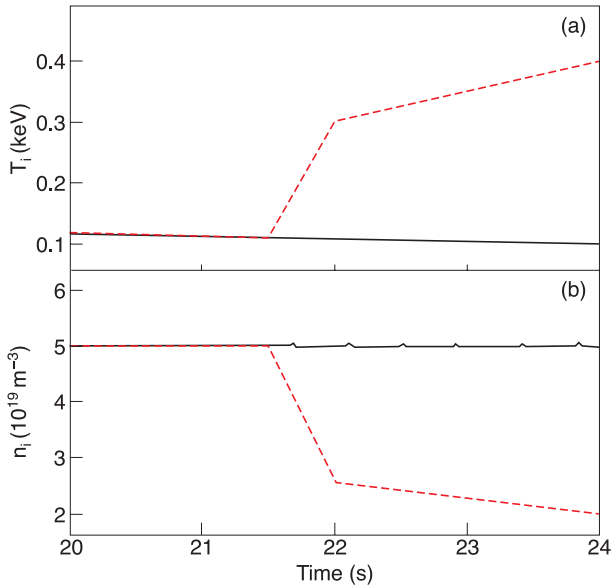
Fig. 55. Time evolutions of (a) edge ion temperature and (b) edge ion density for simulation with impurity.

Fig. 56. Time traces for the run with the same rate of impurity puffing but different boundary conditions: constant temperatures and density (blue) and rising temperature and falling density (red). (Color online)

Fig. 57. Radial distribution of the convective velocity density of the impurity before (blue solid) and after (red dashed) transition to a lower level of gas puffing. (Color online)

penetrate deep into the plasma core in the opposite case of a weak temperature gradient.

Two sets of boundary conditions were used in predictive modeling to prove the importance of the gas puffing in an attempt to avoid impurity accumulation in the core, shown in Fig. 55. We keep plasma parameters at the separatrix constant in the first case [with $T_e(\rho = 1) = T_i(\rho = 1) \approx 100$ eV and $n_i(\rho = 1) = 5 \times 10^{19}$ m^{-3}], which corresponds to a constant, high level of gas puffing. We then reduce edge density and increase edge temperature in the second run [with $T_e(\rho = 1) = T_i(\rho = 1)$ increasing in time from 100 to 400 eV and ion density decreasing from $n_i(\rho = 1) = 5 \times 10^{19}$ m^{-3} to $n_i(\rho = 1) = 2 \times 10^{19}$ m^{-3} at the end of the run] to simulate the decrease of the gas puff.

Figure 56 shows the main time traces for two simulations. The same level of impurity (Ar in our case) puffing was used in both runs. One can observe very similar initial evolutions of all main plasma parameters (because of the similarity in the boundary conditions at the initial stage of the simulations). Starting from $t = 21.5$ s, however, the edge density goes down and the edge temperature goes up [the "red dashed" case (color online)]. This gradual change in the boundary conditions causes a dramatic transformation in the behavior of impurities: They start to penetrate through the edge transport barrier and accumulate in the core. The reason for such transformation is the convective velocity for impurities, which changes sign from positive to negative within the edge barrier. Figure 57 shows the radial distribution of the convective velocity, averaged over all ionization stages, and the impurity density for two
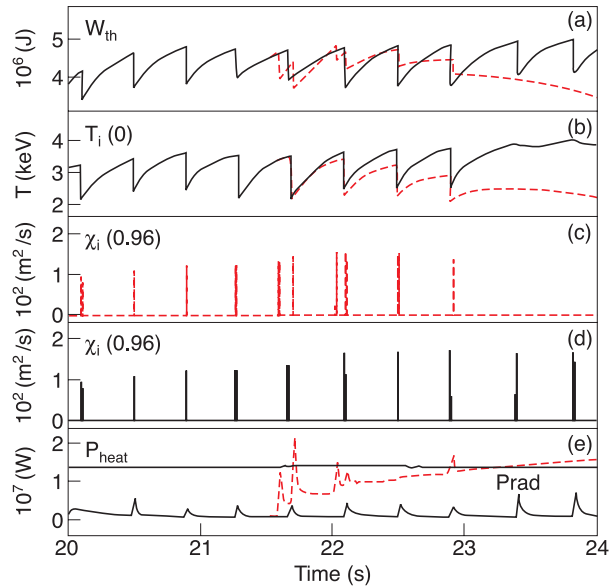
time slices, $t = 21$ and 23 s, for shot 53550. At 21.0 s the two runs have the same boundary conditions and both have the same positive convective velocity, leading to accumulation of impurities outside separatrix, in

the SOL. At $t = 23$ s after the step down in the edge density and step up in the edge temperature in the "red dashed" case (color online), the convective velocity for 53550 has a different, negative sign. This allows impurities to penetrate through the ETB and to accumulate deeper in the core, changing both the level and the pattern of the radiated power.

The ELM contribution to preventing impurity accumulation is not as important as either the deuterium gas puff or the outward convective velocity due to high ion temperature gradient and low main ion density gradient. The simulations were repeated with COCONUT, which allows self-consistent evolution of plasma parameters near the separatrix as a function of D puff. These simulations confirmed JETTO results.

VI.E. Modeling of Optimized Shear Plasmas: Role of Current Drive and Real-Time Profile Control

Tokamak plasma operation with weak or negative magnetic shear and with an ITB is regarded as one way to increase fusion performance. A hollow current density profile, i.e., a reversed q profile (negative magnetic shear), is one of the key conditions that gives rise to the improved core confinement and facilitates the formation of the ITB in advanced tokamak scenarios.[245]

There are several ways to modify the q profile in the preheating phase, i.e., to create the target q profile. The method to obtain a reversed q profile is in principle simple—either to drive off-axis cocurrent or on-axis countercurrent or alternatively to increase the electron temperature in order to slow down the current diffusion from the plasma edge to the center during the current ramp-up phase.

The current profile evolution during the preheating phase in JET has been calculated with the JETTO transport code assuming neoclassical electrical conductivity calculated with the neoclassical transport code NCLASS (Ref. 139) coupled to JETTO. The following preheating methods are considered and compared: ohmic, LHCD, on-axis and off-axis ICRH, and on-axis and off-axis NBI, as well as electron cyclotron current drive (ECCD). The basic principle used in this study is that the power deposition and external current density profiles are calculated in a self-consistent way. Consequently, the codes to calculate the power deposition profiles are coupled to JETTO to allow a self-consistent simulation cycle between the transport and power deposition (plus current density) calculation with time. This means that all the plasma profiles (such as T_e, T_i, n_e, q, B_p, B_T, I_p, Z_{eff}, etc.) are given as input from JETTO to the heating codes, and correspondingly, the heating codes return the power deposition and externally driven current density profiles back to JETTO. Coupled to JETTO at present are modules for the LHCD ray-tracing code FRTC (Ref. 246), an NBI code called PENCIL (Ref. 63), and the ECCD code
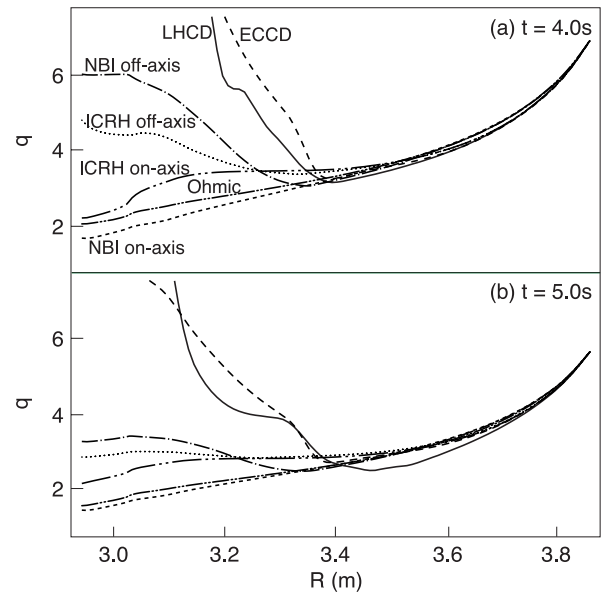

Fig. 58. Target q profiles at (a) $t = 4.0$ s and (b) $t = 5.0$ s simulated with different preheating methods (which all start at $t = 1$ s): LHCD (solid curve), ECCD (dashed curve), off-axis NBI (dashed-dotted curve), off-axis ICRH (dotted curve), on-axis NBI (short-dashed curve), on-axis ICRH (double long-dotted-dashed curve), and ohmic (double short-dotted-dashed curve) (reproduced from Ref. 249).

ECWGB (Ref. 247). The ICRH power deposition profiles have been calculated with PION (Ref. 248) outside JETTO.

The simulated target q profiles at $t = 4.0$ and 5.0 s produced by the different preheating methods are compared in Fig. 58. In the simulations, the main plasma parameters and the initial and boundary conditions for T_e are taken from pulse 51897 ($B_T = 3.45$ T, $I_P < 3$ MA, $P_{NBI} < 13$ MW, $P_{ICRH} = 4$ MW, and $P_{LH} = 2$ MW). The external heating power is 5 MW except in the case of LHCD, where the power is 3 MW. Thus, the simulations are identical except in terms of the heating and current drive methods.

As shown in Fig. 58, LHCD and ECCD are the only preheating methods that can produce deeply reversed q profiles. Quantitatively, the q profiles produced by LHCD and ECCD look quite similar. However, the central values of q are distinct. With LHCD, q tends to increase to very high values, such as $q_0 \approx 30$ to 50, whereas with ECCD, q_0 remains between 10 and 20. This difference comes mainly from the amount of driven off-axis current; LHCD current is of the order of 500 to 900 kA, whereas ECCD current is only 70 to 160 kA. Off-axis NBI and off-axis ICRH heating create weakly reversed q profiles with q_{min} located inside $R = 3.4$ m. Modeling predictions show that on-axis NBI, on-axis ICRH, and

ohmic preheating can create only monotonic target q profiles. The modeling results have been verified qualitatively in JET experiments with respect to LHCD, ICRH, and ohmic preheating.[249]

An important experimental program is in progress on JET to investigate plasma control schemes that could eventually enable ITER to sustain steady-state burning plasmas in an "advanced tokamak" operation scenario. The triggering and subsequent controllability of ITBs are major issues for fulfilling this goal, and their study is therefore an essential part of this program. Recently, a multivariable model-based technique was developed[158,159,250] for the simultaneous control of the current, temperature, and/or pressure profiles in JET ITB discharges, using LHCD together with NBI and ICRH. The RTC algorithms have been implemented in the JET control system, allowing the use of three actuators that are the power levels of NBI, ICRH, and LHCD systems. Algorithms identical to those used in the experiments have been also implemented in the JETTO transport code.[82]

A schematic illustration on how the open- and closed-loop RTC transport simulations are performed with JETTO is presented in Fig. 59. All the simulations start typically around $t = 4$ s (indicated by the vertical dashed-dotted line). The power step-ups in the open-loop simulations (such as the solid line) are made when the discharge is rather stationary, typically around $t = 15$ s, and the steady-state response, i.e., the calculation of the feedback controller matrix, is taken at around $t = 30$ s (dashed vertical line). In the closed-loop simulations, the RTC starts typically at $t = 5.5$ s (dashed vertical line), and RTC can be applied as long as desired, typically for more than one resistive current diffusion time. The power levels vary in the closed-loop simulations (dashed curve), as requested by the controller. The whole procedure of carrying out the open-loop power step-up simulations, determination of the controller matrix from the open-loop simulations, and finally performing the

closed-loop simulations with RTC is identical to that performed in JET experiments when applying the RTC technique. The benefits in the transport simulations with respect to experiments are that transport simulations are free from unpredictable events, such as MHD events, diagnostics problems, or power system failures, occurring often in the experiments and "polluting" the data. In addition, RTC techniques can be tested for several current diffusion times, which is impossible with the present capabilities of JET heating systems. Therefore, the simulations serve as a simplified platform to test, validate, and develop the RTC algorithms techniques, with increasing degrees of complexity and completeness.

Two closed-loop simulations with different setpoint profiles of q and $\rho^*_{T_e}$,

$$ \rho^*_{T_e} = -\frac{1}{Z_i} \sqrt{\frac{A_i m_p}{q_e}} \frac{1}{B_T} \sqrt{T_e} \frac{1}{B_T} \frac{\partial T_e}{\partial R} $$

[also see the definition in Eq. (20)] are compared to a reference open-loop simulation with constant power levels in Fig. 60. The setpoint profiles are a strongly reversed q and a strong ITB (large $\rho^*_{T_e}$), as illustrated in Fig. 60 by the dashed curves. The magnetic field, the plasma current, the plasma geometry, Z_{eff}, the initial and boundary conditions, and the power levels of LHCD, NBI, and ICRH, until the control starts, are taken from JET pulse 62527. Again, to assess the controller's effect on a fully developed steady state, the closed-loop simulations have been extended much farther in time than the experiment itself, which ended after $t = 9.2$ s.

The simulations with the combined RTC demonstrated that varieties of setpoint q profiles and $\rho^*_{T_e}$ profiles can be achieved and controlled simultaneously. Very important is that the successful control could be continued for several resistive current diffusion times. Therefore, within the limits of the present transport model, the simulation with the reversed q profile and strong ITB as the setpoint $\rho^*_{T_e}$
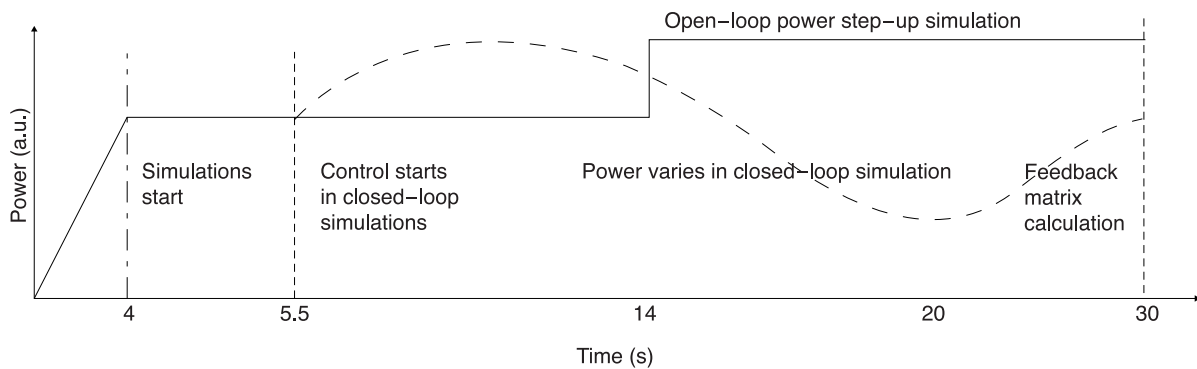

Fig. 59. A schematic view on how to perform open- and closed-loop transport simulations with JETTO. Times refer to typical times in JET ITB discharges, used in the predictive simulation (reproduced from Ref. 82).
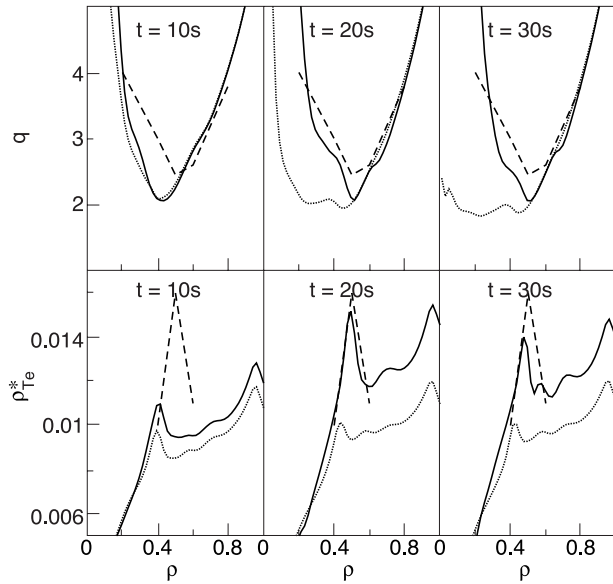
Fig. 60. The closed-loop simulation with a reversed setpoint q profile and strong ITB setpoint $\rho_{T_e}^*$ profile (solid curves). The setpoint q profile and $\rho_{T_e}^*$ profile are shown by the dashed curves and the reference open-loop simulation by the dotted curves (reproduced from Ref. 82).

profiles showed a way to achieve strong ion ITBs in a controllable way, desirable and necessary for high fusion performance in long-pulse experiments. These simulations also supported strongly the experimental results that the RTC of q and $\rho_{T_e}^*$ profiles can be carried out by using the RTC techniques presented in Refs. 158 and 250.

VI.F. Summary

Predictive transport modeling at JET always was an integral part of the JET project. However, if initially the number of modelers as well as available tools were very limited, after 2000 the number of users rose to about a hundred. Many predictive transport codes as well as postprocessing tools were bundled into a user-friendly suite of codes, which is available online from all European associations. Relative ease of code usage and proper organization of the catalog of modeling results, which allows users to look at other users' runs, led to a significant progress in the modeling activity at JET. Also, the JET-modeling community benefits strongly from the recent introduction of the JET Transport Task Force, which actually organizes and supervises the modeling activity at JET.

Last, but not least, the JET transport codes are being modified to be able to do predictive modeling of ITER scenarios. It is expected that JET tools will be actively used in preparation for ITER operation.

VII. OUTLOOK ON FUTURE DEVELOPMENTS OF CORE TRANSPORT WORK IN JET

The various sections of this paper have revised progress toward reaching a comprehensive understanding of turbulent transport in order that a validated theoretical tool becomes available for reliable extrapolation to predict transport in fusion reactor plasmas. It is clear that a systematic work of assessment of the existing theoretical tools, especially the most comprehensive gyrokinetic codes, against a wider set of well-characterized results from dedicated transport experiments or from large databases with high statistical weight is still needed to achieve this goal. Still, some basic physics understanding of the main mechanisms at play has been reached, which represents a true step forward with respect to our understanding of transport compared to, for example, 10 years ago. Moreover, such understanding is now addressing heat, particle, and momentum transport in a consistent approach.

With respect to the basic questions formulated in the introduction to this paper, we summarize in the following paragraphs the state of understanding and the main work needed to consolidate and complete the present views, with particular focus on what could be done on JET.

ITER H-mode scenarios are expected to present a significant level of stiffness in both the ion and electron channels, so temperature profiles will be determined by thresholds. It will then become a priority of future work to assess theoretical predictions of R/L_{T_e} and R/L_{T_i} thresholds and their parametric dependences, including the stabilizing effect of $E \times B$ shear and the nonlinear up-shift in the ion channel. This work should aim at extracting from experiments the main parameters that affect thresholds and quantifying their effect, with special emphasis on the ion channel, for which JET has unique diagnostics. The results should then be compared with various theoretical models, making more extensive use of nonlinear fluid and gyrokinetic codes with respect to what has been done so far. On the experimental side, ICRH power modulation using ^{3}He has already been shown to be the best tool for exploring ion and electron stiffness and thresholds, together with careful shaping of power deposition profiles and well-designed scans of plasma parameters. The availability of more ICRH power following installation on JET of the ITER-like ICRH antenna will provide also the possibility of studying plasmas with reduced rotation and $T_e \sim T_i$, i.e., in conditions more similar to those of ITER. The impact of turbulence spreading on plasma profiles will have to be assessed.

The basic understanding of a turbulence-generated particle pinch that increases with decreasing collisionality suggests that ITER density profiles will have a significant peaking, as supported by the JET database. In this area the main unsolved issues are the dependence of

the pinch on magnetic shear in H-mode plasmas and the quantitative match between the measured peaking and the predictions by gyrokinetic codes when collisions are included. The availability of more ICRH power from the ITER-like ICRH antenna will provide the possibility of studying particle transport with reduced importance of core particle sources provided by NBI heating, reduced rotation, and $T_e \sim T_i$ conditions.

JET results suggest that impurity accumulation may not represent a problem for the ITER H-mode low-collisionality scenarios, which will be dominated by turbulent transport. In these conditions, light impurities present an outward convection that prevents accumulation, and the accumulation of heavy impurities may also be prevented by the large amount of central electron heating provided by alpha particles, which can induce an impurity pinch reversal and increased diffusion. In turbulence-dominated impurity transport, the presence of a finite density gradient is also not a cause for concern, since it contributes to expelling impurities rather than driving them toward the core as in neoclassical impurity transport. However, these conclusions are presently still based on the analysis of a limited database and its modeling with linear gyrolinetic codes, and they call for extension to a larger number of experimental conditions and modeling with nonlinear tools. Also, impurity accumulation in ITBs still raises concern due to dominant neoclassical impurity transport in layers in which turbulence is suppressed. The usefulness of electron heating in this case remains to be explored.

The understanding of momentum transport is the least advanced, and still not enough basic insight has been reached to even hint what would be the level of rotation in ITER plasmas. For toroidal rotation, it appears that the effective Prandtl number $\chi_{\varphi\,eff}/\chi_{i\,eff}$ is lower than is conventionally assumed for ITER predictions. From first perturbative momentum transport experiments in JET, indications emerge that this is because of the presence of a significant turbulence-generated inward momentum pinch, whereas the real Prandtl number χ_{φ}/χ_i remains close to 1 in accordance with gyrokinetic predictions. More dedicated experiments making use of transients will be required to characterize the parametric dependences of this convective term and will allow better comparison with theory than do steady-state data alone. In addition, the role of edge momentum transport and generation needs thorough experimental and theoretical assessment. Good amounts of new data coming from ripple experiments and edge ergodization experiments using error field correction coils have recently been collected and will provide precious information to compare with theory. For poloidal rotation, it has become evident that the usual assumption of neoclassical poloidal rotation does not hold in any plasma regime, because of the presence of anomalous poloidal flows generated by Reynolds and Maxwell stresses. The effect of such flows in H-mode plasmas has still to be assessed, but the largest flows are measured in plasmas with ITBs and certainly contribute to sustaining the ITB through increased $E \times B$ flow shear. It is still unclear whether such poloidal flows are also a crucial ingredient for ITB triggering, and more experimental data and comparison with not only fluid but also gyrokinetic codes will be required to gain deeper insight into the role of the anomalous poloidal velocity.

More insight into the physics of ITBs has been reached, with a clear identification of the roles of $E \times B$ flow shear, negative magnetic shear, and alpha stabilization in ITB sustainment. With respect to ITB triggering, of major importance in JET is the role of rational magnetic surfaces, which is still missing a consolidated explanation, but research is focusing on the hypothesis that it may be connected with the onset of anomalous poloidal flows that help trigger the ITB via an increased $E \times B$ flow shear. This will require further work on the theoretical side and comparison with the existing, quite exhaustive experimental database. Such progress in understanding forms the physics basis for developing reliable control tools that may allow the use of ITBs in ITER Advanced Tokamak (AT) scenarios. Weak ITBs seem presently more suitable in this respect, due to the fact that strong ITBs (such as in the presence of strongly reversed q profiles) are prone to impurity accumulation and can easily get out of control, leading to excessive pressure gradients and disruptions.

Integrated core-edge transport modeling tools have become available at JET within a specific project, Integration of Transport and MHD Codes at JET, which has coupled existing core and edge transport codes as well as heating, MHD, and microstability codes to create a versatile tool directly linked to JET and also ITPA databases. This has led to an increased number of modelers working on JET results under the coordination of the JET Transport Task Force, and to a significant progress in the JET modeling activity, providing support for the interpretation of experimental sessions and also for scenario development work.

REFERENCES

1. J. D. CALLEN et al., *Nucl. Fusion*, **27**, 1857 (1987).

2. J. P. CHRISTIANSEN et al., *Nucl. Fusion*, **28**, 817 (1988).

3. P. H. REBUT et al., in *Plasma Physics and Controlled Nuclear Fusion Research*, Nice, France, 1988, IAEA-CN-50/D-IV-1, Vol. 2, p. 191, IAEA, Vienna (1989).

4. B. BALET et al., *Nucl. Fusion*, **34**, 1175 (1994).

5. J. P. CHRISTIANSEN et al., *Proc. 26th EPS Conf. Controlled Fusion and Plasma Physics*, Maastricht, The Netherlands, ECA Vol. 23J, 209 (1999)

6. J. G. CORDEY et al., *Nucl. Fusion*, **39**, 301 (1999).

7. B. J. D. TUBBING et al., *Nucl. Fusion*, **27**, 1843 (1987).

8. P. MANTICA et al., *Nucl. Fusion*, **32**, 2203 (1992).

9. P. GALLI et al., *Nucl. Fusion*, **38**, 1355 (1998).

10. V. PARAIL et al., *Nucl. Fusion*, **37**, 481 (1997).

11. J. G. CORDEY et al., *Plasma Phys. Control. Fusion*, **36**, A267 (1994).

12. J. G. CORDEY et al., *Nucl. Fusion*, **35**, 101 (1995).

13. M. ERBA et al., *Plasma Phys. Control. Fusion*, **39**, 261 (1997).

14. R. E. WALTZ et al., *Phys. Plasmas*, **14**, 056116 (2007).

15. X. GARBET et al., *Plasma Phys. Control. Fusion*, **46**, B557 (2004).

16. A. G. PEETERS et al., *C. R. Physique*, **7**, 592 (2006).

17. F. IMBEAUX et al., *Plasma Phys. Control. Fusion*, **43**, 1503 (2001).

18. X. GARBET et al., *Plasma Phys. Control. Fusion*, **46**, 1351 (2004).

19. A. M. DIMITS et al., *Phys. Plasmas*, **7**, 969 (2000).

20. F. JENKO et al., *Plasma Phys.Control. Fusion*, **47**, B195 (2005).

21. D. C. McDONALD et al., *Fusion Sci. Technol.*, **53**, 891 (2008).

22. T. DANNERT and F. JENKO, *Phys. Plasmas*, **12**, 072309 (2005).

23. P. MANTICA and F. RYTER, *C. R. Physique*, **7**, 634 (2006).

24. M. MANTSINEN et al., *Nucl. Fusion*, **44**, 33 (2004).

25. D. VAN EESTER et al., in *Recent ³He Radio Frequency Heating Experiments on JET*, C. B. FOREST, Ed., AIP Conf. Proc. 694, AIP, New York (2003).

26. G. V. PEREVERZEV et al., "ASTRA: An Automatic System for Transport Analysis in a Tokamak," Max-Planck-IPP Report IPP 5/98 (2002).

27. P. MANTICA et al., *Proc. 19th IAEA Fusion Energy Conf.*, Lyon, France, IAEA-CN-94/EX/P1/04 (2002).

28. P. MANTICA et al., *Proc. 30th European Conf. Controlled Fusion and Plasma Physics*, St. Petersburg, Russia, 2003, O-3.1A, European Physical Society ECA Vol. 27A (2003).

29. P. MANTICA et al., *Proc. 31st EPS Conf. Plasma Physics*, London, England, 2004, ECA 28G, P-1.153, European Physical Society (2004).

30. P. MANTICA et al., *Proc. 20th IAEA Fusion Energy Conf.*, Vilamoura, Portugal, 2004, EX/P6-18, IAEA (2004).

31. C. BOURDELLE et al., *Nucl. Fusion*, **42**, 892 (2002).

32. G. REGNOLI and M. ROMANELLI, Personal Communication.

33. G. TARDINI et al., *Nucl. Fusion*, **42**, 258 (2002).

34. F. RYTER et al., *Nucl. Fusion*, **43**, 1396 (2003).

35. F. RYTER et al., *Phys. Rev. Lett.*, **95**, 085001 (2005).

36. F. RYTER et al., *Plasma Phys. Control. Fusion*, **48**, B453 (2006).

37. A. G. PEETERS et al., *Phys. Plasmas*, **12**, 022505 (2005).

38. M. KOTSCHENREUTHER, G. REWOLDT, and W. M. TANG, *Comput. Phys. Commun.*, **88**, 128 (1995).

39. R. E. WALTZ et al., *Phys. Plasmas*, **4**, 2482 (1997).

40. M. KOTSCHENREUTHER et al., *Phys. Plasmas*, **2**, 2381 (1995).

41. H. NORDMAN, J. WEILAND, and A. JARMEN, *Nucl. Fusion*, **30**, 983 (1990).

42. G. CORDEY et al., *Nucl. Fusion*, **43**, 670 (2003).

43. G. CENACCHI and A. TARONI, "JETTO: A Free Boundary Plasma Transport Code (Basic Version)," Rapporto ENEA RT/TIB 1988 (5).

44. L. GARZOTTI et al., *Nucl. Fusion*, **43**, 1829 (2003).

45. P. MANTICA et al., *Plasma Phys. Control. Fusion*, **44**, 2185 (2002).

46. I. VOITSEKHOVITCH et al., *Proc. 33rd EPS Conf. Plasma Physics*, Rome, Italy P1.078 (2006).

47. R. BUDNY et al., *Proc. 21st Fusion Energy Conf.*, Chengdu, China, IT/P1-5, IAEA (2006).

48. Z. LIN and T. S. HAHM, *Phys. Plasmas*, **11**, 1099 (2004).

49. V. NAULIN, A. H. NIELSEN, and J. J. RASMUSSEN, *Phys. Plasmas*, **12**, 122306 (2005).

50. V. NAULIN et al., *Proc. 33rd EPS Conf. Plasma Physics*, Rome, Italy, P1.076 (2006).

51. B. PH. VAN MILLIGEN et al., *Plasma Phys. Control. Fusion*, **47**, B743 (2005).

52. D. DEL-CASTILLO-NEGRETE, *Phys. Plasmas*, **13**, 082308 (2006).

53. R. C. WOLF et al., *Plasma Phys. Control. Fusion*, **45**, 1757 (2003).

54. A. R. POLEVOI et al., *J. Plasma Fusion Res. Series*, **5**, 82 (2002).

55. V. MUKHOVATOV et al., *Nucl. Fusion*, **43**, 942 (2003).

56. A. A. WARE, *Phys Rev. Lett.*, **25**, 916 (1970).

57. C. ANGIONI et al., *Phys. Rev. Lett.*, **90**, 205003 (2003).

58. M. VALOVIC et al., *Plasma Phys. Control. Fusion*, **44**, 1911 (2002).

59. J. ONGENA et al., *Nucl. Fusion*, **44**, 124 (2004).

60. H. WEISEN et al., *Nucl. Fusion*, **45**, L1 (2005).

61. M. F. F. NAVE et al., *Nucl. Fusion*, **43**, 1204 (2003).

62. H. WEISEN et al., *Plasma Phys. Control. Fusion*, **48**, A457 (2006).

63. C. D. CHALLIS et al., *Nucl. Fusion*, **29**, 563 (1989).

64. R. J. GOLDSTON et al., *J. Comput. Phys.*, **43**, 61 (1981).

65. J O'ROURKE et al., *Plasma Phys. Control. Fusion*, **35**, 585 (1993).

66. M. VALOVIC et al., *Plasma Phys. Control. Fusion*, **46**, 1877 (2004).

67. A. ZABOLOTSKY et al., *Nucl. Fusion*, **46**, 594 (2006).

68. L. GARZOTTI et al., *Nucl. Fusion*, **46**, 73 (2006).

69. A. ZABOLOTSKY et al., *Plasma Phys. Contr. Fusion*, **45**, 735 (2003).

70. L. GARZOTTI et al., *Nucl. Fusion*, **46**, 994 (2006).

71. L. GARZOTTI et al., *Nucl. Fusion*, **43**, 1829 (2003).

72. H. WEISEN et al., *Plasma Phys. Control. Fusion*, **46**, 751 (2004).

73. V. V. YANKOV, *Plasma Phys. Rep.*, **21**, 719 (1995).

74. M. B. ISICHENKO, A. V. GRUZINOV, P. H. DIAMOND, and P. N. YUSHMANOV, *Phys. Plasmas*, **3**, 1916 (1996).

75. C. ANGIONI et al., *Phys. Plasmas*, **12**, 112310 (2005).

76. G. T. HOANG et al., *Phys. Rev. Lett,*, **90**, 155002 (2003).

77. H. WEISEN et al., *21st IAEA Conf. Plasma Fusion and Controlled Fusion*, Chengdu, China, IAEA-CN-149/EX/8.4 (2006); available on the Internet at http://www-pub.iaea.org/MTCD/Meetings/FEC2006Presentations/Presentations/20-oct-06/talk_EX8-4.ppt.

78. C. ANGIONI et al., *Nucl. Fusion*, **47**, 1326 (2007).

79. K.-D. ZASTROW et al., *Plasma Phys. Control. Fusion*, **46**, B255 (2004).

80. S. E. SHARAPOV et al., "Burning Plasma Studies at JET," *Fusion Sci. Technol.*, **53**, 989 (2008).

81. K. BORRASS et al., *Nucl. Fusion*, **44**, 752 (2004).

82. T. TALA et al., *Nucl. Fusion*, **45**, 1027 (2005).

83. D. PASINI et al., *Nucl. Fusion*, **30**, 2049 (1990).

84. L. LAURO TARONI et al., *Contrib. Plasma Phys.*, **38**, 242 (1998).

85. S. P. HIRSHMAN and D. J. SIGMAR, *Nucl. Fusion*, **21**, 1079 (1981).

86. H. SUMMERS, ADAS Manual V2.6; available on the Internet at http://adas.phys.strath.ac.uk/.

87. R. GIANNELLA et al., *Plasma Phys. Control. Fusion*, **34**, 687 (1992).

88. D. PASINI et al., *Plasma Phys. Control. Fusion*, **34**, 677 (1992).

89. R. GIANNELLA et al., *Nucl. Fusion*, **34**, 1185 (1994).

90. M. MATTIOLI et al., *Nucl. Fusion*, **35**, 1115 (1995).

91. K. D. LAWSON et al., *Proc. 35th EPS Conf. Controlled Fusion and Plasma Physics*, Praha, Czech Republic, ECA Vol. 22C, 377 (1998).

92. L. C. INGESSON et al., *Nucl. Fusion*, **38**, 1675 (1998).

93. M. ROMANELLI and M. OTTAVIANI, *Plasma Phys. Control. Fusion*, **40**, 1767 (1998).

94. H. CHEN et al., *Phys. Plasmas*. **7**, 4567 (2000).

95. H. CHEN et al., *Nucl. Fusion*, **41**, 31 (2001).

96. A. C. C. SIPS et al., *Proc. 26th EPS Conf. Controlled Fusion and Plasma Physics*, Maastricht, The Netherlands, ECA Vol.23J, 217 (1999).

97. R. DUX et al., *Nucl. Fusion*, **44**, 260 (2004).

98. C. GIROUD et al., *Proc. 28th Conf. Plasma Physics and Controlled Fusion*, Funchal, Portugal, ECA Vol 25A, p. 549 (2001).

99. P. BELO et al., *Plasma Phys. Control. Fusion*, **46**, 1299 (2004).

100. C. GIROUD et al., *Nucl. Fusion*, **47**, 313 (2007).

101. C. GIROUD et al., *Proc. 21st IAEA Conf. Plasma Fusion and Controlled Fusion*, Chengdu, China, October 16–21, 2006, IAEA-CN-149/EX/8.3 (2006); available on the Internet at http://www.naweb.iaea.org/napc/physics/FEC/FEC2006/html/node407.htm#81216.

102. C. ANGIONI et al., *Phys. Plasmas*, **14**, 055905 (2007).

103. J. ONGENA et al., *Nucl. Fusion*, **44**, 124 (2004).

104. P. MONIER-GARBET et al., *Nucl. Fusion*, **45**, 1404 (2005).

105. H. CHEN et al., *Plasma Phys. Control. Fusion*, **43**, 369 (2001).

106. M. E. PUIATTI et al., *Plasma Phys. Control. Fusion*, **44**, 1863 (2002).

107. M. E. PUIATTI et al., *Plasma Phys. Control. Fusion*, **45**, 2011 (2003).

108. B. UNTERBERG et al., *Plasma Phys. Control. Fusion*, **46**, A241 (2004).

109. M. E. PUIATTI et al., *Phys. Plasmas*, **13**, 042501 (2006).

110. C. ANGIONI and A. G. PEETERS, *Phys. Rev. Lett.*, **96**, 095003 (2006).

111. K. H. BURRELL et al., *Phys. Plasmas*, **4**, 1499 (1997).

112. A. M. GAROFALO et al., *Nucl. Fusion*, **41**, 1171 (2001).

113. Y. LIU et al., *Nucl. Fusion*, **45**, 1131 (2005).

114. A. KALLENBACH et al., *Plasma Phys. Contol. Fusion*, **33**, 595 (1991).

115. J. S. DE GRASSIE et al., *Nucl. Fusion*, **43**, 142 (2003).

116. K.-D. ZASTROW et al., *Nucl. Fusion*, **38**, 257 (1998).

117. P. C. DE VRIES et al., *Plasma Phys. Control. Fusion*, **48**, 1693 (2006).

118. P. C. DE VRIES et al., "Scaling of Rotation and Momentum Confinement in JET Plasmas," *Plasma Phys. Control. Fusion* (submitted for publication).

119. N. MATTOR and P. DIAMOND, *Phys. Fluids*, **31**, 1180 (1988).

120. T. TALA et al., "Toroidal and Poloidal Momentum Transport Studies in Tokamaks," *Plasma Phys. Control. Fusion*, **49**, B291–B302 (2007).

121. B. COPPI, *Nucl. Fusion*, **21**, 1363 (1981).

122. R. R. DOMINGUEZ and G. M. STAEBLER, *Phys. Fluids B*, **5**, 387 (1993).

123. G. M. STAEBLER et al., *BAP*, **46**, 221 (2001), LP1-17.

124. A. G. PEETERS et al., *Phys. Rev. Lett.* **98**, 265003 (2007).

125. T. S. HAHM et al., *Phys. Plasmas*, **14**, 072302 (2007).

126. O. D. GURCAN et al., *Phys. Plasmas*, **14**, 042306 (2007).

127. A. G. PEETERS and D. STRINTZI, *Phys. Plasmas*, **11**, 3748 (2004).

128. J. E. RICE et al., *Phys. Plasmas*, **11**, 2427 (2004).

129. J. S. DE GRASSIE et al., *Phys. Plasmas*, **11**, 4323 (2004).

130. A. BORTOLON et al., *Phys. Rev. Lett.*, **97**, 235003 (2006).

131. J. S. DE GRASSIE et al., *Phys. Plasmas*, **14**, 056115 (2007).

132. L.-G. ERIKSSON et al., "Toroidal Rotation in RF Heated JET Plasmas," *Proc. 17th Topl. Conf. Radio Frequency Power in Plasmas*, Clearwater, Florida (2007).

133. J. WEILAND and H. NORDMAN, *Proc. 33rd European Physical Society Conf. Controlled Fusion and Plasma Physics*, Rome, Italy, ECA, Vol. 30, P2.186 (2006).

134. A. ERIKSSON et al., *Plasma Phys. Control. Fusion*, **49**, 1931 (2007).

135. J. E. KINSEY, G. M. STAEBLER, and R. E. WALTZ, *Phys. Plasmas*, **12**, 052503 (2005).

136. T. TALA et al., *Nucl. Fusion*, **47**, 1012 (2007).

137. R. E. BELL et al., *Phys. Rev. Lett.*, **81**, 1429 (1998).

138. W. M. SOLOMON et al., *Phys. Plasmas*, **13**, 056116 (2006).

139. W. HOULBERG et al., *Phys. Plasmas*, **4**, 3231 (1997).

140. K. CROMBÉ et al., *Phys. Rev. Lett.*, **95**, 155003 (2005).

141. T. TALA et al., *Nucl. Fusion*, **46**, 548 (2006).

142. E. J. JOFFRIN et al., *Nucl. Fusion*, **42**, 235 (2002).

143. E. J. JOFFRIN et al., *Plasma Phys. Control. Fusion*, **44**, 1738 (2002).

144. A. G. PEETERS and C. ANGIONI, *Phys. Plasmas*, **12**, 072515 (2005).

145. JET TEAM and C. GORMEZANO, *Proc. 16th Int. Conf. Plasma Physics and Controlled Nuclear Fusion Research*, Montreal, Canada, 1996, Vol. 1, IAEA, Vienna, p. 487 (1997).

146. C. GORMEZANO et al., "Advanced Tokamak Scenario Development at JET," *Fusion Sci. Technol.*, **53**, 958 (2008).

147. X. LITAUDON et al., *Nucl. Fusion*, **43**, 565 (2003).

148. X. LITAUDON, *Plasma Phys. Control Fusion*, **48**, A1 (2006).

149. J. F. DRAKE et al., *Phys. Rev. Lett.*, **77**, 494 (1996).

150. F. ROMANELLI and F. ZONCA, *Phys. Fluids*, **B5**, 4081 (1993).

151. J. W. CONNOR and R. J. HASTIE, *Phys. Rev. Lett.*, **92**, 075001 (2004).

152. R. E. WALTZ et al., *Phys. Plasmas*, **2**, 2408 (1995).

153. H. BIGLARI et al., *Phys. Fluids B*, **2**, 1 (1990).

154. T. S. HAHM and K. H. BURRELL, *Phys. Plasmas*, **2**, 1648 (1995).

155. G. TRESSET et al., *Nucl. Fusion*, **42**, 520 (2002).

156. C. D. CHALLIS et al., *Plasma Phys. Control. Fusion*, **44**, 1031 (2002).

157. S. E. SHARAPOV et al., *Nucl. Fusion*, **46**, S868 (2006).

158. D. MOREAU et al., *Nucl Fusion*, **43**, 870 (2003).

159. D. MAZON et al., *Plasma Phys. Control. Fusion*, **45**, L47 (2003).

160. R. V. BUDNY et al., *Plasma Phys. Control. Fusion*, **44**, 1215 (2002).

161. F. CRISANTI et al., *Nucl. Fusion*, **41**, 883 (2001).

162. L.-G. ERIKSSON et al., *Phys. Rev. Lett.*, **88**, 145001 (2002).

163. D. E. NEWMAN et al., *Phys. Plasmas*, **5**, 938 (1998).

164. J. WEILAND, *Collective Modes in Inhomogeneous Plasmas*, IOP (2000).

165. A. L. ROGISTER, *Nucl. Fusion*, **41**, 1101 (2001).

166. J. KIM et al., *Phys. Rev. Lett.* **72**, 2199 (1994).

167. X. GARBET et al., *Nucl. Fusion*, **43**, 975 (2003).

168. T. J. J. TALA et al., *Plasma Phys. Control. Fusion*, **43**, 507 (2001).

169. P. MAGET et al., *Plasma Phys. Control. Fusion*, **45**, 1385 (2003).

170. B. ESPOSITO et al., *Plasma Phys. Control. Fusion*, **45**, 933 (2003).

171. M. A. MALKOV and P. H. DIAMOND, Personal Communication.

172. S.-I. ITOH et al., *Phys. Rev. Lett.*, **89**, 215001 (2002).

173. C. BOURDELLE et al., for the ITPA Topical Group on Transport and ITB Physics, and the International ITB Database Working Group, *Nucl. Fusion*, **45**, 110 (2005).

174. Y. F. BARANOV et al., *Plasma Phys. Control. Fusion*, **47**, 975 (2005).

175. A. BECOULET et al., *Plasma Phys. Control. Fusion*, **43**, A395 (2001).

176. P. MANTICA et al., *Phys. Rev. Lett.*, **96**, 95002 (2006).

177. A. CASATI, Laurea Thesis, Politechnic of Milano (2006).

178. G. D.CONWAY et al., *Rev. Sci. Instrum.*, **70**, 3921 (1999).

179. G. D. CONWAY et al., *Phys. Rev. Lett.*, **84**, 1463 (2000).

180. G. D. CONWAY et al., *Plasma Phys. Control. Fusion*, **44**, 1167 (2002).

181. G. M. D. HOGEWEIJ et al., *Plasma Phys. Control. Fusion*, **44**, 1155 (2002).

182. G. M. D. HOGEWEIJ et al., "Analysis of Electron Internal Transport Barriers in JET Low and Reversed Shear Discharges," *Proc. 32th EPS Conf.*, Tarragona, Spain, P4.039 (2005).

183. A. BOTTINO, PhD Thesis, EPFL, Lausanne, Switzerland (2004).

184. F. CRISANTI et al., *Proc. 20th IAEA Fusion Energy Conf.*, Vilamoura, Portugal, EX/P2-1 (2004).

185. G. TARDINI et al., *Nucl. Fusion*, **47**, 280 (2007).

186. T. TALA et al., *Nucl. Fusion*, **46**, 548 (2006).

187. T. TALA et al., *Nucl. Fusion*, **45**, 1027 (2005).

188. V. V. PARAIL et al., *Nucl. Fusion*, **39**, 429 (1999).

189. G. M. D. HOGEWEIJ et al., *Nucl. Fusion*, **38**, 1881 (1998).

190. A. M. R. SCHILHAM et al., *Nucl. Fusion*, **42**, 581 (2002).

191. A. MARINONI et al., *Plasma Phys. Control. Fusion*, **48**, 1469 (2006).

192. A. CASATI et al., *Phys.Plasmas*, **14**, 092303 (2007).

193. V. BASIUK et al., *Nucl. Fusion*, **43**, 822 (2003).

194. J. KINSEY et al., *Phys Plasmas*, **12**, 062302 (2005).

195. J. WEILAND and I. HOLOD, *Phys. Plasmas*, **12**, 012505 (2005).

196. X. GARBET et al., *Phys. Plasmas*, **8**, 2793 (2001).

197. I. VOITSEKHOVITCH et al., *Phys. Plasmas*, **9**, 4671 (2002).

198. A. THYAGARAJA, *Plasma Phys. Control. Fusion*, **42**, B255 (2000).

199. S. SHARAPOV et al., "Development of Alfvén Spectroscopy in Advanced Scenarios on JET," *Proc. 21st IAEA Fusion Energy Conf.*, Chengdu, China, October 16–21, 2006 (2006); also preprinted in IOP site EFDA-JET-CP(06)05-14.

200. J. CANDY et al., *Phys. Plasmas*, **9**, 1938 (2004).

201. A THYAGARAJA et al., *European J. Mech. B/Fluids*, **23**, 475 (2004).

202. R. E. BELL et al., *Phys. Rev. Lett.*, **81**, 1429 (1998).

203. W. M. SOLOMON et al., *Phys. Plasmas*, **13**, 056116 (2006).

204. Y. BARANOV et al., *Plasma Physics Control. Fusion*, **46**, 1181 (2004).

205. P. MAGET et al., *Nucl. Fusion*, **39**, 949 (1999).

206. L. GARZOTTI et al., *Nucl. Fusion*, **46**, 73 (2006).

207. W. DORLAND et al., *Phys. Rev. Lett.*, **85**, 5579 (2000).

208. L. LAURO-TARONI et al., *Proc. 21st EPS Conf. Controlled Fusion and Plasma Physics*, Montpellier, France, Vol. I, p. 102 (1994).

209. R. SIMONINI et al., *Contrib. Plasma Phys.*, **34**, 368 (1994).

210. A. TARONI and JET TEAM, *Proc. 16th IAEA Fusion Energy Conf.*, Montreal, Canada, paper IAEA-CN-64/D3-3, Vol. 2, p. 477 (1996).

211. M. FICHTMÜLLER et al., *J. Nucl. Mater.*, **266–269**, 330 (1999).

212. J. W. CONNOR et al., *Proc. 16th IAEA Fusion Energy Conf.*, Montreal, Canada, paper IAEA-CN-64/FP-21, Vol. 2, p. 935 (1996).

213. V. PARAIL et al., *Plasma Phys. Control. Fusion*, **40**, 805 (1998).

214. A. TARONI et al., *Contrib. Plasma Phys.*, **38**, 37 (1998).

215. G. J. RADFORD et al., *Contrib. Plasma Phys.*, **38**, 183 (1998).

216. A. LOARTE, *J. Nucl. Mater.*, **241–243**, 118 (1997).

217. M. FICHTMULLER et al., *Czech. J. Phys.*, **48**, Suppl. 2, 25 (1998).

218. J. S. LONNROTH et al., *Proc. 32nd EPS Conf. Plasma Physics and Controlled Fusion*, Tarragona, Spain, Vol. 29C, P4.043 (2005).

219. A. TARONI et al., *Plasma Phys. Control. Fusion*, **36**, 1629 (1994).

220. J. G. CORDEY et al., *Plasma Phys. Control. Fusion*, **36**, A267 (1994).

221. A. CHERUBINI et al., *Plasma Phys. Control. Fusion*, **38**, 1421 (1996).

222. P. R. THOMAS et al., *Phys. Rev. Lett.*, **80**, 5548 (1998).

223. V. PARAIL et al., *Nucl. Fusion*, **39**, 369 (1999).

224. F. X. SOLDNER et al., *Nucl. Fusion*, **39**, 407 (1999).

225. K. C. SHAING and E. C. CRUME, Jr., *Phys. Rev. Lett.*, **63**, 2369 (1989).

226. Y. KISHIMOTO et al., *Proc. 16th Int. Conf. Fusion Energy*, Montreal, Canada, 1996, Vol. 2, p. 581, IAEA, Vienna (1997).

227. V. PARAIL et al., *Plasma Phys. Reports*, **29**, 539 (2003).

228. A. B. MIKHAILOVSKII et al., *Plasma Phys. Rep.*, **23**, 844 (1997).

229. J. LÖNNROTH et al., *Plasma Phys. Control. Fusion*, **45**, 1689 (2003).

230. T. ONJUN et al., *Phys. Plasmas*, **11**, 1469 (2004).

231. T. ONJUN et al., *Phys. Plasmas*, **11**, 3006 (2004).

232. S. E. SNYDER et al., *Phys. Plasmas*, **12**, 112508 (2005).

233. T. ONJUN et al., *Phys. Plasmas*, **12**, 082513 (2005).

234. T. ONJUN et al., *Phys. Plasmas*, **12**, 012506 (2005).

235. J. LÖNNROTH et al., *Plasma Phys. Control. Fusion*, **46**, 767 (2004).

236. J. LÖNNROTH et al., *Plasma Phys. Control. Fusion*, **46**, A249 (2004).

237. J. LÖNNROTH et al., *Plasma Phys. Control. Fusion*, **46**, 1197 (2004).

238. J. LÖNNROTH et al., *Plasma Phys. Control. Fusion*, **45**, 1689 (2003).

239. J. W. CONNOR et al., *Phys. Plasmas*, **5**, 2687 (1998).

240. C. MERCIER, *Nucl. Fusion*, **1**, 47 (1960).

241. C. MERCIER, *Nucl. Fusion*, **2** (Suppl.), 801 (1962).

242. J. ONGENA et al., *Plasma Phys. Control. Fusion*, **43**, A11 (2001).

243. G. P. MADDISON et al., *Plasma Phys. Control. Fusion*, **45**, 1657 (2003).

244. K. W. WENZEL and D. J. SIGMAR, *Nucl. Fusion*, **30**, 1117 (1990).

245. J. CONNOR et al., *Nucl. Fusion*, **44**, R1 (2004).

246. A. R. ESTERKIN and A. D. PILIYA, *Nucl. Fusion*, **36**, 1501 (1996).

247. S. NOWAK et al., *Phys. Plasmas*, **3**, 4140 (1996).

248. L.-G. ERIKSSON et al., *Nucl. Fusion*, **33**, 1037 (1993).

249. T. J. J. TALA et al., *Plasma Phys. Control. Fusion*, **44**, 1181 (2002).

250. L. LABORDE et al., *Plasma Phys. Control. Fusion*, **47**, 155 (2005).